Measurement of the Forward-Backward Charge Asymmetry in Electron-Positron Annihilation into a Quark-Antiquark Pair: A Test of Electroweak Interference

By

David Donald Stuart

December 1992

DISSERTATION

Submitted in partial satisfaction of the requirements for the degree of

DOCTOR OF PHILOSOPHY

in

Physics

in the

GRADUATE DIVISION

of the

UNIVERSITY OF CALIFORNIA

DAVIS

Approved:

.....

.....

.....

Abstract

The forward-backward asymmetry of quarks produced in e^+e^- annihilations, summed over all flavors, is measured at $\sqrt{s}$ between 50 and $64GeV$. The asymmetry is found to agree with the electroweak standard model.

Acknowledgements

This thesis reports a measurement made with the AMY detector on the TRISTAN electron-positron collider. The measurement would not have been possible without the combined efforts of the members of the AMY collaboration, and AMY would not have been possible were it not for the successful operation of TRISTAN. Neither AMY nor TRISTAN would have been possible without the support of the various governments and funding agencies which provided financial support. All of these essential contributions are gratefully acknowledged.

I want to thank my AMY colleagues at UC Davis for their guidance and support; A. Balics, R.E. Breedon, Winston Ko, R.L. Lander, K. Maeshima, R.L. Malchow, J. Rowe, and J.R. Smith.

On a personal note, I am grateful to my father for the time he spent with me making model rockets and that short-wave radio which got me excited about science. Also, I want to thank my mother for teaching me to do my best. Finally, thank you Lily for your patience and support while I chased my dream.

Table of Contents

Abstract (pg. ii)

Acknowledgements (pg. iii)

Table of Contents (pg. iv)

Overview (pg. vii)

A brief overview of the thesis is given.

1. Introduction and motivation pg. 1

This chapter gives a brief summary of the standard model and the motivation for studying electroweak interference in quark production at TRISTAN.

2. Quark production pg. 4

This chapter describes the theoretical framework for quark production in e^+e^- annihilation.

2.1 Electroweak formalism

The cross-section for $e^+e^- \rightarrow q\bar{q}$ is given and discussed. The forward-backward asymmetry is defined and discussed. The expectations for the asymmetry and the total cross-section are plotted as functions of the center of mass energy and qualitative features are discussed.

2.2 Initial state radiation

Initial state and final state photon radiation is introduced, and its effects are briefly discussed.

2.3 Gluon radiation

Hard gluon radiation in the final state is introduced, and its effects are briefly discussed.

2.4 Hadronization

The transformation of quarks into final state hadrons is described. It is broken down into 3 phases: gluon radiation, fragmentation, and decay. The 3 phases are described separately, and the phenomenological models used to describe them are discussed. The Monte Carlo program is introduced as a means of implementing the models for each phase, and its necessity and use are explained.

3. Experimental methods pg. 16

This chapter describes the experimental methods used to measure the asymmetry. It begins by describing how the asymmetry would be measured in the ideal case that there were no hadronization effects, and then describes techniques for dealing with effects from each phase of hadronization. Along the way, the techniques of thrust, jet clustering, and jet charge are introduced and developed as needed.

3.1 Prehadronization

This section describes how the asymmetry would be measured in the ideal case that there were no hadronization effects. Sample quark angular distributions from Monte Carlo are shown and the fitting technique is introduced to extract the asymmetry.

3.2 Parton Shower

This section describes the effects of the parton shower (hard and soft gluon radiation). Thrust and jet clustering are introduced as methods for reconstructing the original quark directions.

3.3 Fragmentation

This section describes the effects of fragmentation. The performance of the thrust and jet clustering methods is discussed. Jet charge is introduced, and its performance is discussed.

3.4 Decay

This section describes the effects of decay. The effects of heavy flavor decay is described with regard to the thrust, jet clustering, and jet charge methods.

4. The AMY detector pg. 42

This chapter describes the AMY detector in detail.

5. Detector Effects pg. 57

This chapter describes the effects which come from the imperfections of the detector. It shows how the experimental techniques account for these effects. The detector simulator is introduced and explained in this chapter.

6. Results pg. 71

This chapter gives the results of the measurement.

7. Systematic uncertainties pg. 76

This chapter discusses the systematic uncertainties involved in the asymmetry measurement. In addition, some consistency checks are described such as looking for any effects from gluon radiation.

8. Conclusions pg. 93

This chapter discusses the conclusions which can be drawn from the asymmetry measurement. A value is extracted for the weak axial-vector coupling.

9. Summary pg. 98

A brief summary is given.

Appendix pg. 99

References pg. 101

Overview

This section is a brief overview of the thesis. It is intended to allow a particle physicist to glean the general idea by reading only this section. Everything mentioned in this overview will be repeated in more detail in the body of the thesis.

The annihilation of an electron and positron pair can be mediated by either a photon or a Z_0. At low energies, $e^+e^- \to \gamma$ is more likely, and at center of mass energies near the Z_0 mass, $e^+e^- \to Z_0$ is more likely. But at intermediate energies, the two processes occur with comparable probabilities, so they interfere. Studying this interference provides a sensitive test of the electroweak theory.

Including both γ and Z_0 exchange, the differential cross section for electron-positron annihilation into any fermion-antifermion pair ($e^+e^- \to \{\gamma, Z_0\} \to f\bar{f}$) is[1]

$$\frac{d\sigma_f}{d\Omega} = \frac{\alpha^2}{4s}[R_f(1+\cos^2\theta_f) + B_f\cos\theta_f]$$

The angle θ_f is the angle between the incoming electron and the outgoing fermion. The factors R_f and B_f contain the couplings of the fermions to the photon and the Z_0, and therefore contain the physics of interest. A measurement of R_f and B_f provides information about these couplings which may then be compared to the standard model predictions. The R_f term is symmetric in $\cos\theta$, while the B_f term is antisymmetric in $\cos\theta$. So, the angular asymmetry of the differential cross section provides a measurement of B_f, while the total cross section (integrated over Ω) provides a measurement of R_f.

In principle, this allows examination of the couplings of any fermion (lepton or quark) by identifying events of the desired type and then measuring the

corresponding differential and total cross sections. The e, μ, and τ are easy to identify and have been examined in this way.[2] Other fermions, however, can be difficult or impossible to identify. For example, $e^+e^- \to \nu\bar{\nu}$ events are practically undetectable. In the quark sector, it is difficult to determine the couplings for each flavor independently since it is only possible to tag the heavier quark flavors, and then only with reduced efficiency.[3] However, it is expected that the three generations of quarks have the same couplings (universality), so the flavors can be summed to obtain a combined B and R. (It is also possible to enhance the relative contribution of some flavors in the sum to provide a check on the assumption of universality.) The measurement of R for all quark flavors combined is the subject of another thesis.[4] The measurement of B for all quark flavors combined is the subject of this thesis.

Measuring B amounts to measuring the forward-backward asymmetry, A, of the angular distribution of $\cos\theta$. It is given by

$$A = \frac{3B}{8R}.$$

The procedure is to select $e^+e^- \to q\bar{q}$ events, and measure the angular distribution of the quark i.e., $\cos\theta_q$. However, it is not experimentally possible to tell the difference between the quark jet and the antiquark jet (i.e., between $\cos\theta_q$ and $\cos\theta_{\bar{q}}$). So, instead, the angle θ_+ is used. It is defined with respect to electric charge by using the angle between the incoming positive charge (positron) and the outgoing positive charge (the u or c quark or the d, s, or b *anti*quark). Since $\cos\theta_{\bar{q}} = -\cos\theta_q$, this amounts to a measurement of $A_d - A_u + A_s - A_c + A_b$. This is called the *charge asymmetry* since it is defined with respect to charge.

The experimental determination of θ_+ is accomplished by first finding the thrust axis of the event. This axis is ambiguous with respect to inversion through the origin, and so it could line up with either the quark or the antiquark direction, since they are back-to-back. To determine which jet (i.e., which of the two possible orientations of the thrust axis) is the positive jet, the charge of each jet is

calculated. The charge of a jet is determined by summing the charges of the jet's particles scaled by a weighting factor proportional to the particle's momentum. This weighting is done to reduce the effect of soft particles from the quarks' fragmentation. The thrust axis is then oriented toward the jet with the most positive charge. The azimuthal angle of the oriented thrust axis is then θ_+.

The measurement was done with the AMY detector at the TRISTAN e^+e^- collider with center of mass energies ranging from 50 to 64 GeV. At these energies, the standard model prediction for the forward-backward asymmetry of each individual quark flavor is about -50%, and the total charge asymmetry i.e., $A_d - A_u + A_s - A_c + A_b$, is expected to be about +9.5% when the relative production rates of each quark flavor are taken into account.

The charge asymmetry is found to agree with the standard model predictions, and to strongly disagree with the prediction if electroweak interference is neglected.

1. Introduction and motivation

Particle physics is an attempt to answer the fundamental question: "What is matter made of on its most fundamental level, and what holds it together?" The quest for answers to this question is currently guided by a model[5] developed in the 1960's and 70's. This model (called the Standard Model[6]) can be stated as an answer to that fundamental question. In short, it states that matter is made of elementary particles called quarks and leptons which can be divided into 3 families which differ only in mass. Furthermore, for each of these particles there is an antiparticle which is identical except for having opposite electric charge and parity. The particles interact with each other through four forces; the gravitational, electromagnetic, strong, and weak forces. Due to their very small mass, the gravitational force experienced by elementary particles is negligibly small. The electromagnetic force, of course, couples to the electric charge of the particles. The strong force is felt by quarks but not by leptons, while the weak force is felt by both. The weak force has a vector and an axial-vector part. The axial-vector part couples to the isospin of the particles, I, while the vector part couples to a combination of isospin and electric charge, $I - Q \sin^2 \theta_W$. The coupling to electric charge arises because of a mixing between the electromagnetic and weak forces which is accounted for by the mixing angle, θ_W. Because of this, the electromagnetic and weak forces can be thought of as arising from a single *electroweak* force.

The interactions between the particles are mediated by the exchange of gauge bosons. The electromagnetic force is mediated by photon exchange. The strong force is mediated by gluon exchange. The weak force is mediated by the exchange of $W^{\pm}$ or Z_0 bosons.

Name	Symbol	Approximate mass	Electric charge (e)	Weak vector coupling	Weak axial vector coupling
			Quarks		
down	d	$300MeV$	$-\frac{1}{3}$	-0.35	$-\frac{1}{2}$
up	u	$300MeV$	$+\frac{2}{3}$	$+0.19$	$+\frac{1}{2}$
strange	s	$500MeV$	$-\frac{1}{3}$	-0.35	$-\frac{1}{2}$
charm	c	$1.5GeV$	$+\frac{2}{3}$	$+0.19$	$+\frac{1}{2}$
bottom	b	$4.7GeV$	$-\frac{1}{3}$	-0.35	$-\frac{1}{2}$
top	t	$> 90GeV$	$+\frac{2}{3}$	$+0.19$	$+\frac{1}{2}$
			Leptons		
electron	e	$0.5MeV$	-1	-0.04	$-\frac{1}{2}$
e neutrino	ν_e	0	0	$+\frac{1}{2}$	$+\frac{1}{2}$
muon	μ	$106MeV$	-1	-0.04	$-\frac{1}{2}$
μ neutrino	ν_μ	0	0	$+\frac{1}{2}$	$+\frac{1}{2}$
tau	τ	$1.8GeV$	-1	-0.04	$-\frac{1}{2}$
τ neutrino	ν_τ	0	0	$+\frac{1}{2}$	$+\frac{1}{2}$

Table 1.1: Summary of elementary particles in the Standard Model.

To test and understand this model experimentally, we must find all of the predicted particles and study their interactions. All of the particles have been found except for the tau neutrino (ν_τ), and the top quark (t). In addition, all of the bosons have been found. The W and Z_0 bosons were discovered in 1983 so it is now of interest to carefully study their interactions. The LEP collider at CERN and the SLC at Stanford were built for that purpose. By annihilating electrons and positrons at energies equal to the Z_0 mass, they produce a very large sample of Z_0 exchange interactions which can then be carefully studied.

It is equally interesting to study the interplay between the electromagnetic

Name	Symbol	Approximate mass (GeV)	Electric charge (e)
photon	γ	0	0
gluon	g	0	0
Z_0	Z_0	91	0
W^+	W^+	81	$+1$
W^-	W^-	81	-1

Table 1.2: Summary of gauge bosons in the Standard Model.

and weak forces. This can be done at the TRISTAN collider at KEK which annihilates electrons and positrons at energies below the Z_0 mass, specifically 50 - $64GeV$. In this energy range, the exchange of photons and virtual Z_0's are about equally probable. So, their probability amplitudes strongly interfere. Measuring this interference not only allows a measurement of the couplings, it also provides a test of the electroweak formalism.

This thesis describes such a measurement of the electroweak interference in quark production at TRISTAN.

2. Quark production

2.1 Electroweak formalism

The electroweak theory allows electron-positron annihilation into quarks through two channels: γ exchange and Z_0 exchange. The Feynman diagrams for these processes are shown in figure 2.1.

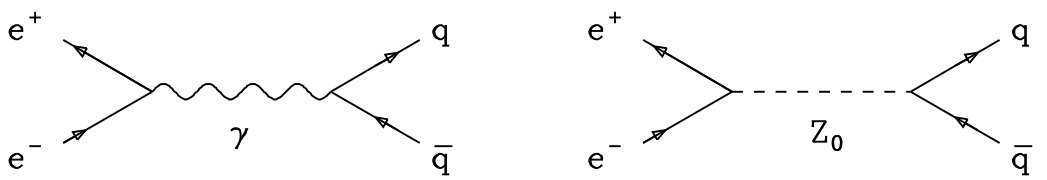

Fig. 2.1: First order Feynman diagrams for quark production in e^+e^- annihilation.

The differential cross section is calculated from the matrix element corresponding to the square of the sum of these two channels. It contains three terms; one from the γ exchange diagram, one from the Z_0 exchange diagram, and a cross term which results from the interference between the γ and Z_0 exchange. The differential cross section is[1]

$$\frac{d\sigma}{d\Omega} = \frac{\alpha^2 C_F}{4s}[R_q(1+\cos^2\theta_q) + B_q\cos\theta_q]. \tag{2.1}$$

θ_q is the production angle of the quark measured from the electron direction and $C_F = 3$ is the color factor accounting for the 3 possible colors of the quarks allowed

by QCD. The coefficients R_q and B_q contain the couplings of the γ and Z_0 to the fermions (q, $\bar{q}$, e^+, and e^-). They are given by

$$R_q = Q_q^2 - 8Q_q g_V^e g_V^q \Re(\chi) + 16({g_V^e}^2 + {g_A^e}^2)({g_V^q}^2 + {g_A^q}^2)|\chi|^2 \tag{2.2}$$

$$B_q = -16Q_q g_A^e g_A^q \Re(\chi) + 128 g_V^e g_V^q g_A^e g_A^q |\chi|^2 \tag{2.3}$$

where Q_q is the electric charge of the quark, g_V^e and g_V^q are the weak vector couplings of the electron and the quark, and g_A^e and g_A^q are the weak axial vector couplings of the electron and the quark. χ contains the Breit-Wigner of the Z_0, and depends upon the mass and width of the Z_0 as well as the center of mass energy, $\sqrt{s}$,

$$\chi = \frac{1}{16\sin^2\theta_W \cos^2\theta_W} \frac{s}{(s - M_Z^2 + iM_Z\Gamma_Z)}. \tag{2.4}$$

Since R_q and B_q depend on the real part of χ (i.e., $\Re(\chi)$) and on its magnitude (i.e., $|\chi|^2$), it is useful to write them out explicitly.

$$\Re(\chi) = \frac{1}{16\sin^2\theta_W \cos^2\theta_W} \frac{s(s - M_Z^2)}{[(s - M_Z^2)^2 + M_Z^2\Gamma_Z^2]}. \tag{2.5}$$

$$|\chi|^2 = \frac{1}{(16\sin^2\theta_W \cos^2\theta_W)^2} \frac{s^2}{[(s - M_Z^2)^2 + M_Z^2\Gamma_Z^2]}. \tag{2.6}$$

There are some general features that are worth noting. The differential cross section contains two terms. The $R_q(1 + \cos^2\theta_q)$ term is symmetric in $\cos\theta_q$, and has the angular form expected from QED for spin $\frac{1}{2}$ particles. The $B_q \cos\theta_q$ term is antisymmetric in $\cos\theta_q$ and does not appear if only the QED (γ exchange) diagram is used.

The R_q factor carries three terms. These correspond to the three terms contributing to the matrix element. The Q_q^2 term comes purely from γ exchange (QED). The $|\chi|^2$ term comes purely from Z_0 exchange (weak). The $\Re(\chi)$ term

comes from interference between γ and Z_0 exchange (electroweak) i.e., from the cross term in the matrix element. Notice that the purely weak part of R_q (the $|\chi|^2$ term) has a maximum when $\sqrt{s} = M_Z$ as expected. Likewise, the interference term drops out in both the pure QED limit ($\sqrt{s} = 0$) and in the pure weak limit ($\sqrt{s} = M_Z$).

The B_q factor is similar, but it does not have a pure QED term.

The oddness of the $\cos\theta_q$ term causes the total cross section (integrated over solid angle) to depend only on R_q. It is

$$\sigma = \frac{4\pi\alpha^2 C_F}{3s} R_q. \tag{2.7}$$

That oddness also causes the backward direction ($\cos\theta_q < 0$) to be favored over the forward direction. The corresponding forward and backward cross sections are

$$\sigma_{|\cos\theta_q>0} = \frac{\pi\alpha^2}{12s}(8R_q + 3B_q)$$

$$\sigma_{|\cos\theta_q<0} = \frac{\pi\alpha^2}{12s}(8R_q - 3B_q).$$

This causes more events to send the quark into the backward direction and the antiquark into the forward direction (since $B_q < 0$). This forward-backward asymmetry can be quantified as the fraction of extra events in the forward direction. I.e.,

$$A_q \equiv \frac{\sigma_{|\cos\theta_q>0} - \sigma_{|\cos\theta_q<0}}{\sigma_{|\cos\theta_q>0} + \sigma_{|\cos\theta_q<0}} \tag{2.8}$$

Plugging in the expressions for the forward and backward cross sections,

$$A_q = \frac{3}{8}\frac{B_q}{R_q}. \tag{2.9}$$

It is then possible to rewrite the differential cross section in terms of the forward-

backward asymmetry.

$$\frac{d\sigma}{d\Omega} = \frac{\alpha^2 C_F}{4s} R_q[(1+\cos^2\theta_q) + \frac{8}{3} A_q \cos\theta_q]. \tag{2.10}$$

So, there are 2 measurable quantities, R_q and A_q, which depend upon the electric charge and electroweak couplings of the quark and electron. Measuring R_q and A_q provides information about the couplings. R_q is found by measuring the total cross-section, and A_q is found by measuring the angular distribution of the differential cross-section. The Standard Model predictions for these quantities are shown as functions of the center of mass energy in figure 2.2.[7] The curves in the figure are for u and d quarks. The curves for the other quark families are identical.

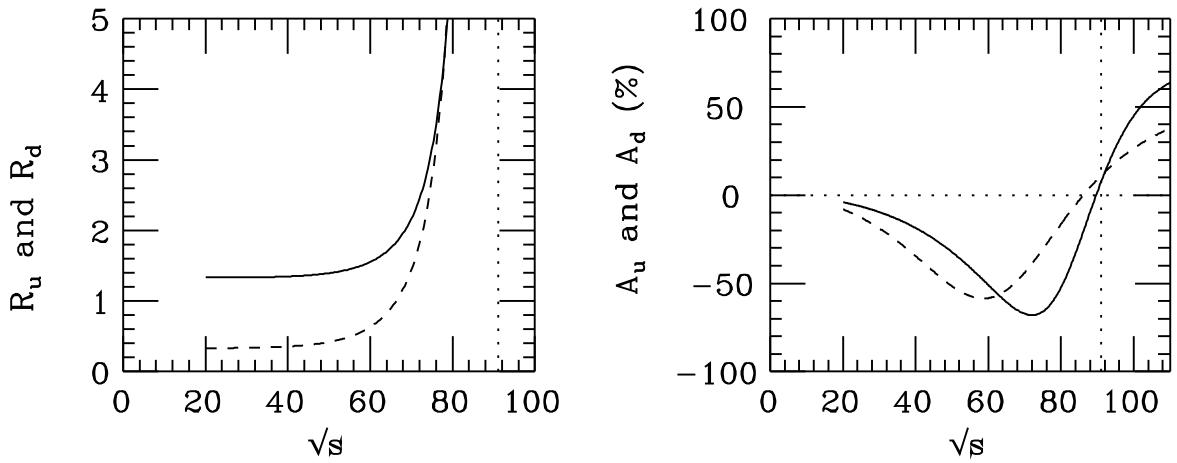

Fig. 2.2: R and A for u and d quarks. The solid curves are for u quarks. The dashed curves are for d quarks. (The heavier quark families are the same.)

From the figure, it is apparent that R_u is greater than R_d. This difference is due to the quarks' electric charges. At low $\sqrt{s}$ the Q_q^2 term dominates, so $R_u/R_d = 4$, but as $\sqrt{s}$ increases, the weak terms begin to dominate and the difference decreases. For energies around $60GeV$, u quarks are produced about $2\frac{1}{2}$ times more often than d quarks.

The figure shows that the *magnitude* of the asymmetry reaches a maximum around 60 to 70 GeV for both types of quarks, and then falls through zero near the Z_0 mass. This happens because the asymmetry is dominated by the interference term in B_q which is largest when the strengths of γ and Z_0 exchange are comparable.

So, there are three general regions of energy. For low energy (say $\sqrt{s} < 40GeV$), QED effects dominate. For intermediate energy (say $40GeV < \sqrt{s} < 80GeV$) electroweak interference effects dominate. For high energy ($\sqrt{s} \rightarrow M_Z$), weak effects dominate. This thesis focuses on the intermediate energy range and the interference effects by measuring the forward-backward asymmetry of all quark flavors combined at energies between 50 and $64GeV$

The asymmetry has several advantages both as a test of the theory and as a probe for new phenomenon. It is sensitive to the *interference* between the electromagnetic and weak forces (i.e., γ and Z_0) and is therefore a good test of electroweak unification. Also, when the 5 quark flavors are combined, their asymmetries nearly cancel. As a result, any new phenomenon affecting quark production will unbalance this cancellation and thus show up distinctly in the asymmetry even if it is not a large effect in the total cross section. The asymmetry is also less dependent upon the sources of systematic errors involved in a measurement of the total cross section such as higher order corrections, luminosity monitoring, and triggering. (However, higher order corrections can have some indirect effect on the asymmetry measurement as is discussed below.)

2.2 Initial and final state radiation

The $e^+e^- \rightarrow q\bar{q}$ cross section is modified by the possibility of initial state or final state photon radiation. This comes from electron bremsstrahlung in the initial state or quark bremsstrahlung in the final state. The Feynman diagrams for these processes are shown in figure 2.3. The cross section for both initial and final state radiation is dependent upon the energy of the radiated photon, E_γ. They

are peaked strongly toward $E_\gamma = 0$, and also toward $E_\gamma = \sqrt{s}/2$, though not as strongly. There is also a dependence on the radiated photon direction which is peaked along the beam direction.

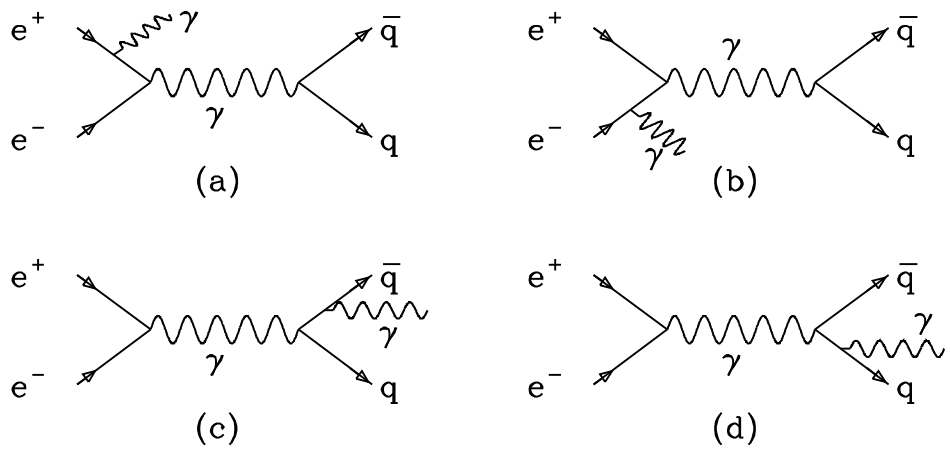

Fig. 2.3: Feynman diagrams for initial and final state radiation. (a) and (b) are initial state radiation. (c) and (d) are final state radiation. Only the γ exchange diagrams are shown. The Z_0 exchange diagrams are similar.

This photon radiation has an effect on the measurement of the forward-backward asymmetry in several ways. The most obvious way is that an initial state photon carries away some of the beam energy, leaving the center of mass energy diminished.[8] As can be seen from figure 2.2b, even a small change in $\sqrt{s}$ can change the asymmetry considerably. Another effect is that for high energy radiation, say $E_\gamma > 0.1\sqrt{s}$, the recoil of the quark and antiquark make their directions deviate noticeably from back-to-back. This makes it difficult to define the quark production direction. Another, and more interesting, effect of initial and final state radiation is that it can produce a forward-backward asymmetry effect of its own. This asymmetry arises because initial state radiation produces a final state with charge conjugation quantum number C = -1 while final state radiation produces a charge conjugation quantum number C = +1. The different C states interfere and produce a forward-backward asymmetry which is *opposite* to the asymmetry from

electroweak interference. This asymmetry is interesting in its own right, and has been examined elsewhere,[9] but for the purposes of this thesis, events with high energy initial or final state radiation are removed to provide a clean measurement of the electroweak asymmetry. The experimental aspects of selecting and removing these events will be discussed later.

2.3 Gluon radiation

The $e^+e^- \rightarrow q\bar{q}$ cross section is also modified by hard gluon radiation in the final state. The Feynman diagrams for this are shown in figure 2.4. Gluon radiation modifies the total cross section by adding radiative corrections. Including gluon radiation to order α_s, the cross section becomes

$$\sigma = \sigma_0(1 + \alpha_s/\pi)$$

where σ_0 is the cross section without gluon radiation (i.e., Eq. 2.7). Since the electroweak asymmetry appears in the angular distribution of the cross section, which is unchanged, gluon radiation has no direct effect on the asymmetry. This makes intuitive sense since the gluon radiation can be thought of as occurring after the $q\bar{q}$ momenta have been determined. However, high energy gluon radiation can have an indirect effect by perturbing the quark directions. If one of the quarks radiates a high energy gluon (say $E_g > 0.1\sqrt{s}$) it will recoil from the gluon and there will be three distinct jets of particles in the final state. It is then important to account for this effect in determining the quark directions since only one of the three jets will have the correct direction information. This is discussed further in the chapter on experimental methods.

2.4 Hadronization

Individual quarks or gluons have never been observed experimentally, so we do not expect to see either the quarks or the gluons in the final state. Instead, they appear as jets of hadrons. The process which forms the quarks and gluons

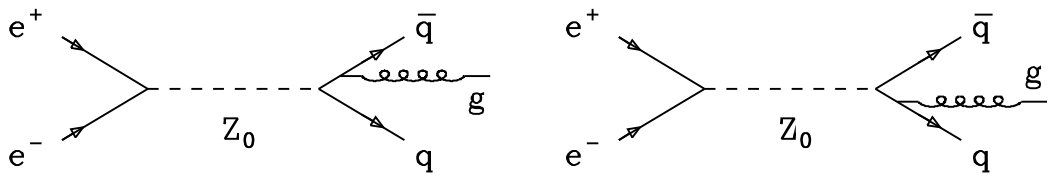

Fig. 2.4: First order (QCD) Feynman diagrams for gluon radiation. Only the Z_0 exchange diagrams are shown. The γ exchange diagrams are similar.

into jets is called hadronization, and can be thought of as occurring in 3 distinct phases.

Hard gluon radiation (see section 2.3) occurs in the first phase. The cross section for this is calculable up to second order of QCD, but calculating higher orders is prohibitively complex. However, there is evidence suggesting that calculations stopping at second order are not sufficient to describe the experimental results,[10] so something must be done to approximate the higher order contributions. The currently best technique for doing this is the *parton shower* algorithm.[11] It is based on the repeated application of the first order QCD branchings; $q \rightarrow qg$, $g \rightarrow q\bar{q}$, and $g \rightarrow gg$. These branchings are governed by the Altarelli-Parisi equations which give the probability for any given branching to occur. This probability is a function of the energy imparted to the daughter particles, and is peaked toward low energy (i.e., in $q \rightarrow qg$, the gluons tend to be soft).

The parton shower algorithm is applied as follows. Initially there is only the q and the $\bar{q}$. The q branches by $q \rightarrow qg$ with the gluon energy chosen randomly according to the probability distribution from the Altarelli-Parisi equations. In the same way, the $\bar{q}$ also branches into $\bar{q}g$, so there are four partons ($q\bar{q}gg$). In the next iteration, all four partons are allowed to branch (with the gluons branching through either $g \rightarrow gg$ or $g \rightarrow q\bar{q}$). In this way, the number of partons increases with each iteration until some minimum energy threshold is reached, and the iteration is stopped. An example is shown in figure 2.5. The large number of branchings in the diagram makes it virtually impossible to calculate analytically. But, the parton shower algorithm can provide an estimate of the contributions from the

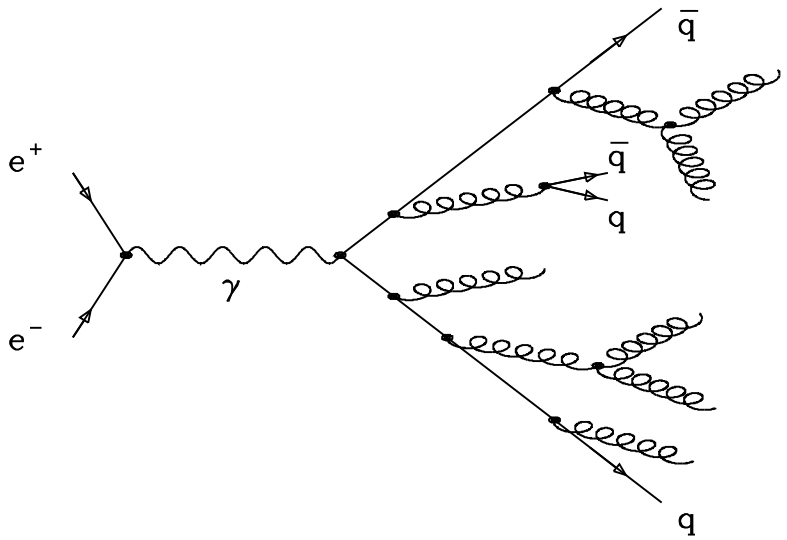

Fig. 2.5: Example of a parton shower in which the partons (quarks and gluons) branch repeatedly through $q \to qg$, $g \to q\bar{q}$, or $g \to gg$.

incalculable higher order processes.

Due to it's iterative nature, the algorithm is well suited to application in a Monte Carlo computer program. This has been done by the LUND group, and it is their program (JETSET version 6.3)[12] which is used in this thesis.

The second phase of hadronization is the *fragmentation* of the quarks and gluons produced by the parton shower. This phase is even softer than the first phase described above. It also cannot be calculated directly and must be approximated by a phenomenologically based model. The LUND Monte Carlo program which is used to model the parton shower also includes a model for the fragmentation phase. This is done using the *string fragmentation* algorithm.[13]

The string fragmentation model pictures the color field concentrated tightly along the line between the quark and the antiquark. This field can be thought of as a string which is under tension. As the q and $\bar{q}$ move apart, the potential energy in the string increases until the string "breaks", creating a $q\bar{q}$ pair at the new endpoints. There are then 2 strings and 2 $q\bar{q}$ pairs. The 2 strings each continue

to stretch and break, creating even more $q\bar{q}$ pairs. This continues iteratively until some cutoff threshold is reached. The remaining strings are then the final state hadrons. Gluons are modelled as a kink on the string connecting the q and $\bar{q}$. The gluon kink moves out from the origin and causes the string to deform from a straight line. As the string stretches, it can break on either side of the gluon kink, and the process proceeds as in the $q\bar{q}$ case. Of course, the parton shower algorithm produces many quarks and gluons, so there must be many strings stretched across all of these partons, but the core algorithm remains the same.

At the end of the string fragmentation process, the $q\bar{q}$ pairs which are connected by strings have nearly equal velocity so that they combine into mesons. For the light quarks, these mesons tend to be soft, each carrying only about 10% of the original quark's momentum. However, this is not the case for the c and b quarks. A heavy quark does not need to give up much of its energy to produce a light quark pair (matching it's velocity) from which it can form a meson. As a result, the heavy mesons which contain the original c or b quark tend to carry a very large fraction of the original quark's momentum. This tendency toward hard fragmentation in heavy quarks is parameterized in the Monte Carlo program with a fragmentation function, $f(z)$, which is a probability distribution giving the probability that a given hadron will end up with a fraction, z, of the original quark's momentum. There are two commonly used parameterizations. The Peterson fragmentation function is[14]

$$f(z) \propto \frac{1}{z(1-\frac{1}{z}-\frac{\alpha_Q}{1-z})},$$

where α_Q depends on the quark mass. The other parameterization is the symmetric Lund fragmentation function. It is

$$f(z) \propto \frac{1}{z}(1-z)^a e^{-\frac{bm_T^2}{z}},$$

where a and b are experimentally determined parameters and m_T is the transverse mass of the quark. Both fragmentation functions are peaked toward $z = 0$ for

the light quarks and toward $z = 1$ for c and b quarks. The Lund fragmentation function is used in this thesis.

The third and final phase is the prompt decay of some of the hadrons which were produced during fragmentation. Some of these are heavy, short lived resonances which decay before they travel far enough to be detected. This decay is also incorporated into the Monte Carlo program. Since the decays are random in nature, the program accounts for them by using empirically determined distributions for both the branching fractions into the different channels and their corresponding lifetimes.

The first two phases described above occur on the extremely short time scale of about 10^{-23} seconds. However, the third phase can occur over the much longer time scale that corresponds to the flight time through the detector i.e., ranging up to several nanoseconds.

Due to the inherent randomness of hadronization, the characteristics of the quarks only survive into the final state in an average sense. For example, the momentum of the quark can be measured by summing the momentum of all the final state particles in the jet of hadrons resulting from the quark. Likewise, the quark's charge can also be measured by summing the charge of all the final state particles in the quark's jet, but there is considerable smearing. Even with perfect detection, such things as the momentum, the charge, and especially the flavor of the original quarks can not be easily determined. The experimental challenge lies in finding a method for extracting such information from the final state particles.

The Monte Carlo program applies empirical models to generate a large statistical sample of artificially generated events with all three of the phases (parton shower, fragmentation, and decays) included. This *generated* data is then processed to account for the geometry and inefficiencies of the detector. This processing is called a detector simulation. The final result is a large sample of events as they would appear in the detector if the quark production model (i.e., the standard model) and the phenomenological models used to describe the 3 phases of

hadronization are correct. This is then compared with the real experimental data sample to determine if the phenomenological models provide a valid description. If they do (and they do[15]), the Monte Carlo data may then be used to develop and test methods for extracting the needed information about the original quarks, and then to determine and correct for any inefficiencies inherent in these methods. Finally, those methods may be used with the real data to measure the asymmetry and compare the results to the standard model.

3. Experimental method

In the previous chapter, the formalism of electroweak quark production was presented. Hadronization was also presented, and the Monte Carlo program was introduced as a way to implement the theories for quark production and hadronization for experimental tests. This chapter deals with the details of the experimental methods used to extract the necessary information from the particles resulting from electroweak quark production and subsequent hadronization.

3.1 Prehadronization

It is illustrative to begin by looking at the quarks before hadronization, and describe an asymmetry measurement for the unrealistically ideal case in which the quarks could be detected directly.

The Monte Carlo program implements the electroweak production cross-section (Eq. 2.10) to produce a sample of events containing the flavor and momentum of the $q\bar{q}$ pair. From the angular distribution of the quark's momentum, the asymmetry can be measured. This is done with several different center of mass energies, and the results are plotted on the theoretical curve for A.

The angular distributions of u and d quarks are shown in figure 3.1. The other flavors are not shown, but c quarks are identical to u quarks, and s and b quarks are identical to d quarks, as expected. The asymmetry can be calculated from the angular distribution in two ways. The most direct method is to use the definition in Eq. 2.8 and just count the number of events in the forward and the backward directions. But, a better way is to fit a function with the form of Eq. 2.10 to the angular distribution and extract the asymmetry from the fit. This results in

smaller errors than the first method because it uses the shape of the whole curve. The asymmetry determined from each method is written on the plots of figure 3.1. The direct method is denoted A_1, and the fitting method is denoted A_2.

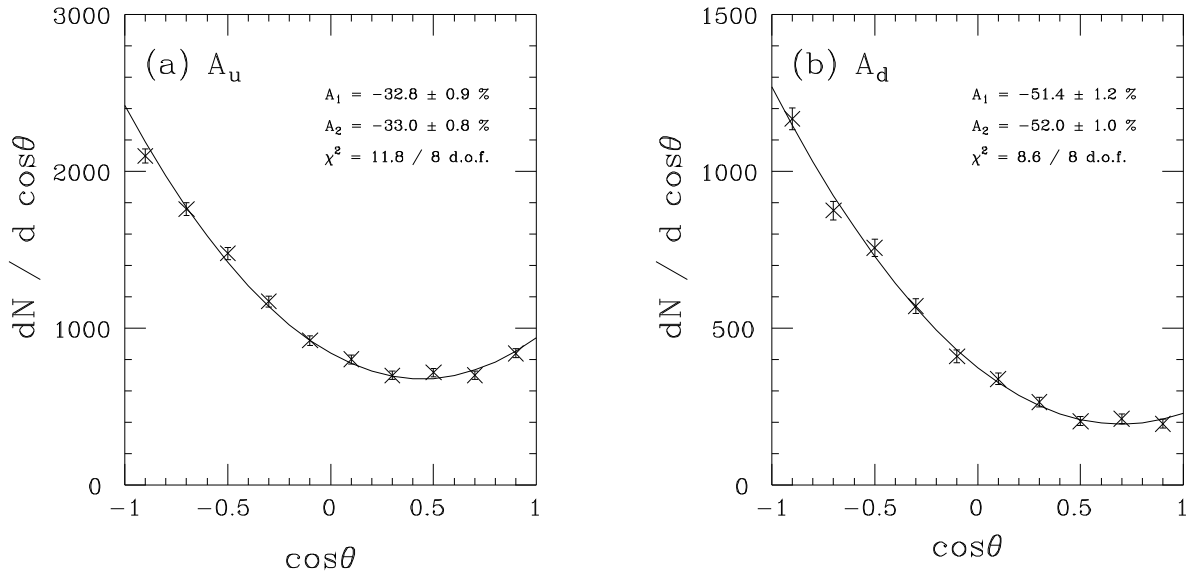

Fig. 3.1: Angular distribution of $\cos\theta$ of the quark in Monte Carlo data at $\sqrt{s} = 52GeV$. The curve is the best fit to Eq. 3.1. (a) u quarks. (b) d quarks.

The fitting method uses a fit to a function of the form

$$\frac{dN}{dx} = R[(1+x^2) + \frac{8}{3}Ax] \tag{3.1}$$

where $x \equiv \cos\theta_q$, and R and A are the parameters varied in the fit. Only A is of interest to us. R contains information related to the luminosity, trigger efficiency, and detection efficiency, but for the purposes of this thesis, it amounts to just a normalization factor, and its fitted value is not used. The fitting can be performed using either a minimum χ^2 or a maximum likelihood approach. The two techniques give similar results, but the χ^2 approach has an advantage since it provides a measure of the goodness of the fit. For that reason, the minimum χ^2 technique is

used, and a maximum likelihood fit is performed only as a consistency check. The curve resulting from the fit is drawn on the plots in figure 3.1, and the χ^2 values are written with the fitted asymmetry values.

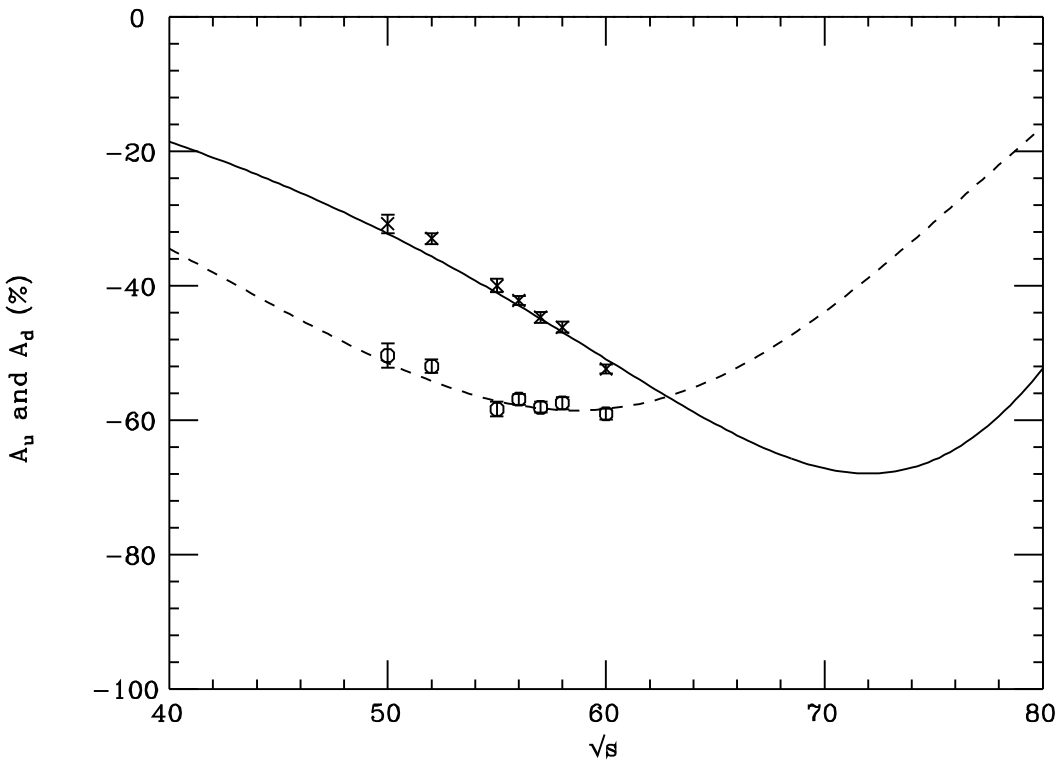

3.2: Asymmetry of u and d quarks measured with Monte Carlo data before hadronization. The solid curve is the Standard Model prediction for u quarks. The dashed curve is the Standard Model prediction for d quarks.

The fitted asymmetry values for several center of mass energies are compared to the Standard Model predictions in figure 3.2. As can be seen from the figure, the Monte Carlo program reproduces the predictions of the electroweak theory. This is of course expected since that is what the Monte Carlo program is for, but it is important to verify this, and it is illustrative to initially see how the asymmetry is determined from the angular distribution without having to be concerned about all the hadronization details.

3.2 Parton shower

As described in the previous chapter, the first phase of hadronization is the radiation of gluons. This is modelled by the parton shower algorithm which is implemented in the Monte Carlo program.

The parton shower algorithm typically results in about 10 soft gluons and slightly modifies the quark directions. Occasionally, however, there is a hard gluon as described in section 2.3. The momentum vectors for the quarks and gluons in two sample events are shown in figure 3.3. Notice that the gluons in figure 3.3(a) are mostly soft so the quark directions are nearly unchanged, but in figure 3.3(b) there is a hard gluon which changes the quark direction substantially. Because of this, it is necessary to find a method for reconstructing the original quark and antiquark directions. There are two common methods which will be used in this thesis; thrust[16] and jet clustering[17].

The thrust method relies on the fact that the quark and antiquark are produced back-to-back and therefore can be described by a single vector which is called the *thrust axis*. It is defined as the axis, $\hat{\mathbf{n}}_T$, which maximizes the thrust value, T, given by

$$T = \frac{\sum_{i=1}^{N} |\vec{\mathbf{p}}_i \cdot \hat{\mathbf{n}}_T|}{\sum_{i=1}^{N} |\vec{\mathbf{p}}_i|} \tag{3.2}$$

where the sum is over all the particles' momentum, $\vec{\mathbf{p}}_i$. The magnitude on the dot product accounts for the q and $\bar{q}$ being back-to-back. With this definition, the thrust axis is the direction which has the largest component of the total momentum, and the thrust value, T, is a measure of the fraction of the total momentum which is along the thrust axis. T ranges from $\frac{1}{2}$ to 1. High thrust indicates that the event has narrow back-to-back jets while low thrust indicates that the event has wide jets or substantial gluon radiation. As an example, the thrust axes are shown on the events in figure 3.3. The thrust values for those events are 0.96 and 0.82,

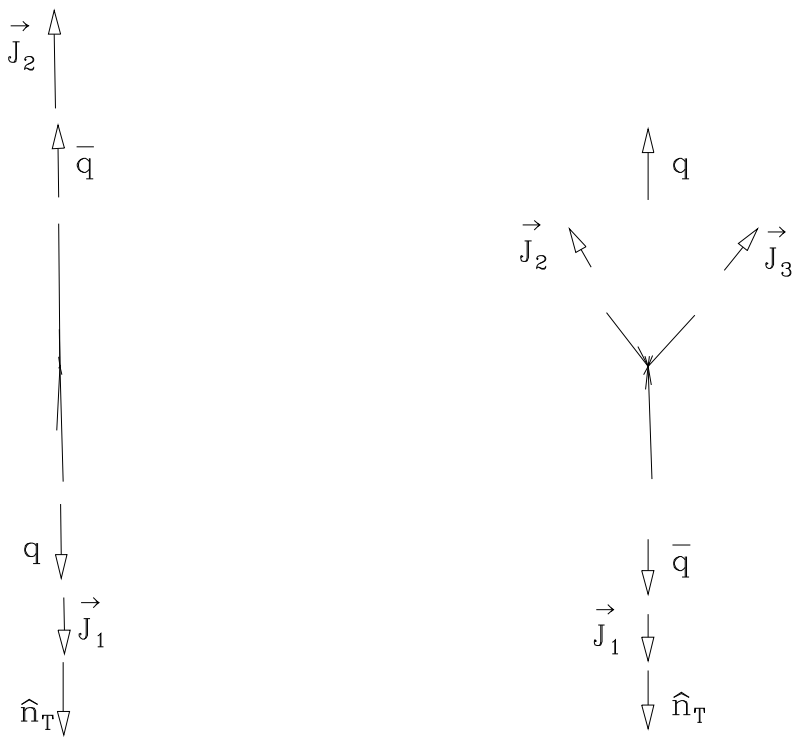

Fig. 3.3: Momentum vectors of the quarks and gluons after the parton shower in 2 sample events. In (a) there is only low energy and collinear gluon radiation. In (b) there is high energy, acollinear gluon radiation which perturbs the quark direction. The original quark and antiquark directions, q and $\bar{q}$, the thrust direction, $\hat{\mathbf{n}}_T$, and the jet directions, $\vec{\mathbf{J}}$, are shown with arrows.

respectively. The thrust is lower in the second event because of the transverse momentum introduced by the hard gluon.

An advantage of the thrust method is that it washes out the effect of any hard gluons and returns the original $q\bar{q}$ direction. Notice that even in the 3 jet event of figure 3.3(b), the thrust axis still lines up with the original quark direction. In addition, thrust depends linearly on momentum while other methods depend on the square of the momentum. As a result, thrust is less sensitive to errors in momentum measurement. A disadvantage is that it does not give much information about any gluon radiation.

The jet clustering method provides information about the number of jets and their momentum so that gluon jets can be discerned and measured. The JADE

jet clustering algorithm is used.[17] In that algorithm, the scaled mass squared is calculated for each pair of particles, i and j. It is defined as $y_{ij} \equiv (m_{ij}/E_{vis})^2$, where $m_{ij}^2 = 2E_iE_j(1-\cos\theta_{ij})$, and E_{vis} is the total visible energy in the event. The particle pair with the smallest y_{ij} is replaced by a single cluster which has the combined four momenta of the two particles. The y_{ij}'s are then recalculated for the new configuration and the process iterates until there are no more pairs of particles or clusters which have y less than some cutoff parameter called y_{cut}.[18] The resulting clusters are the jets, and each corresponds to a quark, antiquark, or gluon with their momentum specified by the momentum of the cluster. The event shown in figure 3.3(a) has two jets. The event in figure 3.3(b) has three jets with the third jet coming from the radiated gluon. The momentum vectors for the jets are indicated in the figure.

The advantage of the jet clustering method is that it can determine if there is hard gluon radiation and then find its momentum vector. Disadvantages are that it can be sensitive to the chosen value of the parameter y_{cut}, and it can be difficult to determine which jet is the unperturbed quark jet if there are 3 or more jets.

To measure the forward-backward asymmetry, only the original quark directions are needed, not the directions of any gluon jets. Because of that, the thrust method is used for reconstruction of the quark directions. The jet clustering method is only used in the minor role of determining if there is a gluon jet. This is of interest for verification that hard gluon radiation does not alter the asymmetry. The performance of the thrust method will be described in the next section after the remaining fragmentation effects are included.

3.3 Fragmentation

The second phase of hadronization is the fragmentation of the partons into hadrons. This is modelled independently from the subsequent decay phase, but it is convenient to lump them together here, and then to treat the special aspects of decay separately. The Monte Carlo program implements the string fragmentation

model to produce a list of final state particles with information such as particle type, charge, and momentum included. The goal is to extract the original quark and antiquark directions from this information.

3.3.1 Determination of the $q\bar{q}$ direction

Since the fragmentation process is soft, the overall structure of the event survives mostly unchanged. For example, figure 3.4 shows the same two events as figure 3.3, but after fragmentation and decay. This time, the thrust axis and jet axes were calculated using the momentum of the final state particles instead of the partons. Even though there are many more particles than partons, the thrust and jet directions are only slightly changed.

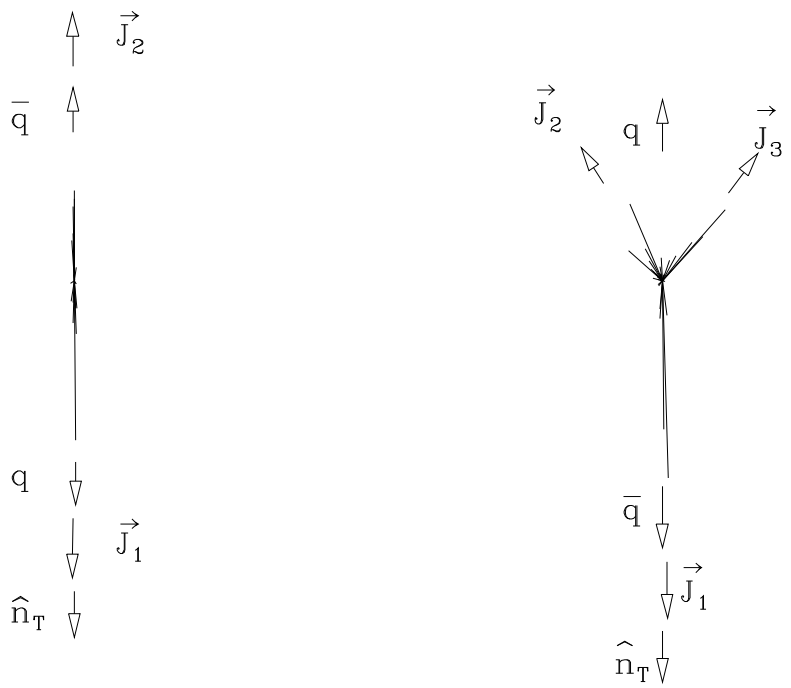

Fig. 3.4: Momentum vectors of the final state particles in 2 sample events. The events are the same as in figure 3.3. The original quark and antiquark directions, q and $\bar{q}$, the thrust direction, $\hat{\mathbf{n}}_T$, and the jet directions, $\vec{\mathbf{J}}$, are shown with arrows.

The thrust axis continues to be a good tool for extracting the quark direction even after fragmentation. Its performance can be determined by comparing the thrust direction with the quark direction in a large sample of Monte Carlo events. This is done in figure 3.5 by plotting the distribution of the angular difference between the $q\bar{q}$ direction and the thrust direction. The figure shows that the thrust axis matches the quark direction to within 5° for 80% of the events but has a very long tail. The same thing can be done using the jet clustering algorithm, and the results are similar, but only if the jet direction that is *closest* to the quark is used. However, in the experimental data, it is not always easy to tell which jet is closest to the quark if there are more than 2 jets.

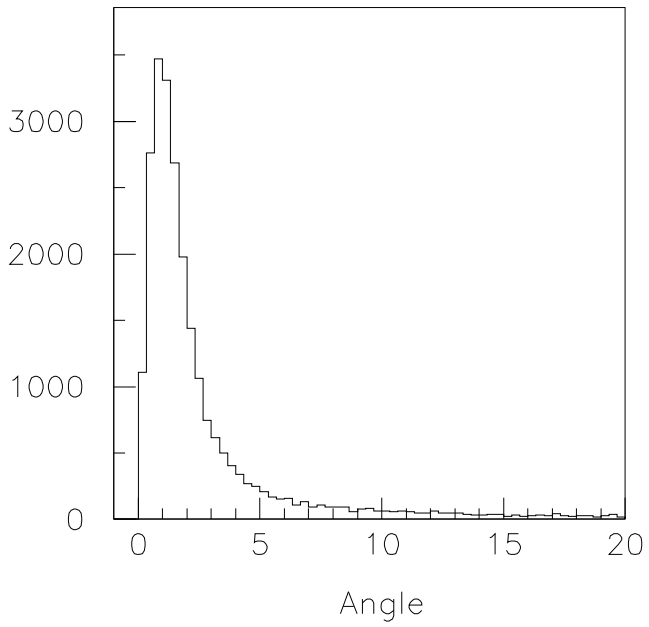

Fig. 3.5: Distribution of the angle between the quark direction and the thrust direction (in degrees).

To understand the long tail in figure 3.5, it is useful to look at the distribution of the thrust values. This is shown in figure 3.6(a), and it is peaked toward high thrust. This occurs because the quark and antiquark have high momentum while

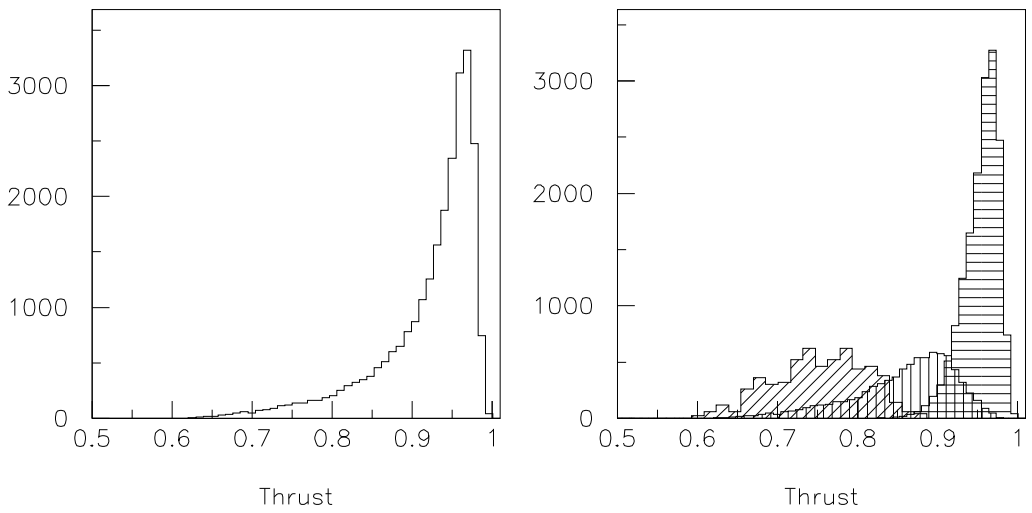

Fig. 3.6: Distribution of the thrust values. (a) contains all events. (b) shows separate distributions for events with 2, 3, and 4 jets. Horizontal hatching is used for 2 jet events, vertical hatching is used for 3 jet events, and diagonal hatching is used for 4 jet events. Due to the low number of 4 jet events, the histogram showing 4 jet events has coarser binning and has been multiplied by 25.

the fragmentation is soft, causing all the final state particles to be swept along the original quark or antiquark direction to produce two narrow, back-to-back jets. However, if a hard gluon was radiated in the parton shower, then some particles are swept along the gluon direction to form a third jet. The resulting transverse momentum causes a lower thrust value. Figure 3.6(b) shows this by plotting the thrust distribution for events with 2, 3, and 4 jets separately. Notice that there are some 3 jet events which have rather high thrust. These come from the gluon jet being low energy or only slightly acollinear with the other jets. There are also 3 jet events which have very low thrust. These are events where the gluon carries away about half of the quark momentum and is highly acollinear. Such events are the cause of the long tail in figure 3.5 since the thrust axis can line up with the high energy gluon jet instead of the quark jet.

This difficulty with high energy gluon jets is further demonstrated in figure 3.7 which plots the angular difference between the quark and thrust directions for

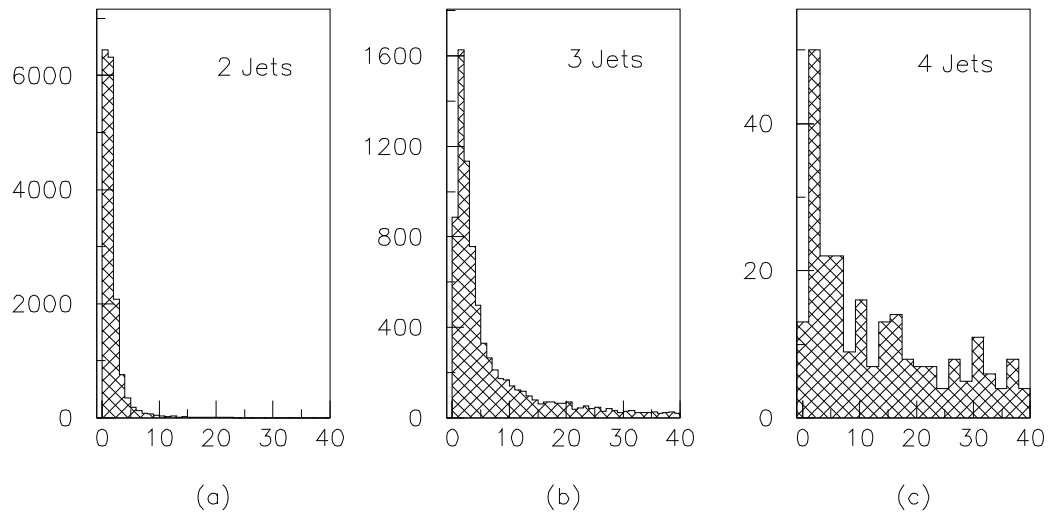

Fig. 3.7: Distribution of the angle between the quark direction and the thrust direction (in degrees) for events with 2, 3, and 4 jets. The thrust axis matches the quark direction well in 2 jet events and some 3 jet events, but it does not match in 4 jet events.

events with different numbers of jets. It shows that in 4 jet events the thrust direction does not match the quark direction well. Because of this, 4 jet events are not used.

The thrust axis can be both good and bad in 3 jet events, so a better way to look at it is to plot the angular difference as a function of the thrust value. Figure 3.8 shows that the thrust axis does not perform well in events with low thrust. Recall that some, but not all, 3 jet events have low thrust. It is these low thrust events which cause the long tail in figure 3.5(b). Because of this, events with low thrust (say $T < 0.8$)[19] are discarded. For the remaining events, the thrust axis matches the quark direction to within 5° for 88% of the events, and is within 10° for 95% of the events. This makes the thrust axis a good tool for determining the original $q\bar{q}$ direction.

3.3.2 Jet charge

The thrust method provides a single direction, $\hat{\mathbf{n}}_T$. Since the q and $\bar{q}$ are

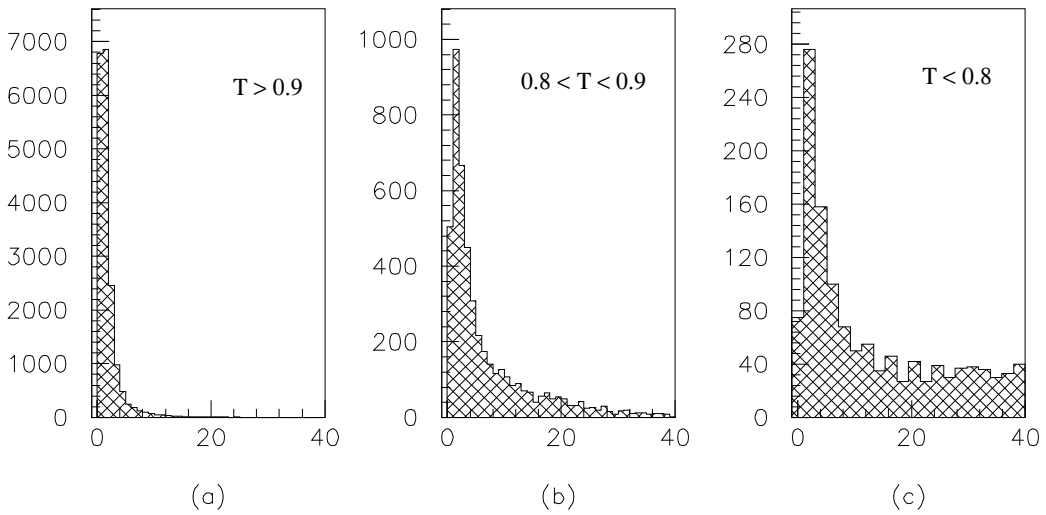

Fig. 3.8: Distribution of the angle between the quark direction and the thrust direction in degrees for events with various thrust values. The thrust axis matches the quark direction well if the thrust value is high.

back-to-back, $\hat{\mathbf{n}}_T$ is sufficient to specify both their directions. I.e., either $\hat{\mathbf{n}}_T$ is the q direction and $-\hat{\mathbf{n}}_T$ is the $\bar{q}$ direction, or $\hat{\mathbf{n}}_T$ is the $\bar{q}$ direction and $-\hat{\mathbf{n}}_T$ is the q direction. The thrust axis does not distinguish between these two cases. Recall that the asymmetry was defined with respect to the quark direction, so the asymmetry of the antiquark direction has the *opposite* sign. Because of this, it is necessary to distinguish between the two cases mentioned above. This amounts to distinguishing between the quark and the antiquark. The only measurable difference between them is that they have opposite electric charge, so that is the handle which must be used. Therefore, differentiating between the quark and antiquark requires measuring the sign of the electric charge of the resulting jets.

While fragmentation does not have a large effect on the direction information of the q and $\bar{q}$, it does have a large effect on the charge because charge is quantized. (The q and $\bar{q}$ have fractional charge, and the final state particles have integer charge.) This makes $q\bar{q}$ separation difficult.

An initial approach to determine the jet charge is to simply sum the charges of all the particles in each jet. (Note that the term *jet* is used loosely here. The

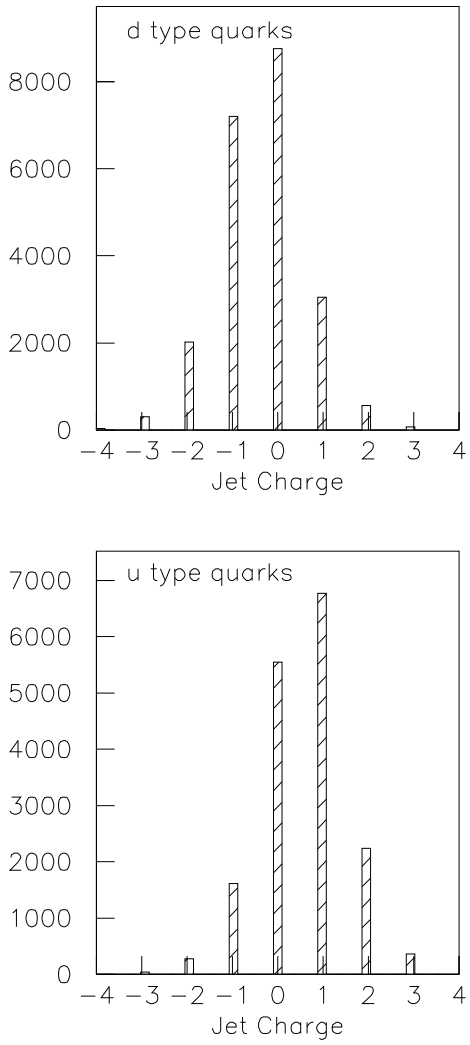

Fig. 3.9: Distribution of the quark jet charge. (Jet charges calculated by summing the particles' charges.) u type (u or c) and d type (d, s, or b) events are shown separately.

jet clustering method is not used. Rather, the plane normal to the thrust axis is used to divide the event into two hemispheres. These hemispheres are referred to as jets. When jet clustering is involved, it will be explicitly stated.) The results of the jet charge sum are shown in figure 3.9, and they are not very good. Many of the events have neutral jets and therefore give no information. As a result, the sign of the charge can only be determined correctly in 55% of u and c events, and

in 43% of d, s, and b events. The rest of the events are either incorrectly identified or indeterminate.

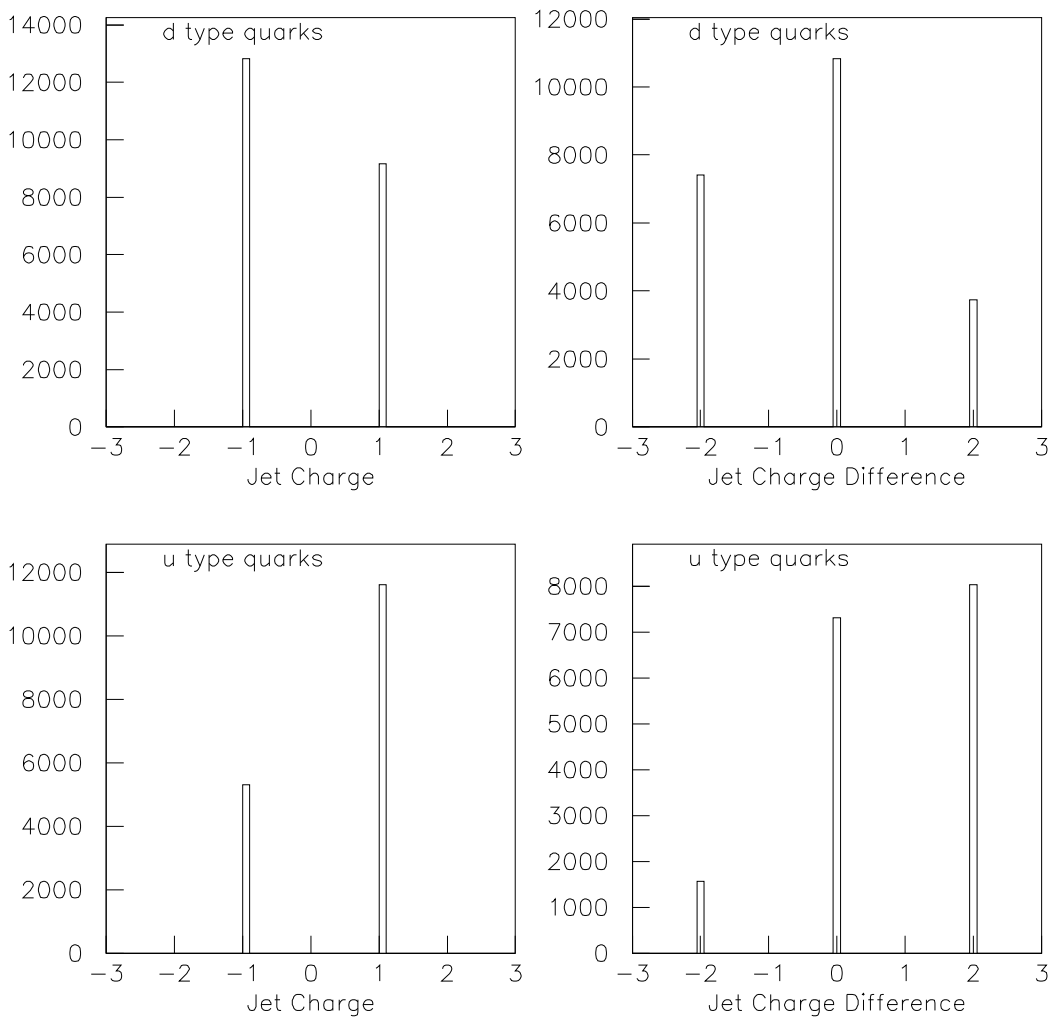

Fig. 3.10: Distribution of the quark jet charge calculated using the leading particle method. The right hand plots show the difference between the quark jet's charge and the antiquark jet's charge, indicating that there are many events for which the two jets have equal charge.

An alternative method is to use the charge of the highest momentum charged particle in the jet. This is called the *leading particle method*, and it relies on the assumption that the soft particles in the jet come from the soft fragmentation,

while the leading (i.e., highest momentum) particle comes from the original quark. The results with this method are slightly better and are shown in figure 3.10. The sign of the jet charge is correctly identified in 68% of u type and in 58% of d type jets. However, there are many events for which the q and $\bar{q}$ jets have the same charge so that although one jet is correctly identified, it is impossible to tell which one is correct and which is incorrect. Such events would have to be cut, drastically reducing the data sample.

It is, however, somewhat arbitrary to use only the leading particle since there are often several particles with high momentum. A better approach would be to include all the particles but to weight each particle's contribution by it's momentum. This weighting lessens the effect of softer particles. This method is called the momentum weighting method, and was inspired by Field and Feynman.[20] It defines the charge of a jet as

$$Q_{jet} \equiv \frac{\sum_{i=1}^{N} q_i |\vec{p}_i|^{\kappa}}{\sum_{i=1}^{N} |\vec{p}_i|^{\kappa}} \tag{3.3}$$

where the sums run over all the particles in the jet, q_i is the charge of the i^{th} particle in the jet, and $|\vec{p}_i|$ is its momentum. κ is a parameter which can be varied to change the strength of the weighting. It is interesting to note that in the limit $\kappa = 0$, the momentum weighting method reduces to the initial charge sum method, and in the limit $\kappa \to \infty$, it reduces to the leading particle method. (It is also possible to use a rapidity weighted charge sum. This option is discussed in the Appendix.)

This definition amounts to a momentum weighted average of the particle charge, and so it is no longer quantized like the charge sum or leading particle method. Figure 3.11 shows the jet charge distributions for u type and d type quarks with $\kappa = \frac{1}{2}$. The performance of this method is rather good. The sign of the charge is determined correctly in 74% of the u jets, and in 69% of the d jets.

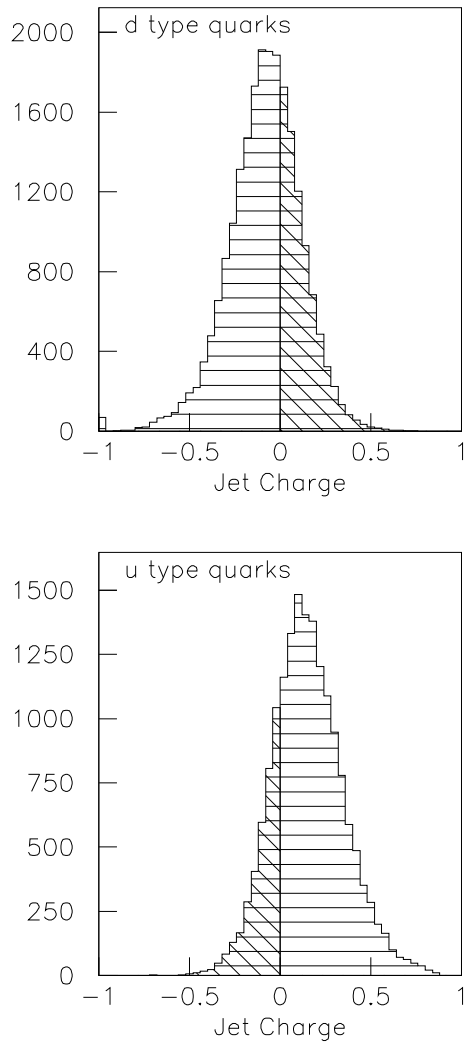

Fig. 3.11: Distribution of the momentum weighted jet charge. u type (u or c) and d type (d, s, or b) events are shown separately. The diagonally hatched regions correspond to incorrectly identified jet charge.

Since the goal is to differentiate between the q and $\bar{q}$, all that is necessary is to determine which of the jets is the *more* positively charged jet. Because of that, it is better to look at the charge *difference* between the two jets, and to define the positive jet as the one with the largest charge, even if that charge happens to be negative. For example, if $Q_1 = -0.1$ and $Q_2 = -0.5$, then jet 1 is the positive jet. This improves the percentage of correctly identified events to 80% for u-type,

and 74% for d-type. The charge difference, ΔQ, is plotted for u-type and d-type quarks in figure 3.12.

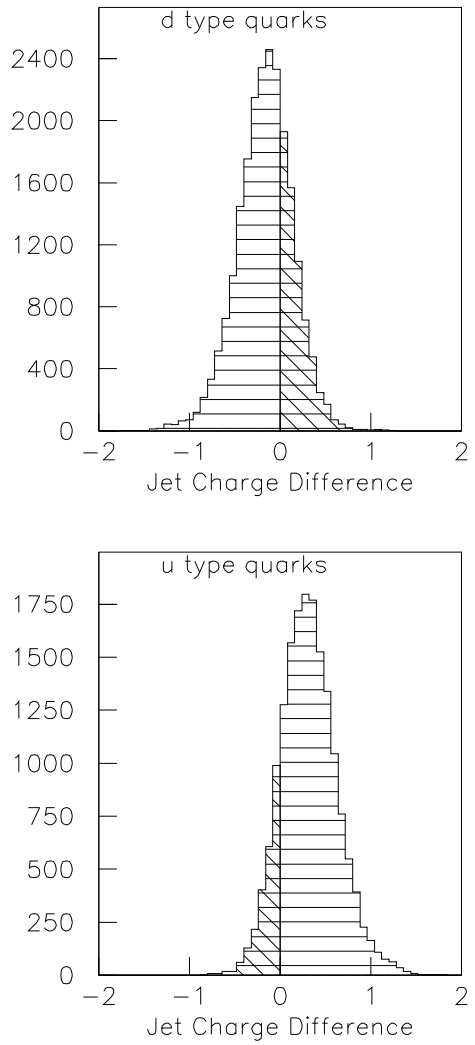

Fig. 3.12: Distribution of the momentum weighted jet charge difference, ΔQ. u type (u or c) and d type (d, s, or b) events are shown separately. The diagonally hatched regions correspond to incorrectly identified jet charge.

The momentum weighting method performs rather well, but it is not perfect. In fact, it is not possible to find a perfect method. There will always be some

events for which the jet charge is incorrectly identified. Therefore, it is necessary to determine what effect these incorrect events will have on the asymmetry measurement. This can be done by recalling the definition of the asymmetry from Eq. (2.8).

$$A_q \equiv \frac{\sigma_{|\cos\theta_q>0} - \sigma_{|\cos\theta_q<0}}{\sigma_{|\cos\theta_q>0} + \sigma_{|\cos\theta_q<0}}.$$

Since the cross section is related to the number of events by the luminosity, $N = \sigma L$, the asymmetry can be rewritten in terms of the number of events in the forward and backward directions;

$$A_q = \frac{N_F - N_B}{N_F + N_B}.$$

Misidentifying the jet charge corresponds to inverting an event from the forward region to the backward region, or vice versa. If P_q is defined as the fraction of correctly identified events, then the number of events *measured* to be in the forward and backward directions are $N'_F = P_q N_F + (1 - P_q)N_B$ and $N'_B = P_q N_B + (1 - P_q)N_F$. The measured asymmetry is then

$$A'_q = \frac{N'_F - N'_B}{N'_F + N'_B} = (2P_q - 1)A_q. \tag{3.4}$$

For example, if $P_q = 80\%$, then the measured asymmetry is only 60% of the actual asymmetry, so misidentification of the q and $\bar{q}$ charge causes the asymmetry to decrease significantly, and it is therefore important to try improving the jet charge method.

One way to improve the jet charge method is to vary the weighting factor, κ, and find the κ value which gives the largest P for Monte Carlo data. To that end, figure 3.13 plots P as a function of κ for all quark flavors combined. The maximum value of P occurs at a κ of about 0.5, which is why that value was used above.[33]

Another way to improve the jet charge method is to discard events for which ΔQ is small. The positive jet is defined as the jet with the largest charge, but if the

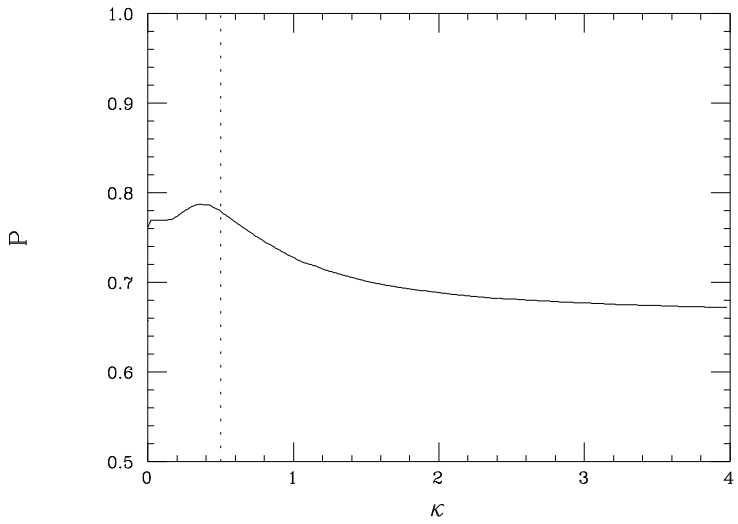

Fig. 3.13: Fraction of events with correctly identified jet charge as a function of the momentum weighting, κ for all quark flavors combined. A dotted line is drawn at $\kappa = \frac{1}{2}$.

jet charges are nearly equal then it is rather arbitrary to claim that one is actually larger than the other. So, such events are discarded by requiring a minimum charge difference between the two jets, ΔQ_{min}. From figure 3.12, it is apparent that a ΔQ_{min} value of 0.5 would discard most of the incorrectly identified events and so give a very high value of P, but it would also discard many correctly identified events and so increase the statistical error on the asymmetry measurement by reducing the number of events. So, the ΔQ_{min} value is not chosen to maximize P, but rather to maximize the significance of P i.e., $\frac{P}{\delta P}$. Determining the best value for ΔQ_{min} will be put off until after the detector effects have been incorporated. For now, it is sufficient to say that the fraction of events with correctly identified jet charge can be made high so that the quark and antiquark jets can be separated with rather good purity.

3.3.3 Flavor

The thrust axis provides a good measure of the $q\bar{q}$ direction, and the momentum weighted, average charge allows identification of the positively charged jet. However, there is no easy way to determine the flavor of an event. There are some methods, but they have low efficiency and are only applicable to heavy flavors.

Because of this, all the flavors are combined and the total *hadronic* asymmetry is measured. It is not just a sum of the asymmetries of the individual flavors because the u type and d type quarks have different electric charge. Recall that the asymmetry was defined with respect to the quark direction, but as discussed in the previous section it is not possible to determine the quark direction, so the positive charge direction is used instead. The production direction is defined with respect to electric charge by using the angle between the incoming positive charge (the positron) and the outgoing positive charge (the u or c quark or the d, s, or b *anti*quark). Because of this charge dependence, the quantity measured is called the hadronic *charge* asymmetry, A_h. Due to their charge, u type quarks contribute with opposite sign, so the hadronic charge asymmetry is related to the electroweak asymmetries of the individual flavors by

$$A_h = A_d - A_u + A_s - A_c + A_b. \tag{3.5}$$

At energies around $60GeV$, $A_u = A_c \approx -51\%$ and $A_d = A_s = A_b \approx -58\%$. As shown in section 2.1, the production rate for u type quarks is greater than for d type quarks by a factor of 2.5, so the u and c contribute to A_h more than the other quarks do. As a result, $A_h \approx +9.5\%$ at $60GeV$. The value of A_h is shown as a function of energy by the dashed curve in figure 3.14.

The asymmetry in Eq. 3.5 is modified by the misidentification of jet charge as was shown in Eq. 3.4, so that

$$A_h = (2P_d - 1)A_d - (2P_u - 1)A_u + (2P_s - 1)A_s - (2P_c - 1)A_c + (2P_b - 1)A_b. \tag{3.6}$$

The value of A_h including these misidentification factors is shown as a function of

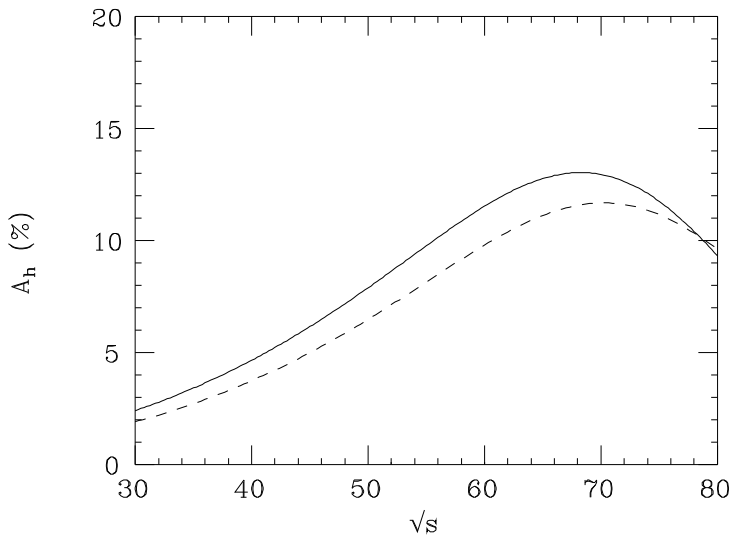

Fig. 3.14: Hadronic charge asymmetry versus center of mass energy. The dashed curve does not include misidentification effects while the solid curve does.

energy by the solid curve in figure 3.14. Notice that it is slightly larger than what is predicted without including charge misidentification. This increase is caused by the fact that P is larger for u-type quarks than for d-type quarks. As a result, the misidentification factors reduce the negative contribution to the asymmetry sum more than they reduce the positive contribution, and thereby increase the total asymmetry.

This section has shown how the required information about the original quark and antiquark is extracted from the final state particles. The direction information can be determined using the thrust method, and the positive and negative jets can be distinguished by using a momentum weighted, average charge. But, the flavor of the original $q\bar{q}$ pair cannot be determined. So, the *total* hadronic charge asymmetry is measured. It is the asymmetry of all quark flavors combined with the direction defined by the positively charged jet.

3.4 Prompt decay of heavy hadrons

The decay of heavy hadrons has some effects of its own on the determination of the original quark information. It introduces more transverse momentum to the jets and therefore it can degrade the performance of the thrust and jet charge methods. In addition, some particular decay channels can have unusual effects on the jet charge. These effects are mostly limited to the heavy flavors so it is possible to use them to study the behavior of individual flavors.[21]

From a purely kinematical point of view, decays decrease the thrust of a jet by imparting transverse momentum to the decay products. Since the jet energy is high, the effect is only important in heavy flavors. For example, B mesons have $m_B = 5GeV$ which is a large fraction of the jet energy, $E_{jet} \approx 30GeV$. So the decay products of the B can have substantial transverse momentum. On the other hand, mesons made from the light quarks have masses less than a GeV so their decay products do not have substantial transverse momentum. The extra transverse momentum in heavy flavors widens the jets and therefore has the potential for deteriorating the thrust and charge information. However, the effect is much smaller than the widening from gluon radiation, so it does not introduce any new difficulties.

A more interesting effect arises from the richness of fragmentation and decay channels that each flavor has available. These different channels can lead to some interesting effects on the jet charge. The string fragmentation typically results in between 10 and 20 hadrons. Many of these decay before detection so that the final state particles consist mostly of $\pi^{\pm}$, $K^{\pm}$, and γ. The spectrum of final state particles depends significantly on what the post-fragmentation hadrons are and which decay channels they choose.

The types of hadrons resulting from fragmentation depend on how the fragmentation proceeds. When a string breaks and produces a $q\bar{q}$ pair, the new pair can be of any flavor. It is equally likely to produce u or d quarks, but s quarks are suppressed by about $\frac{1}{3}$. Production of heavier quarks is highly suppressed due to

their large masses, so they are neglected. With this in mind, look at figure 3.15. It shows the different mesons which can be produced in the fragmentation of a u quark depending upon the flavor of the secondary $q\bar{q}$ pairs. Only the first two mesons are shown. There are more, of course, but only the first two are needed for the purpose of this illustration. Also, the suppressed $s\bar{s}$ pairs are allowed only in the first branching to keep the diagram simple. Notice that the post-fragmentation hadrons can differ widely depending upon what flavor was chosen for the new $q\bar{q}$ pairs.

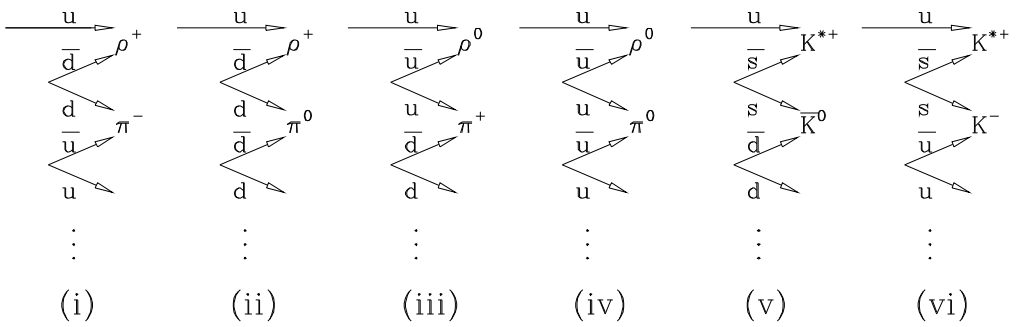

Fig. 3.15: Four fragmentation possibilities for a u quark showing the different mesons produced. The primary meson is usually an excited state, such as a ρ instead of a π, or a K^* instead of a K.

Cases (*ii*), (*iii*), and (*v*) have a positively charged particle as the leading meson and a neutral particle as the secondary meson, so they are a likely to have their jet charge correctly identified. Cases (*i* and *vi*) have positively and negatively charged particles, so they are less likely to have their jet charge correctly identified. But, in case (*iv*) both of the high momentum particles are neutral so it will be difficult to identify the charge.

The ρ^0 and π^0 in case (*iv*) are unstable and quickly decay. The π^0 goes to two photons. The ρ^0 goes to a π^+ and a π^-, and it is equally likely to have the $+$ or the $-$ end up as the leading particle. As a result, the charge of the leading particle is not expected to be a good indicator of jet charge in such events. Expressed in the framework of the momentum weighted jet charge, this means that the charge

determination efficiency, P, will drop as the momentum weighting, κ, increases (recall that large κ means that the leading particles are more heavily weighted). For example, in u events with a leading ρ^0, P_u drops from 83% at $\kappa = 0.5$ to 63% at $\kappa = 2.0$. By comparison, in events with a leading ρ^+, $P_u(\kappa = 0.5) = 87\%$ and $P_u(\kappa = 2) = 82\%$. One of the reasons that the jet charge is easy to identify in u quarks is that their fragmentation is soft resulting in several particles of nearly equal momentum instead of one or two leading particles. So, in the $\rho^0 \rightarrow \pi^+\pi^-$ case, even if the π^- ends up as leading, its momentum is not too much greater than the other particles. That is why $P_u(\kappa = 0.5)$ is high even in events with a ρ^0 as the primary meson.

A figure similar to figure 3.15 could be drawn for each flavor to determine the leading mesons. The two most primary mesons that result are listed in the table below.

Flavor	(i)	(ii)	(iii)	(iv)	(v)	(vi)
u	$\rho^+ \ \pi^-$	$\rho^+ \ \pi^0$	$\rho^0 \ \pi^+$	$\rho^0 \ \pi^0$	$K^{*+} \ \bar{K}^0$	$K^{*+} \ K^-$
d	$\rho^0 \ \pi^-$	$\rho^0 \ \pi^0$	$\rho^- \ \pi^+$	$\rho^- \ \pi^0$	$K^{*0} \ \bar{K}^0$	$K^{*0} \ K^-$
s	$\bar{K}^{*0} \ \pi^-$	$\bar{K}^{*0} \ \pi^0$	$K^{*-} \ \pi^+$	$K^{*-} \ \pi^0$	$\phi^0 \ \bar{K}^0$	$\phi^0 \ K^-$
c	$D^{*+} \ \pi^-$	$D^{*+} \ \pi^0$	$D^{*0} \ \pi^+$	$D^{*0} \ \pi^0$	$D_s^{*+} \ \bar{K}^0$	$D_s^{*+} \ K^-$
b	$\bar{B}^0 \ \pi^-$	$\bar{B}^0 \ \pi^0$	$B^- \ \pi^+$	$B^- \ \pi^0$	$\bar{B}_s^0 \ \bar{K}^0$	$\bar{B}_s^0 \ K^-$

Table 3.1: List of the leading mesons typically produced in the fragmentation of each quark flavor.

The table shows that d quarks have more neutral and wrong sign leading mesons than u quarks. This makes P_d considerably lower than P_u for all values of κ. This is compounded by the decays of the leading mesons. For example, the K^- in case (*vi*) does not decay quickly, so it appears as a high momentum negatively charged particle which makes charge determination easy. But, the ρ^- in case (*iii*)

decays to $\pi^-\pi^0$. The π^- ends up with relatively low momentum compared to the primary π^+, so the jet charge is dominated by the π^+.

s quarks are similar to d quarks, but perform slightly better. The primary mesons formed by s quarks are mostly K^-'s and $\bar{K}^0$'s. The K^-'s do not decay within the detector, so they allow easy charge determination and make P_s a bit higher than P_d.

The light quarks have soft fragmentation, so the mesons tend to be low energy. The heavy quarks, however, have harder fragmentation. The D and B mesons produced from c and b quarks tend to have a large fraction of the total momentum, typically more than 70%. As a result, leading particle effects are much more pronounced in heavy quarks.

c quarks have the same problem with neutral primary mesons as the light quarks, but it is exaggerated since the $+$ and $-$ particles resulting from the meson's decay have much higher momentum than the remainder of the particles, and because of the flavor cascade nature of its decays. D's decay to K's because of the $c \to s$ cascade. In particular, D^+'s decay to K^0's and D^0's decay to K^-'s because the $c \to s$ cascade changes a $+\frac{2}{3}$ charge quark into a $-\frac{1}{3}$ charge quark by radiating a W^+. The strange meson retains most of the energy, so it is leading. For example, the decay $D^0 \to K^-\pi^+$ tends to give more energy to the K^-, so the leading particle is *negatively* charged! In events with that decay chain, P_c actually falls below $\frac{1}{2}$ if a large κ is used. These cascade decays cause P_c to fall sharply as κ is increased.

Furthermore, P_c is reduced by the fact that most of the D^+'s produced in cases (i) and (ii) are excited states (i.e., D^{*+}'s). 40% of the time, these decay to $D^0\pi^+$, and the π^+ has very low momentum. This effectively throws away the charge information and makes jet charge determination difficult.

The mesons produced by b quarks also undergo cascade decays through $b \to c \to s$. The B^-'s decay to D^0's and the B^0's decay to D^+'s via a W. The W then decays to π^-, ρ^-, e^-, or μ^-. As in the c case, the D's have higher momentum

than the W's, but the D's also decay (with the same decay schemes described above). The result is a medium momentum negatively charged particle from the W decay, along with the medium momentum positive and negative particles from the D decay giving a net negative jet charge. This can also be seen by looking at the quark cascade. The negative b decays to a positive c which then decays to a negative s. The final result is a negatively charged quark. So, P is higher in b events than in the other down type events. In fact, P_b is higher than even P_c for large values of κ.

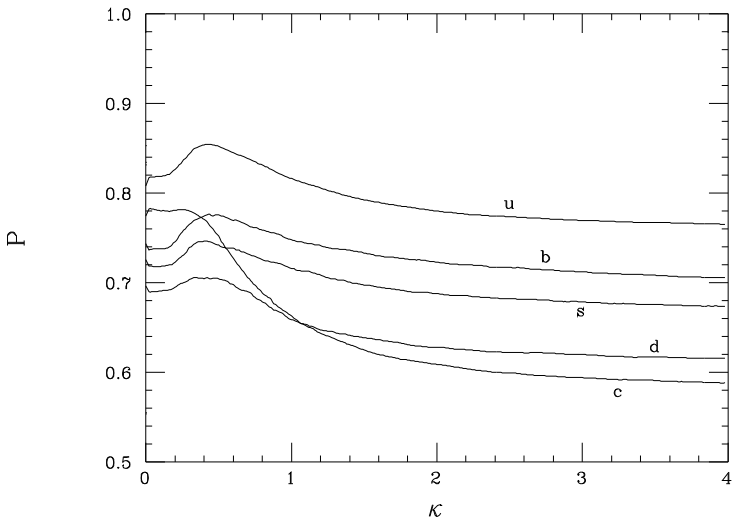

Fig. 3.16: Charge determination efficiency as a function of momentum weighting for each flavor in generated data. Notice how the charge determination deteriorates at high κ for all flavors, and is particularly bad in c quarks.

Figure 3.16 summarizes all of this by plotting P_q as a function of κ for each of the quark flavors. Notice that each flavor exhibits a decrease in P as κ becomes large, but that the effect is most pronounced in P_c as expected from the decays of D mesons. Also notice that the P's are near maximum at $\kappa = 0.5$. The corresponding values are listed in Table 3.2

The decay effects described above cause P_c to be lower than P_u and they also cause P_b to be higher than P_d. These effects combine to decrease the asymmetry

Flavor	u	d	s	c	b
P_q	$85.2 \pm 0.8\%$	$70.4 \pm 1.2\%$	$74.2 \pm 1.2\%$	$75.2 \pm 0.7\%$	$77.6 \pm 1.3\%$

Table 3.2: Performance of the momentum weighted jet charge method in generated data, for each flavor, using $\kappa = 0.5$. The uncertainties are statistical only, limited by the size of the generated data sample which was used.

sum, A_h, since the (positive) c contribution is reduced by the small $2P_c - 1$ factor while the (negative) b contribution is less reduced by the slightly larger $2P_b - 1$ factor.

To summarize, this chapter has described the effects of fragmentation and decay on the determination of the original quark information. The thrust axis is used as a measure of the direction of the original quark. A momentum weighted charge sum is used as a measure of the charge of the original quark. The flavor of the original quark cannot be determined so all the flavors are combined, and the production direction is defined as the positively charged direction.

It is important to note that all the effects described thus far result from quark fragmentation, *not* from measurement errors. Up until now, it has been assumed that all the final state particles are detected and their momentum is measured accurately. In reality, of course, some particles are lost, and the momentum measurements are not always accurate. These measurement errors will have effects of their own which must be understood. The next chapters describe the detector, its limitations, and what effect they have on the measurement.

4. AMY

The measurement was performed with the AMY detector at the TRISTAN collider in Japan.

4.1 TRISTAN

TRISTAN is an e^+e^- collider at the National Laboratory for High Energy Physics (KEK) in Tsukuba, Japan. Its construction began in 1982, and it began operating at the end of 1986 at a center of mass energy of $\sqrt{s} = 50GeV$. During the next several years, superconducting rf (accelerating) cavities were installed to progressively boost the energy. The peak energy achieved was $\sqrt{s} = 64GeV$. Since 1991, TRISTAN has been running at $\sqrt{s} = 58GeV$ with high luminosity provided by superconducting quadrupole (focussing) magnets at each interaction point.

A schematic diagram of TRISTAN[22] is shown in figure 4.1. The linear accelerator (LINAC) produces electron bunches with a width of 1.5ns and a current of $50mA$. These are accelerated down the $390m$ long LINAC to an energy of $2.5GeV$ and then injected into the accumulation ring (AR). The LINAC repeats the injection process every $20ms$, and the AR continues to accumulate the LINAC's bunches until it's beam current reaches about $20mA$. This takes about 30 seconds. The AR then accelerates its beam to $8GeV$ and injects it into the main ring (MR).

Positrons are produced by colliding a high current (10A) beam of $200MeV$ electrons into a tantalum target to produce electron-positron pairs. Positrons are extracted from the debris and accelerated down a separate $250MeV$ linac. They are then feed into the main LINAC and injected into the accumulation ring just as

Fig. 4.1: Schematic diagram of TRISTAN showing the main ring, accumulation ring, and linear accelerator.

the electrons were. Positron accumulation takes about ten times as long as electron accumulation due to the limits on positron production.

The main ring is $3km$ in diameter. It is not actually circular, but rather consists of four straight sections and four curved sections. The curved sections contain dipole bending magnets and tuning magnets. The straight sections contain rf accelerating cavities, quadrupole magnets, and the interaction points. During initial stages of running, only a minimal number of rf cavities were used. More were added later to boost the total energy to $60GeV$, and finally superconducting rf cavities were installed to raise the energy to $64GeV$. (In recent running, the energy was lowered to $58GeV$ to obtain higher luminosity.)

The main ring receives the AR's output into 2 bunches of electrons and 2 bunches of positrons. The electrons circulate clockwise, and the positrons circulate counter-clockwise (as viewed from above). The electron and positron bunches are timed so they cross at each of the four interaction points. The maximum beam

current attainable in the main ring is about $12mA$. Accumulating this current requires at least 8 injection cycles which typically takes 20 minutes. Once the full current is obtained, the beam energy is ramped to the full energy and the beams are brought into collision. While running in collision mode, the beam intensity decays exponentially with a lifetime of about an hour. So, after an hour or two of running, the beams are dumped and the injection process repeats.

4.2 The AMY detector

AMY is one of the three detectors on TRISTAN. Its design was optimized for lepton detection, and it has a strong magnetic field to precisely measure the momentum of charged particles.

Fig. 4.2: A cross-sectional diagram of the AMY detector. Only one quadrant is shown. The other 3 quadrants are identical.

A schematic diagram of AMY is shown in figure 4.2. There are two figures. The first shows the structure of AMY before 1989, and the second is the configuration after 1989. AMY consists of several subdetectors layered upon each other in

a cylindrical geometry. Starting from the interaction point and moving outward, these detectors are the vertex detector (VTX), the inner tracking chamber (ITC), the central drift chamber (CDC), the electromagnetic shower counter (SHW), and the muon chambers (MUO). All but the muon chambers are surrounded by a superconducting coil which provides a 3 Tesla magnetic field along the beam direction. Between the coil and the muon chambers is a thick iron mass which acts as a return for the magnetic flux, and also as a hadron absorber so that only muons penetrate the iron and are detected by the muon chambers. The end regions of the detector have had two incarnations. In early running, the ring veto counter (RVC), pole tip calorimeter (PTC), and luminosity monitor (LUM) covered the end regions. In 1989, these were replaced by the end cap shower counter (ESC), forward tracking chamber (FTC), and small angle counter (SAC). Each of the subdetectors will be described in turn.[23] I was involved in the vertex detector project, so I will describe it in much more detail than the other detectors.

The vertex detector

The vertex detector (VTX) was installed in 1991. At the same time, a smaller, $10cm$ diameter, beam pipe was installed. It has a $1mm$ thick beryllium wall to minimize multiple scattering. The VTX is designed to provide precise tracking very close to the interaction point in order to resolve the secondary vertices produced by the decay of heavy mesons from b and c quarks. This allows tagging of heavy quark events and measurement of the lifetimes of heavy mesons.

The VTX has an inner radius of $55mm$ which is only slightly larger than the beam pipe. Its outer radius is $75mm$. It's active region is $56cm$ in length so that it can cover angles down to 13 degrees. The chamber is constructed from 4 cylindrical layers of mylar straws with 80 straws per layer as shown in figure 4.3.[24] The straw diameters are $4.52mm$, $4.84mm$, $5.21mm$, and $5.58mm$ for the four layers. The internal walls of the straws are coated with a thin layer of aluminum which allows the walls of the straws to be held at ground potential. A fine wire, $20\mu m$ in diameter, is strung down the center of each straw and held at a high

voltage. This establishes a radially symmetric electric field gradient centered on the wire in each straw. A gas mixture of 89% argon, 10% CO_2, and 1% CH_4 is flowed through the straws and held at the highest possible pressure that the straws will allow.[25]

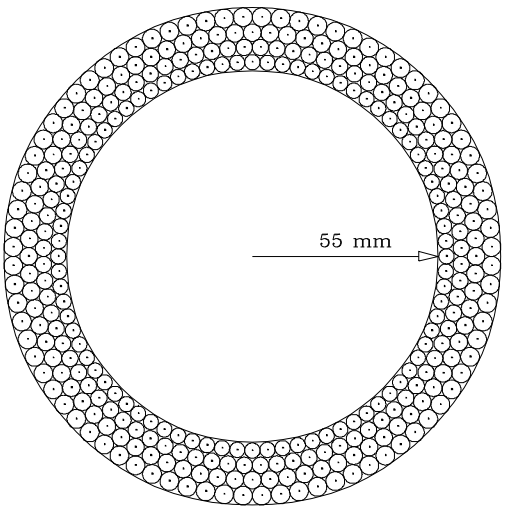

Fig. 4.3: A schematic diagram of the VTX. This is a "beam's eye" view i.e., looking along the beam direction.

The passage of a charged particle through a straw is detected because of the ionization left along the particle's path. In argon, a minimum ionizing particle produces typically 100 ions/cm. The electrons from these ions are then accelerated toward the central wire under the influence of the electric field. But before they get far, they collide with a gas molecule, give up most of their energy, and are accelerated again. Because of these collisions, the electrons follow a random path on a microscopic level, but on a macroscopic level they "slowly" drift in toward the wire at an approximately constant velocity of about $50\mu m/ns$.

The electric field increases as $\frac{1}{r}$, so when the drifting electrons get within about $100\mu m$ of the wire, they are accelerated so vigorously between collisions that the energy they gain is sufficient to ionize the molecule or atom with which

they collide. The extra electron liberated from the molecule also accelerates toward the wire and produces further ions of its own. This avalanche process continues until all the electrons arrive at the wire. In this way, the small number of electrons produced by the ionizing radiation are amplified several hundred thousand times. This is enough to induce a charge of several pC on the wire. With sensitive, low noise amplifiers, this charge can be detected.

The distance of closest approach between the traversing particle and the central wire is found by measuring the time between the passage of the particle and the arrival of the *first* electrons at the wire, and then dividing by the drift velocity. The time of the particle's passage can be accurately determined from the beam crossing timing signal provided by TRISTAN. The time of arrival of the first electrons at the wire is determined from the electronic signal resulting from the deposited charge. The passing particle leaves a *trail* of ions so in order to measure the position of *closest* approach, it is important to measure the time of the *first* avalanche of electrons. To achieve good resolution, this time measurement must be precise, the maximum allowable error is $\approx 1ns$[26]. An important contribution to this error is *diffusion* of the electrons as they drift through the gas. This can be minimized by using a gas which causes the minimum possible diffusion and by using the highest possible gas pressure[27]. Another important error comes from the discrimination time of the electronic signal. This is determined by the signal to noise level of the electronics. If the amplification of the gas avalanche is high, and the electronic noise level can be kept low, then the discriminator threshold used to trigger the timing can be set low enough to trigger on the first electrons in the avalanche. The design resolution of $50\mu m$ in the $r-\phi$ plane (i.e., closest approach) was achieved in a beam test.

The z position (i.e., along the wire) of the particle's path is determined by *charge division.* A resistive wire[28] is used, and the charge is measured from both ends of the wire. The ratio of the signal sizes at the two ends is proportional to the position along the wire at which the avalanche occurred. In a beam test, excellent z resolutions of about 1% of the wire length were obtained.

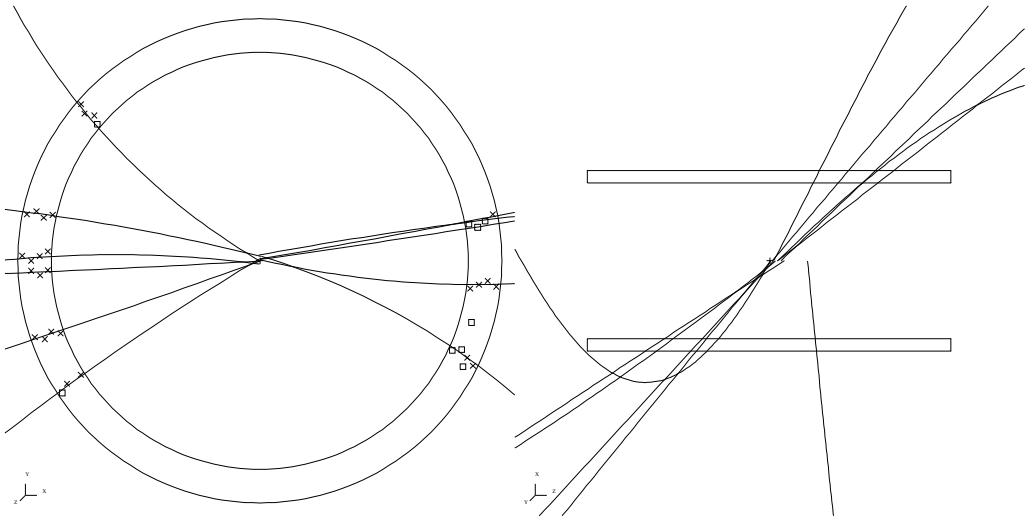

Fig. 4.4: A sample event in the VTX. The left hand figure is looking along the beam direction. The squares and x's show straws which were hit. The lines show the reconstructed tracks. The right hand figure is a cross sectional view showing the z position of the tracks. Notice that one track has been determined to be far from the interaction point in z.

The data from the VTX is not used in this thesis, but I was involved in designing and testing the electronics for the VTX so I will describe them in detail. The electronics for the VTX are shown schematically in figure 4.5.

Each layer has a separate high voltage supply. The HV is carried on coaxial cables from the "electronics hut" to a distribution box (D_1) which is outside AMY's end region, about 3 meters from the VTX. The distribution box distributes the HV onto independent wires, one for each straw, for the rest of the trip to the VTX. This allows any straw to be easily disconnected from HV in case it's anode wire breaks. There is a $1M\Omega$ current limiting resistor (R_1) for each straw to guard against damage from excessive current.

The charge signal is decoupled from the high voltage by a $2200pF$ capacitor (C_1) and fed into a preamplifier (A_1) which is mounted very close to the end of the straw on a small, surface mount circuit board. Each board holds the preamplifiers for 16 straws. The preamplifiers are charge sensitive with a voltage output of $10mV$ per μA of input. Each preamp contains a line driver to drive the output

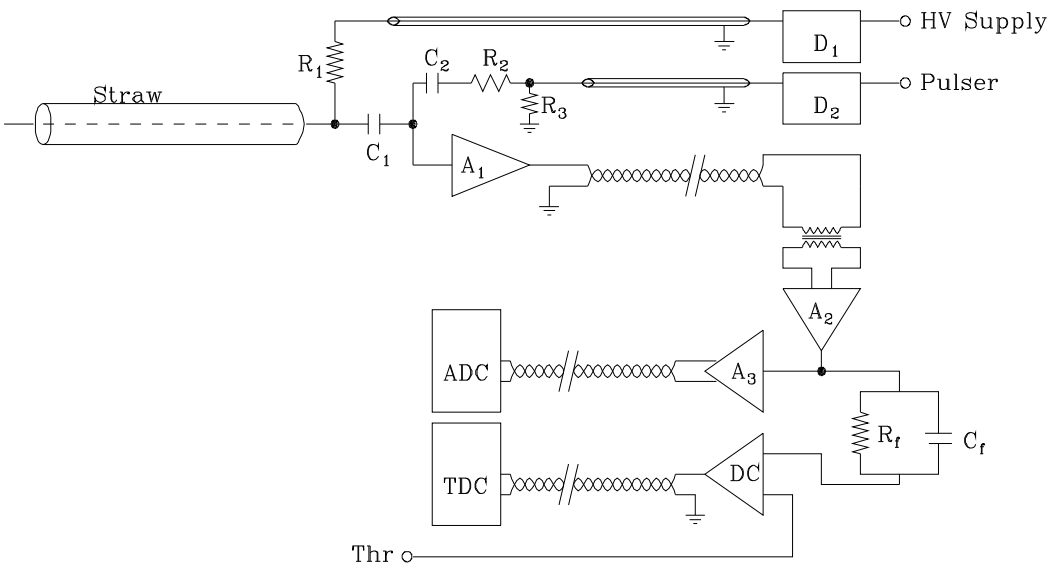

Fig. 4.5: A schematic diagram of the electronics used for the VTX. Only one side is shown. An identical electronics chain is used to readout the other end of the straw.

down twisted pair cable to an amp/discriminator card located just outside AMY's end region.

The amp/discriminator circuit is isolated from the preamplifier by an isolation transformer. The secondary coils of this transformer are fed into a differential operational amplifier (A_2). A video amplifier is used to provide a short rise time. The output of the video amp is then used for two separate purposes.

One half of the video amp's output is driven down a twisted pair by a line driver (A_3). The twisted pair runs for several tens of meters to a charge sensitive analog to digital converter (ADC) in the electronics hut.[29] The line driver actually provides some attenuation of the signal to prevent overflowing the ADC's range. The ADC measurement is compared to a similar measurement on the other end of the wire to determine the z position.

The other half of the video amp's output is run through a pole-zero filter which cancels the long tail (decay time) of the signal. This prevents the tail of one

signal from affecting the next signal. The signal is then compared to a threshold value with a discriminator (DC), and a logic signal is generated when the signal exceeds the threshold. The logic signal is transmitted on twisted pair cable to a time to digital converter (TDC) in the electronics hut. The timing of these logic signals provides a measurement of the drift time.

A pulser is used for testing and calibrating the electronics. The pulser's output is sent to a distribution box near AMY's end region (D_2). There it is divided and a separate signal is sent to each preamplifier card via coaxial cable. On the preamplifier card, there is a terminating resistor (R_3) which matches the cable's characteristic impedance, a capacitor (C_2) for each channel which differentiates the pulse to provide a charge input, and a shaping resistor (R_2) which makes the pulser shape simulate the VTX's signal shape. This pulsing system can be used to check for broken wires or damaged electronics, and to calibrate the electronic gain of each channel.

The inner tracking chamber

The inner tracking chamber (ITC) is similar to the VTX in construction. However, it is used mainly for triggering. The ITC occupies the annular region from $r = 122mm$ to $r = 142mm$, and $|z| \leq 275mm$. It consists of 4 layers of straw tubes with 144 straws per layer. The spatial resolution is $80\mu m$ in the $r - \phi$ plane. No z information is obtained.

Information from the ITC is not used in this thesis, but it is useful for triggering since it helps reject cosmic rays. The trigger decision is made by feeding the bit pattern of hit wires (i.e., 1 if the wire is hit, 0 if not) into a lookup table. If the patterns do not correspond to at least two tracks pointing back to the interaction point, then data acquisition cannot be triggered. This helps reject cosmic rays because the probability of a cosmic ray passing close to the interaction point is small.

The central drift chamber

The central drift chamber (CDC) is the heart of AMY. It tracks particles as they curve in the magnetic field and therefore provides a measurement of their direction, charge, and momentum. Due to the high magnetic field, the CDC could be made relatively compact. It extends from $r = 155mm$ to $r = 640mm$. The coverage along the beam increases with the radius. It is arranged as 6 concentric cylinders with lengths ranging from $93cm$ to $180cm$. The staggered design allows tracking of particles to within 37 degrees of the beam. This corresponds to a $\cos\theta$ coverage of $|\cos\theta| \leq 0.8$.

The $r - \phi$ resolution of each CDC wire is about $215\mu m$. The momentum resolution is $\frac{\Delta p_T}{p_T} \approx 1\% p_T$ for tracks with momentum near the beam energy. For lower momentum tracks, the resolution improves up to the limit imposed by multiple scattering i.e., $\frac{\Delta p_T}{p_T} \approx 0.3\% p_T$. The particles in quark jets are typically below a few GeV, so the momentum resolution for such particles is rather good. (Of course, only the component of momentum transverse to the magnetic field can be measured.)

The z component of each particle's trajectory is determined in the CDC by using *stereo wires*. These wires are strung at angles of 4.1 to 4.9 degrees from the beam direction. They provide θ information (i.e., z information) about the particle's trajectory with a resolution of ≈ 4 milliradians.

The large magnetic field introduces one difficulty. It causes low momentum charged particles to curl repeatedly within the CDC. These *curlers* cause problems in two ways. First, they produce hits in many cells of the CDC and therefore make those cells blind to other particles. Secondly, the tracking software can mistakenly identify a curler as more than one particle. Fortunately, they are low momentum, so they do not have a significant effect on the determination of thrust direction or charge.

The CDC provides the vast majority of the information needed for this thesis. The precise tracking and high magnetic field provide good direction and momentum

determination and make determining each particle's charge simple. However, this is strongly dependent upon the track recognition software's ability to recognize tracks from the CDC's data. The algorithm[30] used by the tracking software is designed to be fast since it will need to keep up with AMY's data acquisition trigger rate. This requires that an event be fully reconstructed in less than half of a second. To accomplish this without resorting to enormous computing power, the tracking algorithm takes advantage of the CDC's band structure i.e., the way that it is made of 6 concentric cylinders. Track segments are first found in each band and then these segments are linked into complete tracks. This drastically reduces the combinatorics compared to searching all the wires simultaneously. The track segments in a band are found by taking each hit in the innermost layer of the band and searching for hits in the remaining layers which fit to a circle with the initial hit. If a group of hits are found which provide a good fit to a circle, then they are recorded as a possible track segment. This is repeated for each band. The curvature and ϕ angle (at the interaction point) of all the track segments are compared. Groups of track segments with similar curvature and angle are then defined as a track.

The electromagnetic shower counter

The electromagnetic shower counter (SHW) measures the energy of electrons and photons. Since nearly half of the energy of a quark jet is carried by π^0's (which decay to two photons), the SHW is useful in determining the thrust direction.

The SHW occupies the cylinder from $r = 79cm$ to $r = 110cm$ with a length of $220cm$. This corresponds to an angular coverage of $|\cos\theta| \leq 0.73$. It consists of 20 layers each containing a lead panel and a gas proportional tube. The lead is $3.5mm$ thick in the first 16 layers and $7mm$ thick in the last 4. The proportional tubes are $10.7mm$ thick. Both θ and ϕ information is obtained from the tubes. This is done by placing rectangular pickup pads just outside the tubes with the longer dimension running in the θ direction on one side of the tube and in the ϕ direction on the other side. The pickup pads are ganged together in groups of 4 layers to

form *towers* which point back to the interaction point. The fine segmentation of the pickup pads provides very good spatial resolution; about 5 milliradians. The energy resolution is not as impressive. The design resolution was $\frac{\Delta E}{E} \approx \frac{15\%}{\sqrt{E}}$ with E in GeV. However, due to an accident, a number of wires could not hold high voltage so the resolution was degraded to about 30%.

In this thesis, the SHW information is only used for determining the thrust direction. It is useful because in a quark jet there are many photons resulting from the decay of π^0's. The SHW information is not needed, however, in determining the jet charge. To check for problems introduced by errors in measuring π^0 energy, the measurement is repeated using only charged particles (i.e., without the SHW information) for comparison.

The magnet

AMY is an unusually small detector. This is allowed by the high field produced by its super-conducting magnet. The magnet is made from an eight layer coil of super-conducting NbTi which occupies the cylinder from $r = 119cm$ to $r = 129cm$, and $|z| < 77cm$. It is held in a liquid helium cryostat and surrounded by 650 tons of iron which acts as a flux return. The magnet is excited with 5000 amperes of current to provide a central field of 3.0 tesla and a stored energy of $40MJ$. The field is uniform to within 10% over most of the CDC's volume. This uniformity simplifies the tracking software since the track segments in each band can be treated as arcs of a circle.

The muon chambers

Photons and electrons are stopped in the SHW. Pions, kaons, and other hadrons easily penetrate the SHW, but they are absorbed in the iron flux return yoke. Muons penetrate the SHW and the iron yoke. They are then detected in the muon chambers (MUO) which consist of 4 layers of drift tubes which cover the same solid angle as the SHW. Two of the layers are oriented along the beam

direction, and the other two are perpendicular to it. Outside the drift tubes there are scintillating plastic sheets which cover the same solid angle. These are used to measure the time of flight of the muons in order to reject triggers from cosmic ray muons. The information from the muon chambers is not needed in this thesis.

The end region detectors

In early running, the luminosity monitor (LUM) was used to measure the luminosity by detecting bhabha scattering very close to the beam pipe. In that angular region, the rate for bhabha scattering is high so the luminosity can be accurately measured. The LUM was made from 4 BaF_2 crystals with no extra segmentation. The pole tip calorimeter also provided a measure of the luminosity. In addition, it provided energy and position information comparable to the SHW. It was made from layers of lead and plastic scintillator along with a single proportional tube layer. The ring veto counter (RVC) was made from 2 layers of lead and plastic scintillator. Its purpose was simply to detect the presence of any particles moving through the end regions. This was needed for missing energy determination which is required in some exotic particle searches.

In 1989, the end regions were completely replaced. The LUM was replaced by the small angle counter (SAC). It also uses BaF_2 crystals, but provides better angular coverage and rather good energy resolution. The PTC and RVC were replaced by the end cap shower counter (ESC). Like its predecessors, the ESC is made from layers of lead and plastic scintillator. It also has proportional tubes with pad readout similar to the SHW to provide position information. A new addition to the end regions was the forward tracking chamber (FTC). This is a drift chamber designed to take over the job of the CDC for particles with $|\cos\theta| \geq 0.82$, and extend the coverage out to $|\cos\theta| \leq 0.97$. This is of particular importance to any asymmetry measurements, such as this thesis, since the cross-sections are peaked at large $|\cos\theta|$ (see figure 3.1). The good $r-\phi$ and z resolution of the VTX combined with the tracking of the FTC was intended to provide good direction and momentum resolution in this crucial region of $\cos\theta$. Unfortunately, however,

difficulties were encountered in the installation and operation of the FTC, so that it has not yet provided useful data. Therefore, this thesis does not use information from any of the detectors in the end region, either before or after the upgrade of 1989.

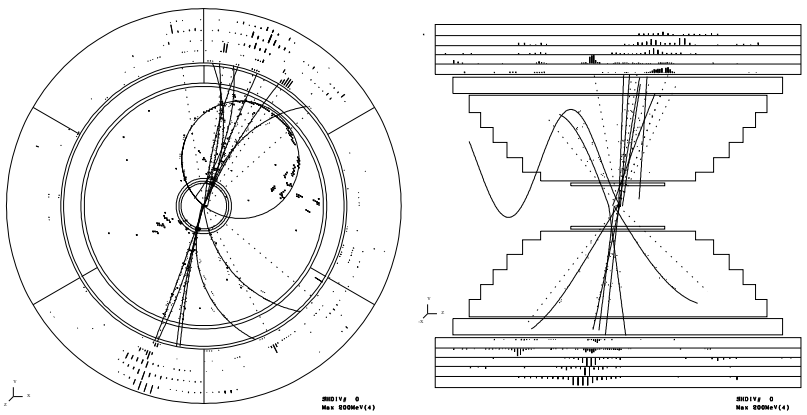

Fig. 4.6: Display of a 2 jet event in AMY. Only the ITC, CDC, and SHW are shown. On the left is the event as seen from the positive z-axis (looking down the beam direction). On the right is the event as seen from the negative x-axis (looking perpendicular to the beam direction). The scattered dots indicate hardware hits. The solid curves are the software reconstructed tracks of charged particles. The dotted lines are the reconstructed tracks of photons (as determined from energy deposited in the shower counter).

For illustrative purposes, figure 4.6 shows a sample 2 jet event in AMY. Two views are shown; a "beam's eye view", and a side view. There are several things worth noting.

1. The two jets are very distinct and easily separable, and they contain stiff (high momentum) tracks.

2. The electric charge of each track is readily apparent from the direction of the track's curvature in the left hand figure, even by eye. (If some of the tracks look straight, hold a straight-edge next to them to see the curvature.) This large curvature is a feature of the high magnetic field.

3. There is one track which has low enough momentum that it repeatedly curls within the CDC until it finally escapes out the end of the detector. This is an example of the curlers mentioned above.

4. There is a track which does not point back to the primary vertex. That track is not likely to come from the primary interaction. It could be the result of a tracking error. It could also have resulted from an interaction between a beam particle and a gas molecule in the beam pipe, or it could be a particle that back scattered off of some material in the SHW or even the opposite side of the beam pipe. In any case, that track would not be used in determining the thrust axis or jet charge.

5. There is scattered noise in both the CDC and SHW which the track reconstruction software successfully ignores.

This chapter has described the technical aspects of the collider and detector. The next chapter describes the effects that the detector has upon the thrust and charge techniques.

5. Detector effects

In chapter 3, fragmentation effects were discussed, and methods were developed to extract the necessary information from the final state particles. In the same way, this chapter deals with the effects of the imperfect detector.

5.1 Simulation

The Monte Carlo program provides information about the four momentum, charge, particle species, etc. of the final state particles in sample events. A simulation program is then used to simulate the detection of these particles. This program uses information about the detector to simulate the output of each part of the detector. This simulated output can then be processed in exactly the same manner as the real data from the detector.

The simulator's output has been found to agree well with what is actually observed in the detector.[31] For example, figure 5.1 compares the distributions of $\cos\theta$ and ϕ of the thrust axis for simulated and real data. The agreement between simulated and real data indicates that the simulator accurately models the geometrical acceptance of the detector and its effect upon the thrust direction. So, simulated data can be used for tests of the thrust method.

Another comparison of simulated and real data is in figure 5.2. It shows the missing momentum distribution and the visible energy distribution. The simulated data is slightly optimistic, but otherwise it matches the real data rather well. Notice that the visible energy is peaked below $E_{vis}/E_b = 2$. This can be attributed to lost K^0's since the SHW is an electromagnetic calorimeter and only measures the energy of electrons and photons.

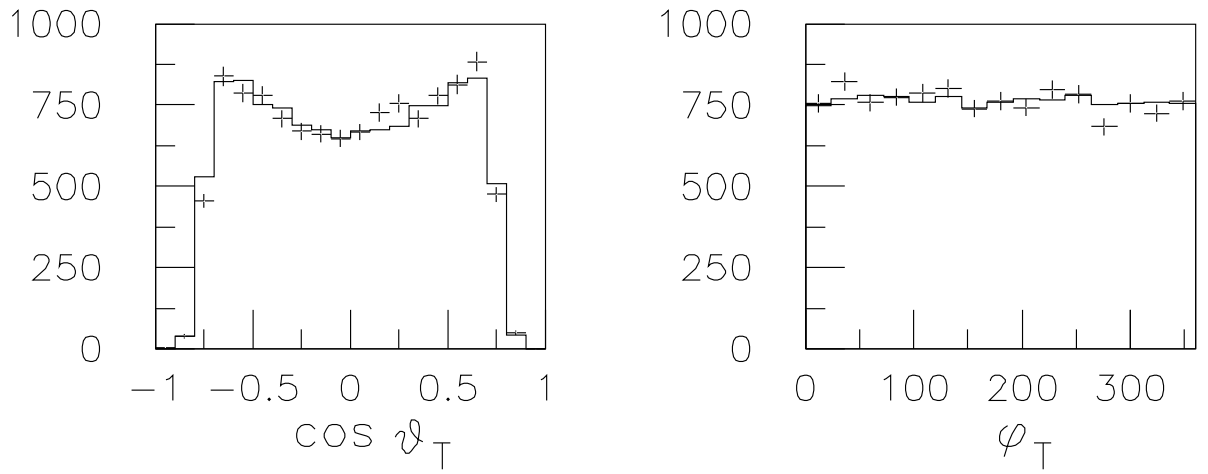

Fig. 5.1: Comparison of the distributions of $\cos\theta$ and ϕ of the thrust axis for simulated (histogram) and real data (points). The simulated data sample contains 3.5 times as many events as the real data sample, so the histogram is scaled down accordingly. Notice that the cylindrical structure of the detector is apparent in the way that the $\cos\theta$ distribution falls off at the edge of the detector, but is uniform for all values of ϕ.

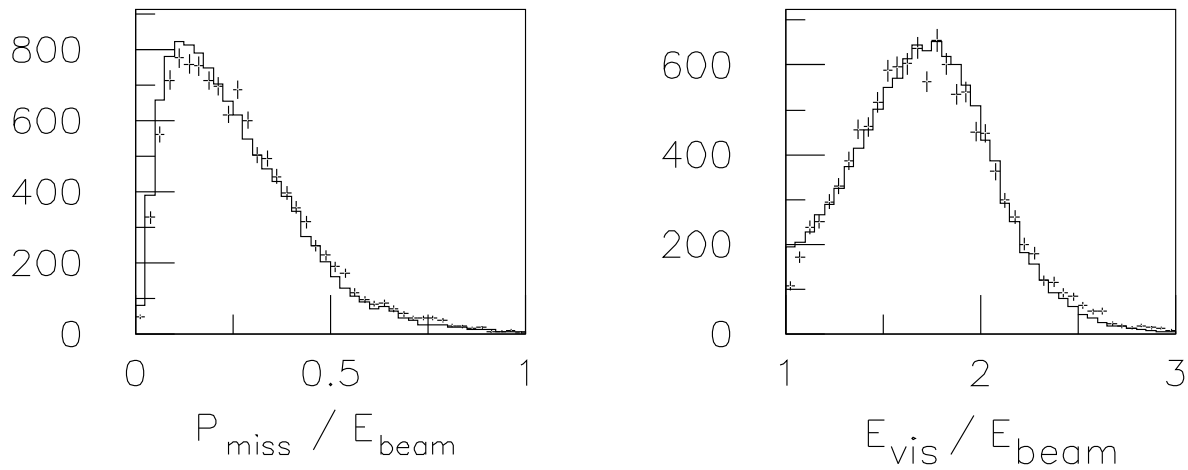

Fig. 5.2: Comparison of the distributions of missing momentum and visible energy (both scaled by the beam energy) for simulated and real data.

Finally, figure 5.3 compares the jet charge measurement in simulated and real data. This is done by plotting the distribution of the jet charge difference i.e.,

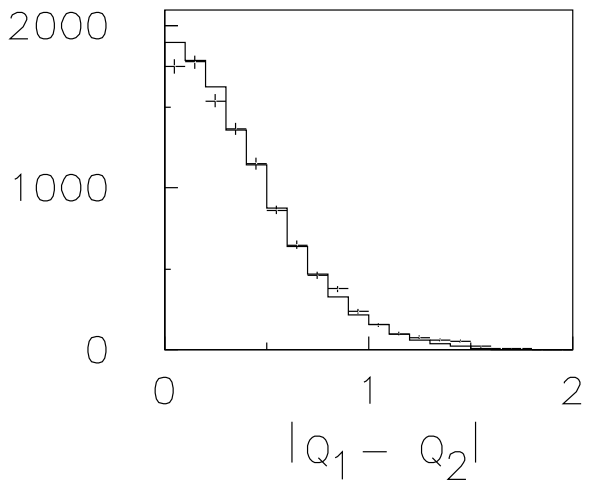

Fig. 5.3: Comparison of the distribution of jet charge difference for simulated and real data.

$|Q_1 - Q_2|$. The good agreement between simulated and real data indicates that the simulated data properly accounts for any effects the detector has on the jet charge method.

In general, the simulator does a good job of modelling the detector response. However, it is a little optimistic in the sense that it tends to slightly underestimate the missing momentum and energy, and it gives slightly narrower thrust distributions than are found in the real data. This arises because the simulator cannot take into account effects such as sporadic electronic noise, unknown errors in alignment, temporarily deactivated channels, calibration errors, etc. To allow for such effects, it is essential that the final measurement be tested for self consistency within the real data. But, with that in mind, simulated data is used throughout the remainder of this chapter to study the detector's response to the thrust and jet charge methods developed earlier, and to finalize the cuts used to select the data sample.

5.2 Initial State Radiation

In section 3.2, the effects of initial state or final state photon radiation where introduced and it was stated that radiative events must be removed from the data

sample. This task turns out to be rather easy for events which radiate a high energy photon since AMY does not efficiently trigger on such events. They send most of their energy down the beam pipe where it is not detected, resulting in insufficient energy inside the detector for triggering. However, events which radiate lower energy photons are difficult to identify.

Since the direction of the radiated photon is unrelated to the quarks' directions, it is likely to be isolated from the quark jets. So, the most direct way of distinguishing radiative events is to look for *isolated photons* detected by the shower counter. This is done by cutting an event if the jet clustering algorithm finds a jet which has more than 90% of its energy carried by a single neutral particle, but only if that neutral particle has more than $8GeV$ of energy. This technique was chosen instead of a "cone isolation" requirement because it is simpler and less sensitive to noise in the shower counter. The cone isolation requirements are more appropriate for cases where one wants to be assured that the selected event is in fact a radiative event. Rather, we want to have a high probability of cutting radiative events even if we must cut some non-radiative events as well. This technique effectively removes events with medium energy photons, but low energy photons are difficult to distinguish from electronic noise.

The isolated photon cut in combination with the standard selection cuts removes most of the events with medium or high energy initial state radiation, but it has little effect on events with low energy initial state radiation. In fact, there is no way to efficiently remove low energy radiative events. As discussed in section 3.2, initial state radiation of any energy has some effect on the asymmetry. So the low energy events may still have an effect. The number of surviving radiative events is not large (35% of the data sample compared with 45% before cuts), so the effect will not be large, but it will need to be considered later as a systematic uncertainty.

5.3 Thrust

The dominant detector effect comes from geometrical acceptance. Recall that the CDC and SHW only cover the angular regions $|\cos\theta| < 0.8$ and $|\cos\theta| < 0.73$, respectively. So, any charged particles with $|\cos\theta| > 0.8$ are not detected, and any photons with $|\cos\theta| > 0.73$ are not detected.[32] As a result, the acceptance falls off and the angular distribution is perturbed at large $|\cos\theta|$. Figure 5.6 shows this by plotting $\cos\theta$ of the thrust direction for a large sample of simulated events and comparing it to a $1 + \cos^2\theta$ curve. Notice that the data fits the curve well for low values of $|\cos\theta|$, but falls rapidly for $|\cos\theta| \geq 0.7$.

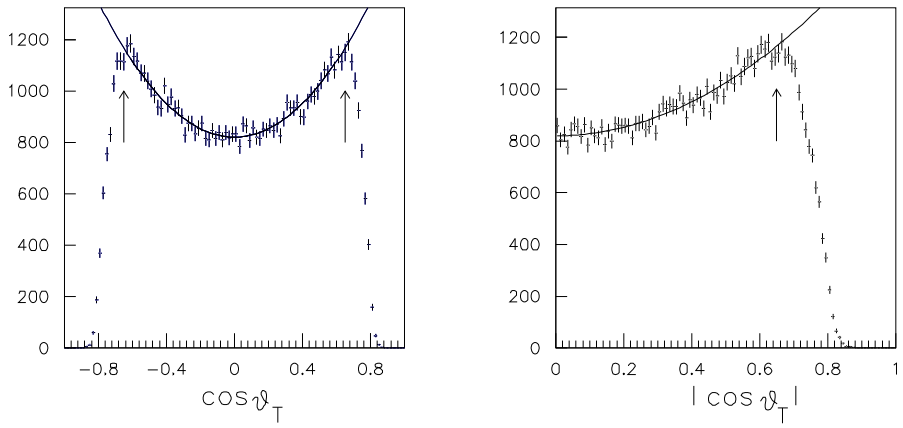

Fig. 5.6: (a) Distribution of $\cos\theta$ of the thrust axis. (b) Distribution of $|\cos\theta|$ of the thrust axis. The data points are from a large sample of simulated data. The solid curve is a $1 + \cos^2\theta$ fit to the data points with $|\cos\theta| < 0.6$. The chosen cut, $|\cos\theta| < 0.65$, is shown with arrows.

In order to assure an unperturbed angular distribution for the asymmetry measurement, the thrust axis must be *well* within the confines of the central detector. So, a $|\cos\theta_T| > 0.65$ cut is used. This cut is shown by arrows in figure 5.6. A slightly larger value might be acceptable, but it is desirable to use a conservative cut to reduce systematic uncertainties.

In figure 3.8 of section 3.3.1, the performance of the thrust method was examined using Monte Carlo data. In the same way, figure 5.5 shows the thrust method's

performance using simulated data by plotting the angle between the thrust axis and the original quark direction for events which pass the $|\cos\theta|$ acceptance cut. The figure shows that for events with thrust less than 0.8, the thrust axis does not reliably match the quark direction. For that reason, events with $T < 0.8$ are cut. However, for events with thrust greater than 0.8, the match is within 10 degrees for over 85% of the events. This indicates that the detector does not significantly affect the determination of the thrust direction for events which are well within the detector acceptance.

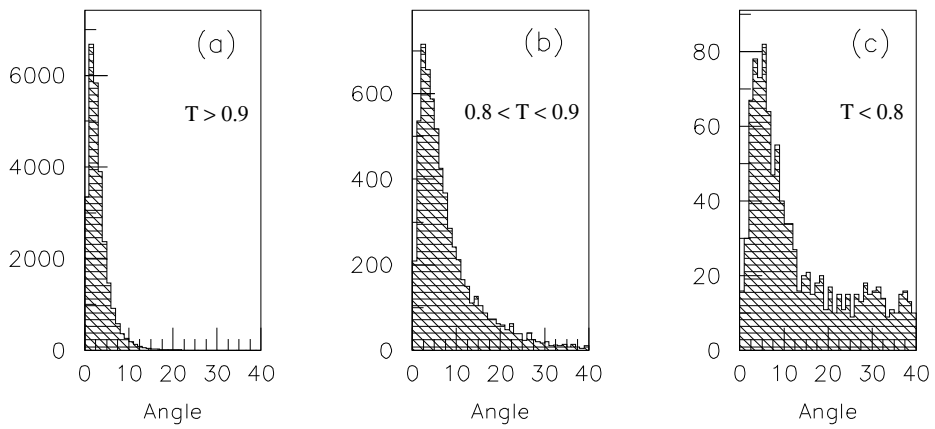

Fig. 5.5: Distribution of the angle between the quark direction and the thrust direction in degrees for events with various thrust values. The thrust axis was calculated with *simulated* data. Comparing this figure to figure 3.8 shows that detector effects do not seriously degrade the performance of the thrust method.

To improve the reliability of the thrust direction, an additional cut is applied. It requires that the z component of the missing momentum be less than 40% of the beam energy. This cut removes events for which the quark-antiquark pair are out of the detector's acceptance but which happen to send some of their energy into the detector (e.g. through gluon radiation). It is also helpful in removing events with very high energy initial state or final state radiation.

5.5 Jet charge

The determination of jet charge is also affected by measurement errors in the detector. Recall that the jet charge is determined from a weighted sum of the particles' charges,

$$Q_{jet} \equiv \frac{\sum_{i=1}^{N} q_i |\vec{p}_i|^{\kappa}}{\sum_{i=1}^{N} |\vec{p}_i|^{\kappa}}. \tag{3.3}$$

So, an error in measuring the momentum of a charged particle will affect that particle's contribution to the jet charge sum. In addition, it is possible that not all the particles are detected either due to track finding inefficiencies or detector acceptance. These measurement errors cause the percentage of events with correctly identified jet charge, P, to be a few percent lower than what was found in chapter 3 where a perfect detector was assumed. The general features, however, remain the same. This is shown in figure 5.7 which plots P as a function of the weighting exponent, κ. The choice for κ remains at 0.5 since it continues to provide the highest values of P.[33]

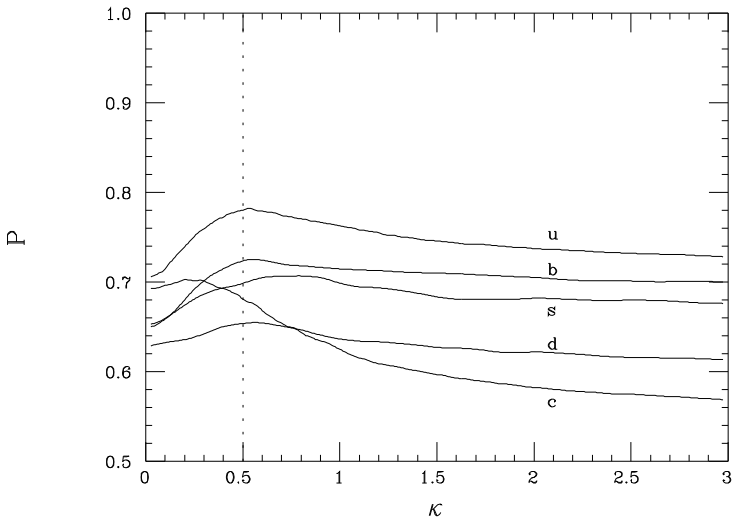

Fig. 5.7: Plot of the percentage of events with correctly identified jet charge, P, as a function of the momentum weighting exponent, κ, for each flavor. This figure is similar to figure 3.16 except that here P is calculated using simulated data.

Flavor	u	d	s	c	b
P_q	$78.5 \pm 0.4\%$	$65.7 \pm 0.8\%$	$70.3 \pm 0.8\%$	$68.1 \pm 0.5\%$	$71.5 \pm 0.8\%$

Table 5.1: Performance of the momentum weighted jet charge method, for each flavor, using $\kappa = 0.5$

From the simulated data, the P values were measured for each flavor. The results are listed in Table 5.1. The errors shown are statistical only (limited by the size of the simulated data sample). The systematic uncertainties will be considered later.

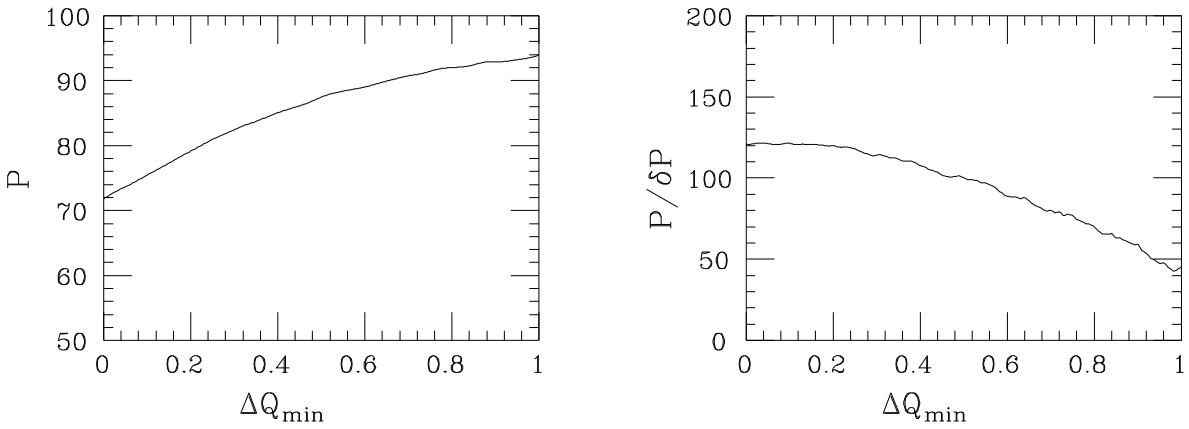

Fig. 5.8: (a) Plot of the percentage of events with correctly identified jet charge, P, as a function of the charge difference cut, ΔQ_{min}, for all flavors combined. (b) Plot of the *significance* of P as a function of ΔQ_{min}. For ΔQ_{min} greater than about 0.15 too many events are cut so the significance decreases.

Recall from section 3.3.2 that P can be improved by removing events which have nearly equal charges for the two jets. This is implemented by requiring that the magnitude of the difference between the charges of the two jets be greater than some value ΔQ_{min}. To decide on a ΔQ_{min} value, figure 5.8(a) plots P as a function of ΔQ_{min} for all the quark flavors combined. P increases as ΔQ_{min}

is increased. However, choosing a ΔQ_{min} which is too large will cut too many events and must be avoided. To find the optimum value, figure 5.8(b) plots $\frac{P}{\delta P}$ as a function of ΔQ_{min}. For ΔQ_{min} greater than ≈ 0.15, $\frac{P}{\delta P}$ decreases since larger values of ΔQ_{min} cut too many events and therefore increase the errors. So, a charge difference requirement of $\Delta Q_{min} = 0.15$ is used. Table 5.2 shows the improvement in the epsilon values after the charge cut is applied.

Flavor	u	d	s	c	b
P_q	$84.2 \pm 0.4\%$	$71.1 \pm 0.9\%$	$75.4 \pm 0.8\%$	$73.5 \pm 0.5\%$	$76.8 \pm 0.8\%$

Table 5.2: Performance of the momentum weighted jet charge method, for each flavor, using $\kappa = 0.5$ and $\Delta Q_{min} = 0.15$.

Some points which must be addressed regarding P are to check for energy dependence and angular dependence. AMY has run at various center of mass energies ranging from 50 to 64 GeV. This is not a wide range of energies, but it is important to verify that P does not change with energy. Figure 5.9 plots the P values, determined from simulated data, as functions of the center of mass energy for each flavor. There is no significant energy dependence so it is valid to use the P's listed in Table 5.2 for all energies. In a similar way, plotting P versus $|\cos\theta|$ (not shown) indicates that there is no angular dependence.

Recall from Eq. 3.4 in section 3.3.2 that the asymmetry is reduced by a factor of $2P - 1$. As a consistency check, figure 5.10 compares the asymmetry values measured using simulated data to the expected values including the $2P - 1$ factor. The agreement indicates that the charge determination does have the expected effect.

Since d-type quarks have $\frac{1}{2}$ the charge of u-type quarks, a large charge cut is more likely to cut d-type quarks than u-type quarks. This changes the flavor spectrum of the data sample, and must be taken into account since it alters the

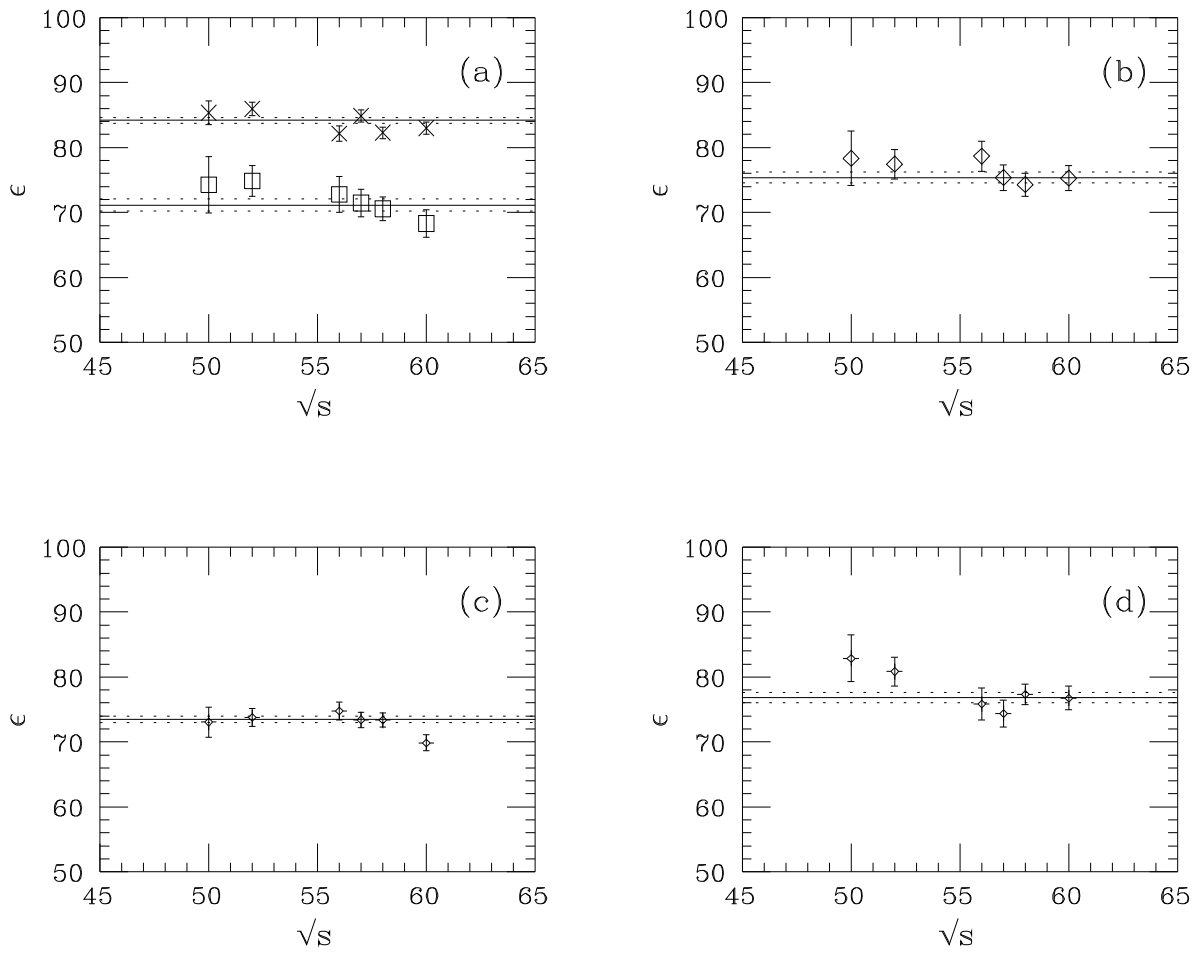

Fig. 5.9: Plot of the percentage of events with correctly identified jet charge, P, as a function of the center of mass energy, $\sqrt{s}$, for each flavor. (a) shows P_u and P_d. (b) shows P_s. (c) shows P_c, and (d) shows P_b. The solid lines are the average over all energies with the combined uncertainty shown by the dotted lines.

contribution that each flavor makes to the asymmetry sum. The easiest way to account for this is in terms of a selection efficiency for each flavor. These selection efficiencies are denoted by f_q, and are listed in Table 5.3. Notice that f_c is significantly lower than f_u. This comes from the fact that P_c is lower than P_u so that the charge cut removes more c events than u events. The same effect pulls f_d below f_s and f_b. In addition, however, c events are also a little more likely to be cut by the standard selection cuts or the initial state radiation cuts. This is

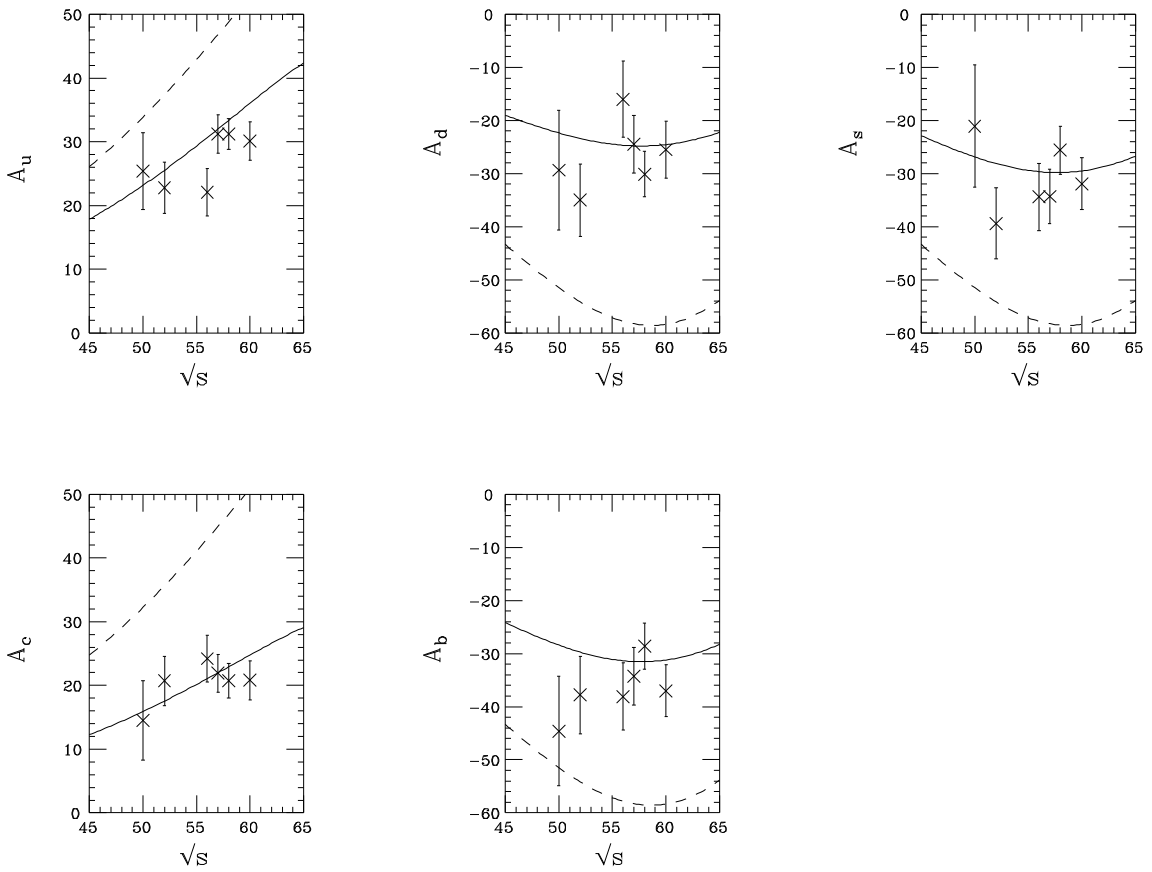

Fig. 5.10: Plot of the measured asymmetry (in simulated data) as a function of energy for each flavor. The solid lines show the predicted asymmetry including the $2P-1$ reduction factor. The dashed lines show the predicted asymmetry without including the reduction factor.

taken into account in the f_c shown in Table 5.3. This introduces the possibility of a systematic error which is why f_c has larger uncertainty than f_u. Although the plots are not shown, the f_q's have been checked for energy and angular dependence. No significant dependence was seen.

Flavor	u	d	s	c	b
f_q	$76.01 \pm 0.36\%$	$71.39 \pm 0.68\%$	$73.38 \pm 0.66\%$	$70.42 \pm 0.90\%$	$71.94 \pm 0.65\%$

Table 5.3: This table lists the percentage of each flavor's data sample which passes the charge difference cut.

The way in which the expected value of the hadron asymmetry depends on the f_q's and P_q's is derived below. The total differential cross section is just the sum of the cross sections for the individual flavors.

$$\frac{d\sigma_h}{d\Omega} = \sum_{q=d,u,s,c,b} \frac{d\sigma_q}{d\Omega} \tag{5.1}$$

$$= \frac{\alpha^2}{4s} \sum_{q=d,u,s,c,b} R_q(1+x^2) + B_q x \tag{5.2}$$

where $x \equiv \cos\theta$. The different selection efficiencies of each flavor merely scale the contribution of each flavor's cross section. Also, as was shown in section 3.3.2, the misidentification of jet charge replaces B_q with $(2P_q - 1)B_q$ so that

$$\frac{d\sigma_h}{d\Omega} = \frac{\alpha^2}{4s} \sum_{q=d,u,s,c,b} f_q[R_q(1+x^2) + (2P_q - 1)B_q x] \tag{5.3}$$

Defining R_h and B_h as

$$R_h \equiv \sum_{q=d,u,s,c,b} f_q R_q \tag{5.4}$$

$$B_h \equiv \sum_{q=d,u,s,c,b} f_q(2P_q - 1)B_q,$$

this reduces to

$$\frac{d\sigma_h}{d\Omega} = \frac{\alpha^2}{4s}[R_h(1+x^2) + B_h x]. \tag{5.5}$$

Comparing this to Eq. (2.10), the hadronic charge asymmetry is identified as

$$A_h = \frac{3B_h}{8R_h}$$

$$= \frac{3}{8} \frac{\sum_{q=d,u,s,c,b} f_q(2P_q - 1)B_q}{\sum_{q'=d,u,s,c,b} f_{q'} R_{q'}} \tag{5.6}$$

$$= \frac{\sum_{q=d,u,s,c,b} f_q(2P_q - 1)R_q A_q}{\sum_{q'=d,u,s,c,b} f_{q'} R_{q'}} \tag{5.7}$$

where the last step was to multiply by R_q/R_q in each term of the sum. This expresses the hadronic charge asymmetry as a weighted sum of the asymmetries of the individual flavors. Each flavor's weighting depends on how well its charge direction can be determined (accounted for by the $2P - 1$ factor) and on the fraction of the total data sample that the flavor comprises (accounted for by the $f_q R_q / \sum f_{q'} R_{q'}$ factor).

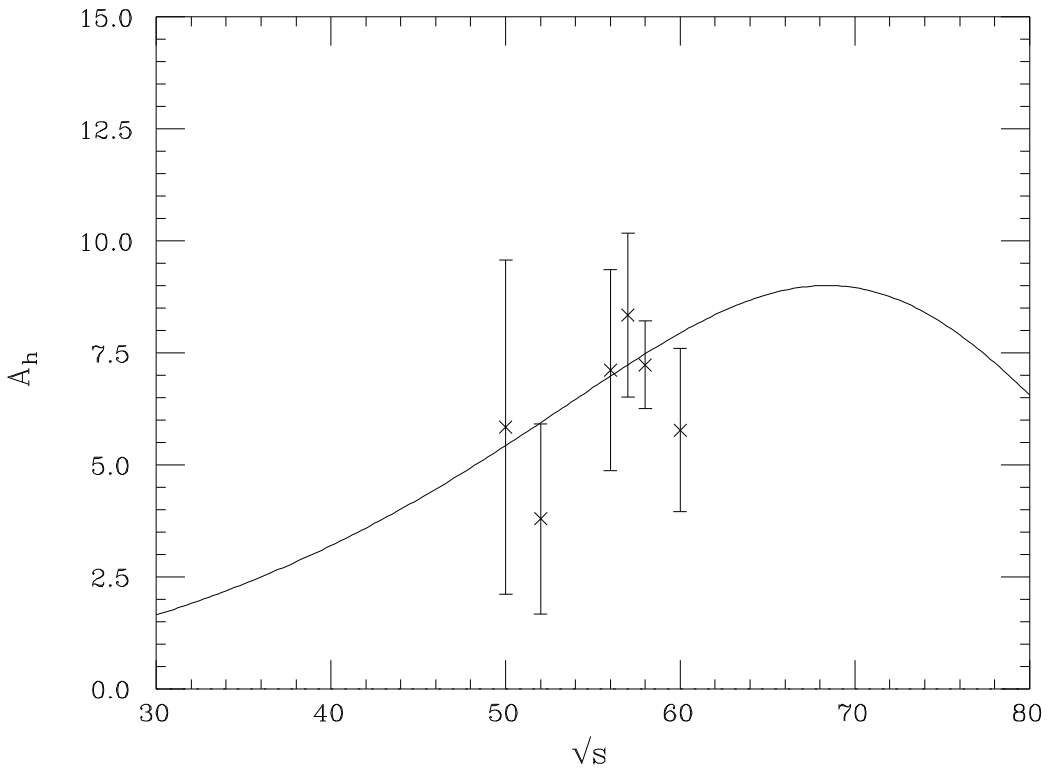

Fig. 5.11: Plot of the measured asymmetry (in simulated data) for several energies. The solid line compares the predicted asymmetry from Eq. (5.6).

This prediction for the asymmetry is plotted as a function of center of mass energy in figure 5.11. Notice that it peaks around $68GeV$ but does not depend as strongly on energy as the asymmetries of the individual flavors. To assure that the Monte Carlo program and the detector simulator give self-consistent results, data points are plotted on figure 5.11 showing the asymmetry values measured using simulated data samples at various energies. The agreement indicates that the f and P values are self-consistent.

This chapter has dealt with the effects of an imperfect detector. The primary effects are (1) a minor increase in the average angle between the quark direction and the thrust direction; (2) a small decrease in the percentage of events with correctly identified jet charge; and (3) no acceptance at small angles. These effects can be accounted for in calculating the expected hadron asymmetry and the results are found to be self-consistent within the simulated data. The next chapter will discuss the actual measurement.

6. Results

Chapter 2 described the experimental techniques used for determining the hadronic charge asymmetry, and chapter 5 finalized them after accounting for detector effects. This chapter describes the results of the measurement. Throughout the chapter, only statistical uncertainties are given. The systematic uncertainties are examined in the next chapter.

The primary result is the angular distribution of the positively charged jet direction with respect to the direction of the incident positron. This is plotted in figure 6.1 for all the experimental data combined. The solid curve is a best fit to the data points (as described in section 3.1). Notice that the data fits rather well, and that is does not fit the symmetric curve (dotted) at all; that has a $\chi^2 > 28$ with 8 degrees of freedom!

AMY accumulated data at many different energies. A plot similar to figure 6.1 was made at each energy to measure the asymmetry. The results are tabulated in table 6.1, and plotted in figure 6.2 as a function of the center of mass energy. Notice that many of the energies have very low integrated luminosity. TRISTAN ran at these energies only as part of an energy scan. The asymmetry for each of these low statistics runs is virtually meaningless alone, so the table and figure do not show measurements for runs with $\int \mathcal{L} < 0.5 pb^{-1}$. However, that data will be incorporated later in measurements which combine several energies.

The asymmetry values fit well to the predicted asymmetry curve and clearly indicate that the asymmetry is positive. As a test of the goodness of the fit, $\chi^2 = 15$ relative to the predicted curve (with 14 data points), and $\chi^2 > 40$ for the

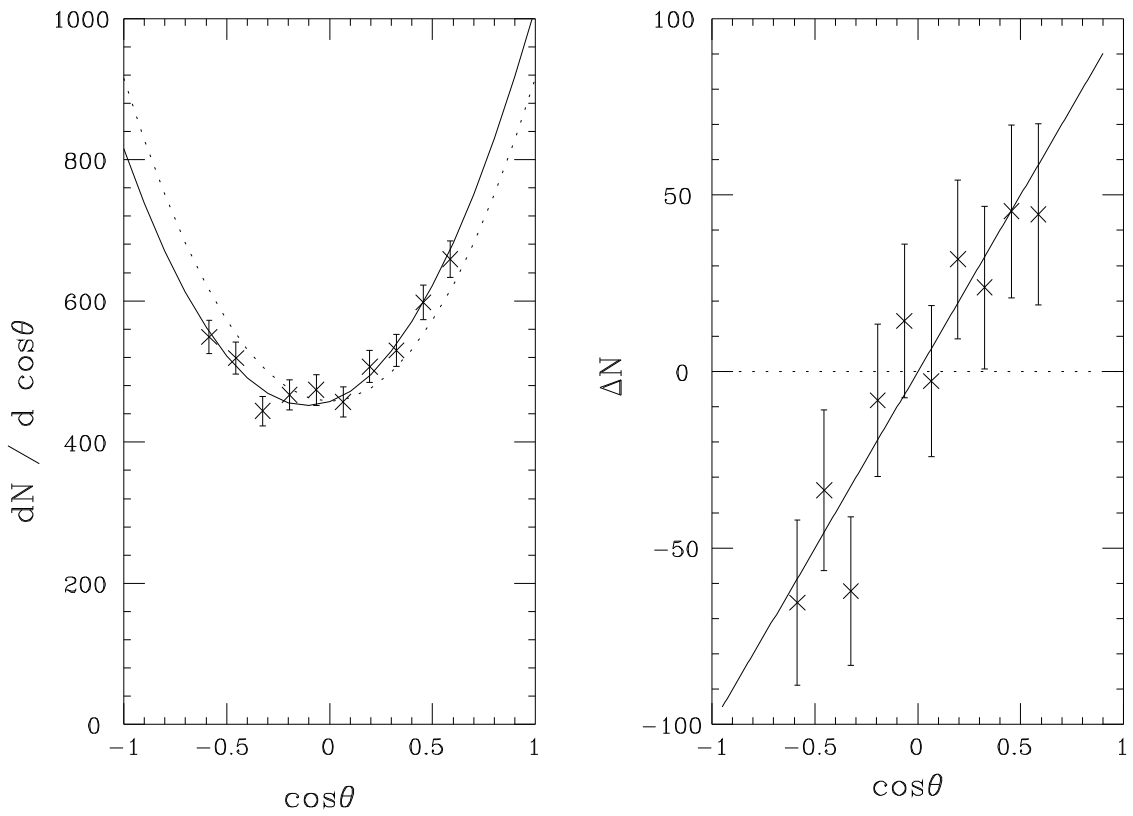

Fig. 6.1: The left hand figure is a plot of the angular distribution of the positively charged thrust axis measured with AMY's total hadron data sample of $96pb^{-1}$. The solid curve is the best fit to the data points (as described in section 3.1). The fitted asymmetry value is $8.2 \pm 1.7\%$. The χ^2 of the fit is 4.2 for 8 degrees of freedom. The dotted curve is what would be expected if the asymmetry were zero. The right hand figure plots the difference between the data points and the symmetric distribution, and clearly shows the asymmetry in the angular distribution.

$A(\sqrt{s}) = 0$ curve.

Figure 6.2 is rather busy with all of the different data points. A cleaner presentation of the data can be made by combining the data into 3 energy bins; $\sqrt{s} < 58GeV$, $\sqrt{s} = 58GeV$, and $\sqrt{s} > 58GeV$. The integrated luminosities of these three data sets are approximately 20, 61, and $15pb^{-1}$ respectively. The average energies of each data set, weighted by luminosity, are 55.1, 58.0, and $60.8GeV$. The asymmetry values are $4.5 \pm 3.4\%$, $9.6 \pm 2.1\%$, and $8.0 \pm 4.1\%$, and they are plotted in figure 6.3. This figure more clearly shows the agreement between AMY's data and the prediction.

$\sqrt{s}$ (GeV)	$\int \mathcal{L}dt$ (pb^{-1})	A_h (%)	χ^2 (8 d.o.f)
50	0.636	-7.0 ± 18	6.6
52	3.976	-6.4 ± 7.6	6.9
54	0.531	17 ± 23	6.5
55	3.266	-0.4 ± 9.1	14.0
56	5.993	14 ± 6.2	13.7
56.5	0.994	-28 ± 16	6.7
57	4.398	17 ± 8	6.3
57.25	0.058		
57.5	0.080		
57.75	0.078		
58	60.903	9.6 ± 2.1	3.5
58.5	0.801	-20 ± 18	13.5
58.75	0.087		
59	0.722	33 ± 21	6.6
59.05	0.504	3.0 ± 26	8.7
59.25	0.098		
59.5	0.072		
60	3.551	6.4 ± 8.6	12.2
60.8	3.481	11 ± 9.2	4.2
61.4	4.287	8.7 ± 8.0	4.5
63.6	0.440		
64	1.097	-6.0 ± 16	1.9

Table 6.1: Luminosity and measured asymmetry for each energy. The total luminosity is $\int \mathcal{L}dt = 96.05 pb^{-1}$, and the average energy (luminosity weighted) is $< \sqrt{s} >= 57.8 GeV$.

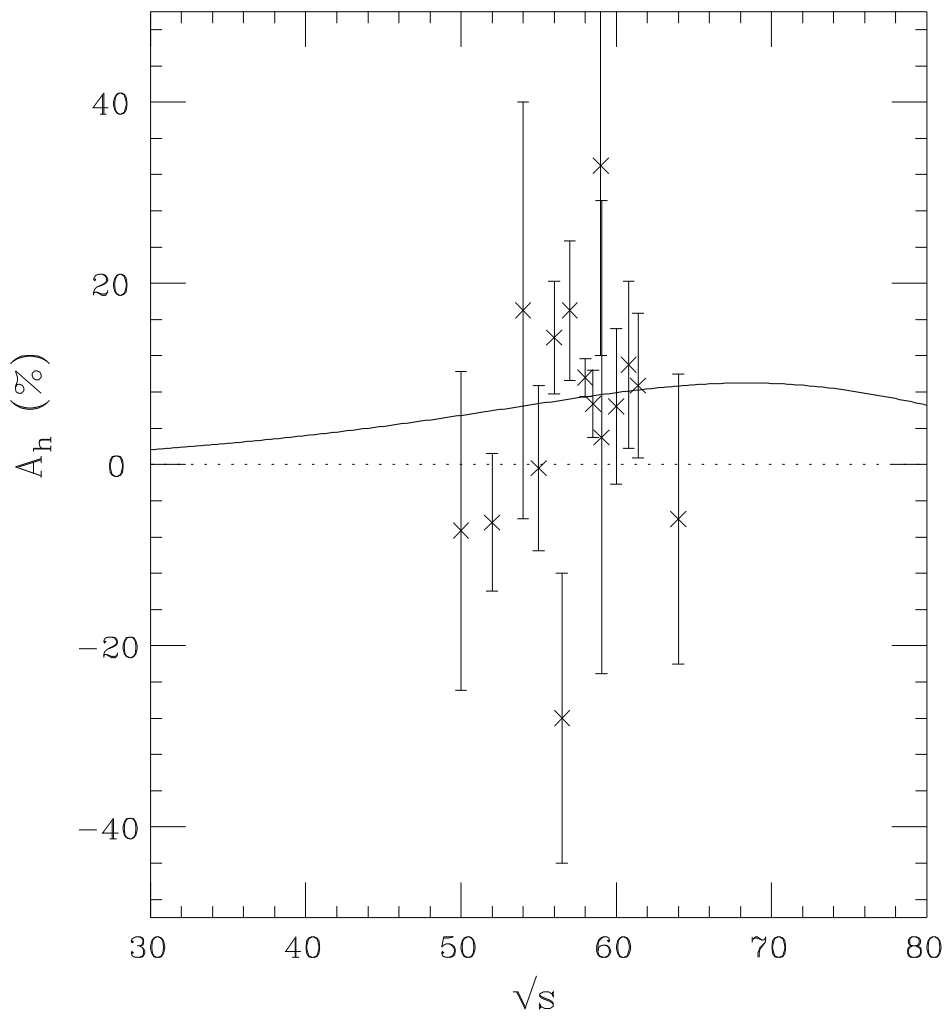

Fig. 6.2: Plot of the measured asymmetry as a function of energy. The solid curve is the predicted asymmetry calculated from Eq. 6.8.

This chapter has shown the primary results of the asymmetry measurement. The measured asymmetry is consistent with the predictions of the Standard Model and the phenomenological models used to describe the hadronization process. The next chapter will discuss the systematic uncertainties in the measurement and describe some self-consistency checks to make sure the results are trustworthy.

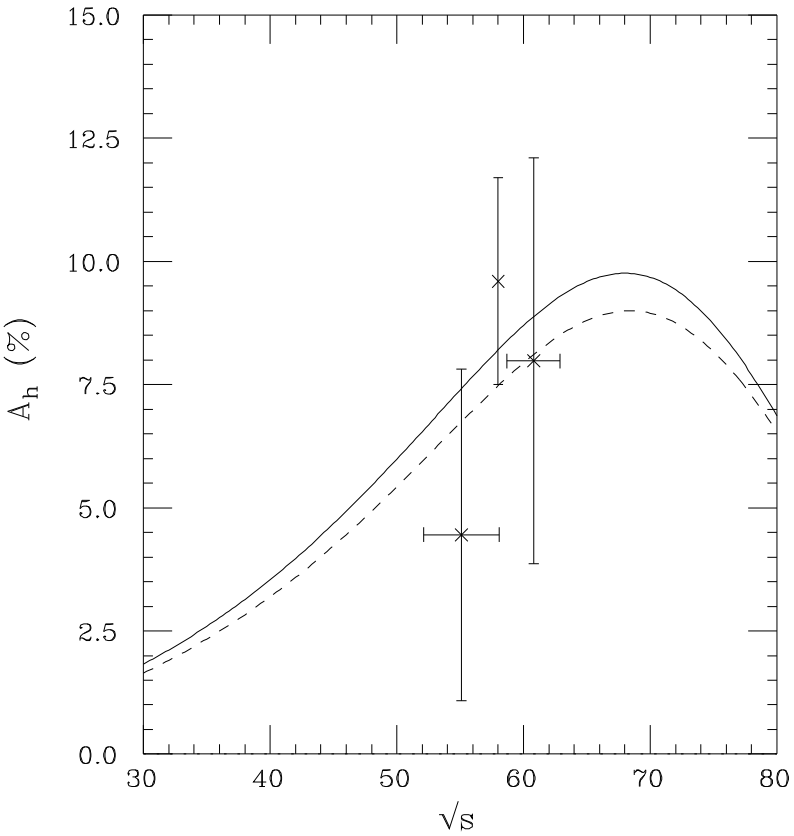

Fig. 6.3: Plot of the measured asymmetry as a function of energy combining the data into 3 energy bins. The horizontal "error" bars show the span of energies included in each point. The solid curve shows the Standard Model prediction including effects from $B^0\bar{B}^0$ mixing, and the dashed curve shows the prediction without including those effects. (The next chapter will describe $B^0\bar{B}^0$ mixing in detail.)

7. Systematic uncertainties and consistency checks

In some sense, the only contribution the physicist makes to a measurement is the uncertainty in the measurement. The statistical uncertainty depends on the total luminosity and was given in the previous chapter; this chapter will discuss the sources of systematic uncertainties and estimate their effect. In addition, some self consistency checks will be made to make sure that the systematic uncertainties are well understood.

The sources of systematic uncertainties (henceforth called *systematics*) can be lumped into several groups: radiative corrections, modelling of the hadronization process, detection, and analysis techniques. Radiative corrections introduce either unknown effects or they introduce effects which are known but cannot be completely accounted for. The most obvious example is initial state or final state radiation, which alters the validity of the thrust direction and introduces an asymmetry effect of its own, as previously discussed. The model used to describe hadronization is key to the measurement, so it must be stable and well understood. The detector can also have a large effect upon the measurement, so it must also be stable and well understood. Finally, the analysis techniques used to make the measurement must not only provide an efficient means of extracting the necessary information, but they must also be stable. For example, the leading particle method of calculating the jet charge was determined to be undesirable not only because it is prone to misidentifying the jet charges, but *also* because it is arbitrary to select one out of the many particles in the jet, especially when there are other particles which have momentum that differs from the leading particle's momentum by less than the measurement uncertainty in the momentum of either particle. Each of these

effects will be discussed separately.

7.1 Radiative corrections

As mentioned in chapter 2, radiative corrections modify the total cross-section and the differential cross-section. Because of the interest in accurately measuring the total cross-section at TRISTAN, the effects of radiative corrections have been thoroughly explored by the TRISTAN theory group.[34] Radiative corrections decrease the asymmetries of the individual quark flavors by less than 10%. This effect is dominated by the interference between initial state and final state photon radiation, which is why the "isolated photon" cut was used to remove such events. However, that cut is not very efficient in removing radiative events, so some of the 10% correction remains. The isolated photon cut and the standard selection cuts reduce the number of radiative events from 45% of the data sample to 35%. So, it is reasonable to estimate that the effect of radiative corrections will be changed by a similar amount i.e., 8% for each flavor. When the flavors are combined, this causes the predicted asymmetry to change by 0.6%.

There is a possibility for confusion here. The contributions from the various systematic uncertainties are given in percent, but the asymmetry is measured in percent. Obviously, a convention is needed. So, all systematics are quoted as a percent of the quantity, *except* for the systematic uncertainty on the asymmetry measurement. It is quoted as the change in the asymmetry value. For example, the systematic uncertainty of 0.6% means that the asymmetry value is predicted to be $7.48 \pm 0.6\%$ at $58GeV$.

This is a small effect, but it is worth checking that it is well understood. One way to check this is to remove the isolated photon cut and verify that the measured asymmetry does not change by more than 0.6%. This consistency check is complicated by the fact that some of the isolated photons carry up to $30GeV$ of energy. In such events, it is simply impossible to measure the thrust direction. So, for the purposes of this check, the isolated photon cut is not removed completely,

but rather relaxed from $4GeV$ to $20GeV$. The measured asymmetry decreases (as expected) by 0.2%, indicating that the 0.6% uncertainty is realistic.

A further test is to measure the asymmetry of the events which are cut by the isolated photon cut. These events should exhibit a negative asymmetry. Again, it is not possible to use events with a very high energy photon, so the selected data sample is events with an isolated photon with energy between $4GeV$ and $16GeV$. The statistics are low so it is not reliable to try and fit the resulting angular distribution. Rather, the raw asymmetry is measured (see section 3.1) and then corrected for the detector acceptance. The result is $A_h = -66 \pm 14\%$, and is significantly negative. This has been done more carefully by the AMY collaboration as an independent analysis project, as well as by several other experiments.[9]

Another radiative correction effect comes from QCD. The radiation of hard gluons in the final state is not expected to affect the asymmetry directly, but it is interesting to verify this by looking at events with gluon radiation (i.e, 3 jet events) to see if they have a significantly different asymmetry. As discussed in chapter 3, the jet clustering algorithm groups the particles into jets, and it is capable of distinguishing a third jet coming from a gluon if the gluon has a high enough energy. So, a sample of events with gluon radiation can be obtained by requiring that the jet clustering algorithm find 3 jets. The asymmetry of this data sample can then be compared to the asymmetry of the remainder of the sample (i.e., containing only 2 jets).

Measuring the asymmetry in 3 jet events is complicated slightly by the fact that the angular distribution is perturbed by the gluon radiation so that it is necessary to apply a bin by bin correction to the distribution before calculating the asymmetry. This is shown in figure 7.1 which plots the $|\cos\theta|$ distribution of the thrust axis in 3 jet events. The real data and simulated data are consistent with each other, but they do not match the expectation for a $1+\cos^2\theta$ distribution. This perturbation of the angular distribution is caused by particles lost outside the detector's acceptance which tends to push the thrust axis inward (toward lower

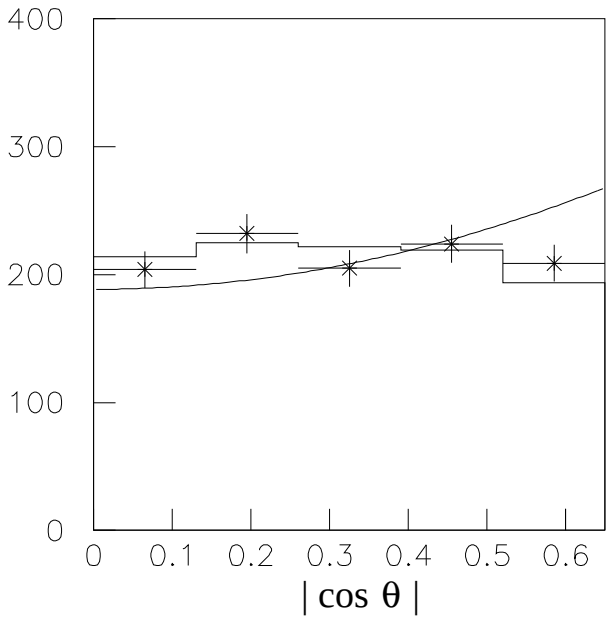

Fig. 7.1: Plot of the distribution of $|\cos\theta|$ for simulated data (histogram) and real data (points) in 3 jet events. The simulated data has been scaled to contain the same number of events as the real data sample. The curve shows the expected $1+\cos^2\theta$ distribution, indicating that the distribution needs to be corrected bin by bin to account for lost particles.

$|\cos\theta|$).

Figure 7.2 shows the angular distribution of both real and simulated data after the bin by bin corrections are applied. No difference can be seen between them, indicating that, as expected, gluon radiation does not affect the asymmetry. It is important to note, however, that gluon radiation does affect the determination of the thrust direction and therefore the angular distribution. This is another source of systematic uncertainty. It can be quantified by the difference between the asymmetry measured with all events and the asymmetry measured with just 2 jet events. This difference is 0.4%. However, the thrust value is closely related to gluon radiation so the uncertainty due to gluon radiation will be taken into account automatically when the systematic uncertainty from the thrust cut is determined later.

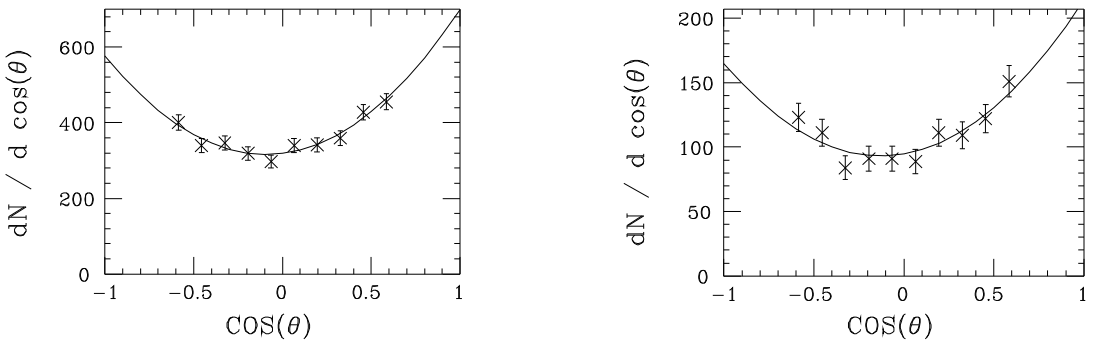

Fig. 7.2: Plot of the corrected angular distribution in 3 jet events. The left plot is for simulated data. The right plot is for real data. The solid lines show the best fit for each case. In simulated data, the asymmetry is $7.2 \pm 2.0\%$. In real data, it is $9.7 \pm 3.6\%$. The vertical scale of the two plots are adjusted to account for the larger sample size in simulated data. This allows direct comparison of the number of 3 jet events in real and simulated data.

7.2 Hadronization uncertainties

The various models used to account for the hadronization process are another source of systematics since they are often only educated guesses which are tuned to fit the observed event properties. The uncertainties of the hadronization model will be described with respect to the three phases of the process: gluon radiation, fragmentation, and decay.

The first phase has already been discussed in the previous section when the effect of gluon radiation was examined. But, a further uncertainty may come from the parton shower prescription for handling very soft gluon radiation. One way to estimate that uncertainty is to "detune" the model and verify that the resulting change in the asymmetry is not large. The parton shower model is tuned by changing the parameters of the first order QCD branchings. This amounts to changing the value of the QCD parameter Λ_{LLA}. In addition, the transverse momentum distribution given to the secondary partons is changed. These changes introduce a change in the asymmetry that is completely negligible.

It should be noted, at this point, that it is not really possible to fully check each tuning difference with a full detector simulation since that would require impossibly

large amounts of computing time and hard disk storage. The simulation of one event requires execution of about 40 billion instructions. Pooling all the computing available for this project, this amounts to $\approx$ 1 minute per event which makes large simulated data samples unrealistic. So, instead, the Monte Carlo program is run to produce generated data samples with the various parameter values, and then the resulting data samples are compared. However, even generating enough data to precisely measure the asymmetry from the angular distribution requires a large amount of computing time, and an unacceptably large amount of hard disk storage (over 2×10^8 bytes per dataset). Because of this, the fitted asymmetries of the generated data samples are not directly compared. Rather, the P and f values are determined from each sample and the expected asymmetry is calculated from them using Eq. (5.7). This is manageable since determining the P and f values to sufficient precision only requires about 20,000 events per sample. Finally, since generated data is used for these tests, the actual value of the asymmetry cannot be compared directly to the real data. As was discussed in chapter 5, the detector imperfections reduce the P and f values and thereby alter the asymmetry in simulated and real data. This is dealt with by determining the fractional change in the asymmetry value for the generated data samples and then scaling that with the predicted asymmetry value in simulated data to obtain the uncertainty in the final measured value.

The second phase, string fragmentation, is treated in the same way. In this case, the parameters of the string fragmentation function are "detuned". Specifically, the parameters a and b in the symmetric LUND fragmentation function, $f(z) = (1-z)^a e^{-bm_T^2/z}$, are changed by approximately 50% from their tuned values. The resulting fractional change in the asymmetry value is 0.015 which corresponds to an uncertainty of about 0.13% in the measured asymmetry.

The uncertainty which is expected to dominant is the uncertainty in the spectrum of particle species which make up the primary mesons. Table 3.1 showed how the type of particles resulting from fragmentation can vary widely depending upon what flavors of $q\bar{q}$ pairs are produced the first few times that the string breaks.

By itself, this does not introduce a systematic error, but the probabilities for producing each flavor when a string breaks are not well know, and that introduces a significant systematic uncertainty. As pointed out in chapter 3, the production of s quarks during the fragmentation process is suppressed due to its larger mass. This suppression has been measured by several experiments,[36] and their combined results are that the ratio of the number of s quarks produced relative to u quarks is $\frac{P(s)}{P(u)} = 0.33 \pm 0.03$. To estimate the effect of the uncertainty in $\frac{P(s)}{P(u)}$, a sample of data was generated with a 1σ deviation i.e., $\frac{P(s)}{P(u)} = 0.36$, and compared to the results using $\frac{P(s)}{P(u)} = 0.33$ (the default). The resulting fractional difference in the asymmetry is 0.06. That corresponds to an uncertainty of 0.5% in the final measured value.

Since this is an important systematic, a small sample of data with $\frac{P(s)}{P(u)} = 0.36$ was simulated so that the comparison could be checked in simulated data as well. The resulting asymmetry difference is $0.3 \pm 1.5\%$. This is consistent with the results from the generated data sample.

The third phase of hadronization, prompt decay, is not as prone to systematics since the vast majority of decays are through well know channels which are completely taken into account by the Monte Carlo program. However, one important effect to consider is $B^0\bar{B}^0$ mixing. It has been shown that B^0 mesons can mix into $\bar{B}^0$ mesons and vice versa.[37] If mixing occurs, then the subsequent decay of the mesons will make the jet charge method likely to incorrectly identify the positively charged jet.

The effect of mixing can be estimated from experimentally determined mixing parameters and the P_b values determined from the Monte Carlo program for B^0 mesons. It will have the effect of reducing the value of P_b, and as a result it will tend to increase the asymmetry.

In estimating the magnitude of the effect, maximal mixing will be assumed for B_s^0 i.e., $\chi_s = 0.5$. The mixing parameter for B_d^0 is taken from the combined ARGUS and CLEO results[37] i.e., $\chi_d = 0.17 \pm 0.04$. If only B_d^0 mesons are considered, the

Monte Carlo program predicts that for generated data, $P_b^d = 70\%$, where the superscript d indicates that only B_d^0 mesons are being considered. So, if a fraction χ_d of these mix to $\bar{B}_d^0$ the result will have $P_b^{d'} = (1-\chi_d)P_b^d + \chi_d(1-P_b^d) = 63\%$. In the same way, the Monte Carlo predicts that $P_b^s = 63\%$, so $P_b^{s'} = (1-\chi_s)P_b^s + \chi_s(1-P_b^s) = 50\%$. Taking into account the $1:1:\frac{1}{3}$ production rates for B_u, B_d^0, and B_s^0, the result is that P_b is decreased by a factor of 0.93. Applying that correction to the P_b from simulated data (after the ΔQ_{min} cut), reduces P_b from 76.8% to 71.7%. This changes the expected asymmetry by +0.8%.

Notice that this is *not* actually a systematic uncertainty since the effect of $B^0\bar{B}^0$ mixing can be determined in a straight forward manner. The source of uncertainty comes from any unknown or uncertain aspects of the method used to account from the effect. The primary source is the uncertainty in the value of χ_d. That can be estimated by repeating the above arithmetic with $\chi_d = 0.21$ i.e., modified by 1σ. That results in an asymmetry change of 0.2%. So, $B^0\bar{B}^0$ mixing increases the predicted asymmetry by $0.8 \pm 0.2\%$. It is interesting to note that the measured asymmetry is in better agreement with the prediction including $B^0\bar{B}^0$ mixing than with the prediction without mixing, however, the difference is not at all significant (see figure 6.3).

7.3 Detector uncertainties

Determining the systematic uncertainties that are introduced by the detector can be very difficult. Part of this difficulty comes from the fact that there are certainly unknown errors in the detector construction and calibration as well as in the analysis software. For example, the data from the recent high luminosity runs had to be reanalyzed several times to correct errors which kept being discovered in the calibration and software. In addition the simulator which is used to model the detector's response has been modified many times to correct errors. This makes it unwise to assume that there are not more errors waiting to be discovered. However, it is reassuring that the asymmetry measurement has been mostly immune to these changes in both the simulator and the analysis software. That is, in fact, a quality

of the charge asymmetry. Since it is the sum of individual quark flavors with opposite signs, the systematic uncertainties tend to cancel.

The largest concern for detector systematics is that the detector may somehow introduce a systematic asymmetry. The detector is of course symmetric in $\cos\theta$, but there could be an unknown non-uniformity in the detection efficiency. If there is such a non-uniformity, it should show up in the detection of charged particles. To test for this, figure 7.3 plots the distribution of the cosine of the angle between each particle's momentum vector and the direction of the positron beam (i.e., $-\hat{z}$).[35] Figure 7.3(a) is for all particles, (b) is for positively charged particles, and (c) is for negatively charged particles.

A striking feature of these distributions is that they are very nearly uniform while one might expect that they should follow a $1 + \cos^2\theta$ distribution as the thrust axis does. The uniformity of the distribution comes from the fact that the histogram is limited to the same angular coverage as the thrust axis acceptance cut. So for example, an event with the thrust axis just inside the $|\cos\theta| < 0.65$ cut will have half of its particles outside of the histogram. This reduces the number of particles in the outer bins causing the histogram to flatten. This explanation of the effect has been verified with both generated and simulated data.

For all the particles combined, the asymmetry is $0.2 \pm 0.7\%$ which is consistent with zero as expected for a uniform, symmetric detector. This indicates that there is no significant systematic uncertainty introduced by a non-uniform detection efficiency.

The other distributions exhibit slight asymmetries. For positively charged particles, the asymmetry is $1.3 \pm 1.1\%$. For negatively charged particles, the asymmetry is $-1.0 \pm 1.1\%$. These asymmetries are small and not very significant. The difference between them is $2.3 \pm 1.6\%$ (a 1.5σ effect). But, they are interesting because they are expected and are related to the charge asymmetry. Recall from section 3.3.2 that several methods for determining the jet charge were discussed and finally the momentum weighted jet charge was chosen because it correctly

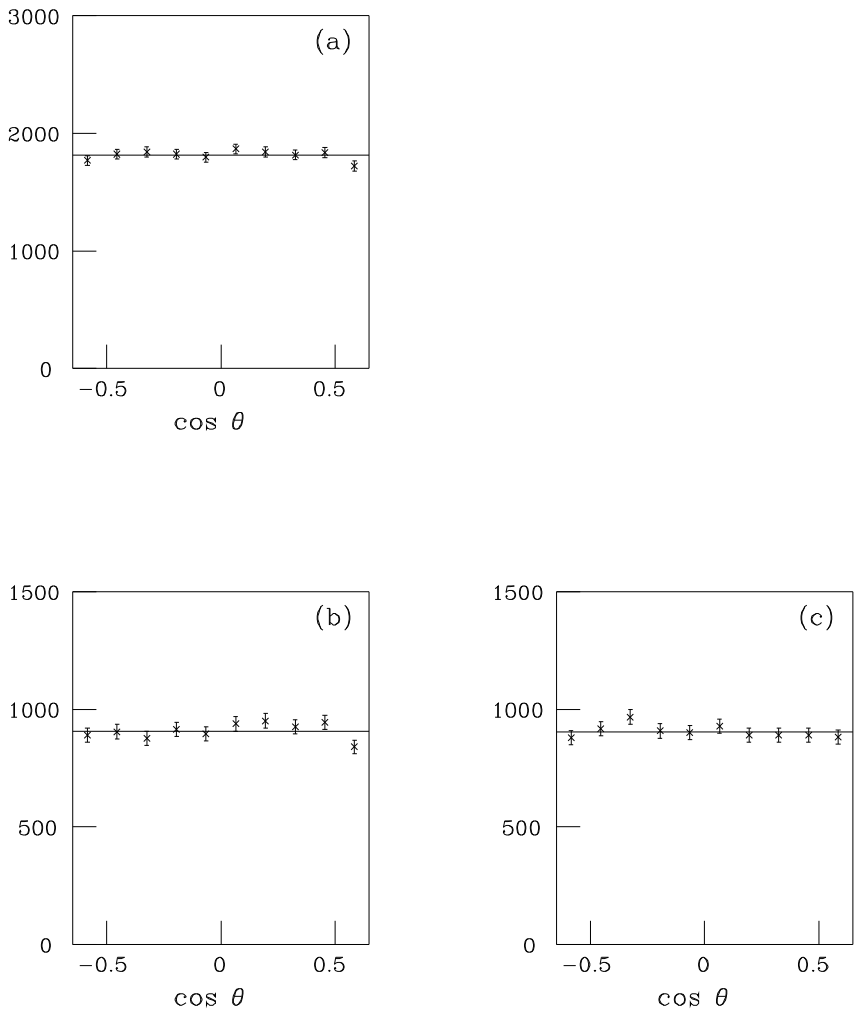

Fig. 7.3: Plot of the angular distribution of each detected particle (in events passing the cuts) in the range $|\cos\theta| < 0.65$. (a) contains all particles, (b) contains only positively charged particles, and (c) contains only negatively charged particles. The horizontal lines are drawn to make any asymmetry more obvious.

identified the jet charge more often than the others. The other methods could also have been used, albeit with reduced significance. In fact, even *randomly* choosing the charge of any particle in the jet will yield the correct charge just *slightly* more than 50% of the time, so there will be a slightly positive asymmetry for positively charged particles, and a slightly negative asymmetry for negatively charged particles. (The same small asymmetry difference is seen in the simulated data, although with only slightly more significance.) This is an amusing confirmation of

the scheme to measure the asymmetry of the combined flavors by using a charge waited asymmetry sum since the expected asymmetry difference between u-type and d-type quarks appears even if the charge direction is determined using only a randomly selected particle!

In chapter 5 it was mentioned that there are a few percent more events with misidentified jet charge in simulated data than in generated data. This difference comes from momentum measurement error and tracking errors. This difference will be considered as part of the next section since it amounts to an uncertainty in the performance of the jet charge technique.

An important detector systematic comes from the acceptance of the detector. The $|\cos\theta| < 0.65$ cut was chosen to stay away from the edge of the CDC and SHW acceptance, 0.8 and 0.73 respectively. However, the stability of this cut must be checked. This is done in the next section by considering systematics arising from the uncertainty in the thrust direction. For now, the detector's effect upon the thrust direction will be checked. To do this, the thrust axis was recalculated using only charged particles. This effectively changes the SHW acceptance to zero, but the thrust value or direction is not significantly altered. The thrust value is changed by 0.03 (FWHM), and the direction is changed by 5 degrees (FWHM). The distribution of the difference between the thrust axis calculated with and without charged particles is shown in figure 7.4(a).

Another test of the thrust direction can be made by comparing the thrust direction to the direction determined using jet clustering. The jet clustering scheme is expected to be slightly more sensitive to detector systematics since it depends on the square of momentum. This comparison is shown in figure 7.4(b). Again, the difference is about 5 degrees.

The final detector systematic to consider is tracking efficiency. It is possible that some of the particles in an event will be missed even if they are within the detector acceptance. The detection efficiency of the CDC is actually very high, but the tracking software can miss tracks or find nonexistent tracks. A reasonable

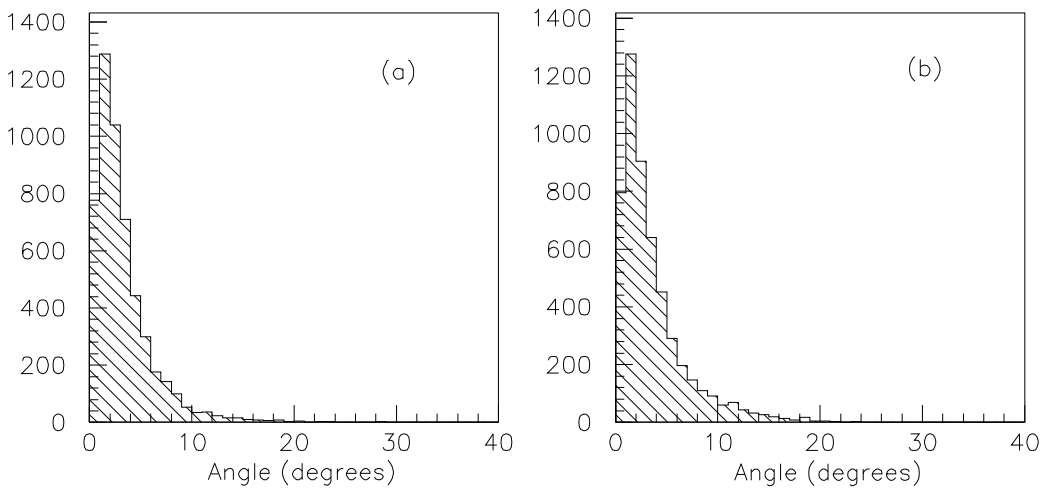

Fig. 7.4: (a) Plot of the angular difference between the thrust direction calculated using all particles and using only charged particles. (b) Plot of the angular difference between the thrust direction and the closest jet.

estimate is that less than 10% of the tracks are missed, and that less than 5% of the found tracks are fakes.[30] These tracking inefficiencies will affect the asymmetry measurement by altering the thrust direction and possibly causing the jet charge to be misidentified. However, these tracking problems are already taken into account by the simulator since it generates CDC hit patterns from which tracks are reconstructed using the same software that is used for the real data. So, it is not necessary to include a separate systematic uncertainty for tracking inefficiencies.

7.4 Analysis Techniques

The majority of this thesis has dealt with describing the techniques used to extract the original quark information from the final state particle information. The thrust and jet charge techniques have been shown to perform well at this task. This section will describe some consistency checks which test the stability of these techniques, and it will estimate the systematic uncertainties that arise from the use of these techniques.

The primary technique is the thrust method used to determine the direction

of the original quark-antiquark pair. As described in section 3.3.1, the thrust axis matches the quark direction to within 5 degrees in nearly 90% of generated events. In simulated data, that deteriorates to 65%, but it is still within 10 degrees for 85% of the events. It is important to verify that this is not different in the real data sample. Of course, it cannot be verified directly, but it can be checked by comparing the thrust direction to the direction determined using another method such as the jet clustering scheme. The difference between these two methods should not be much more than the expected difference between the thrust direction and the quark direction. It should also not be much less since that would indicate that the two methods suffer from very similar uncertainties and make the comparison useless. The comparison was shown in figure 7.4(b) of the last section since it is also a good test of the detector. The important thing to note now is that the distribution is similar to what was seen in figure 5.5 when the thrust direction was compared to the quark direction. That indicates that there is nothing unexpected occurring in the thrust method.

It is nonetheless necessary to quantify the uncertainty in the asymmetry measurement which results from the thrust method. This is done by taking 5° as an estimate of the 1σ uncertainty in the thrust direction and determining what effect that will have upon the asymmetry measurement. The 5° value is chosen since the thrust direction is within 5° of the quark direction in 65% ($\approx 1\sigma$) of the events. For the majority of events, a 5° change in the thrust direction will have no effect since the angular distribution is plotted in bins that are larger than that. It might seem that a 5° change in the thrust direction would allow some particles which are nearly 90° from the thrust axis to slip into the wrong jet. This is not actually a concern, however, since only very low momentum particles are found in that region. In fact it is rare to find any particles there at all. See figures 4.4 or 4.6 as examples. It might also seem that a 5° change would cause a significant difference for events with $|\cos\theta|$ near 0 since it would be possible for an event to be moved from the forward direction to the backward direction, or vice versa. However, that is negligible since the two central bins of the distribution are about equally populated

so smearing would occur equally in both directions. Besides, the asymmetry effect is most pronounced for large values of $|\cos\theta|$, and is very small for $|\cos\theta|$ within 5° of 0. For example, in a large generated data sample, the asymmetry measured using only events satisfying $|\cos\theta| < 0.1$ is $A = -5 \pm 19\%$. The large errors are due to the fact that only a small fraction of the total events are within 5° of 0.

Since the fitted asymmetry relies mostly on the bins with large $|\cos\theta|$. It is only in the outer regions (i.e., large $|\cos\theta|$) that an uncertainty in the thrust direction can have a significant effect. This arises because there is the possibility that the quark direction was outside of the acceptance cut (namely $|\cos\theta| > 0.65$) but that the thrust direction was sufficiently perturbed to make the event pass that cut, or vice versa. Of course this is likely to occur with equal probability for $\cos\theta > 0$ and for $\cos\theta < 0$, so it is not expected to have a large direct affect on the asymmetry. However, it can have an indirect effect by perturbing the outer bins to make them systematically different from the fitted value. This will indirectly alter the asymmetry measurement. To quantify this effect, the acceptance cut was relaxed by 5 degrees, to $|\cos\theta| < 0.71$, and the asymmetry was measured to be $A_h = 7.8 \pm 1.5\%$. Recall that using the standard cut, the value was $A_h = 8.2 \pm 1.7\%$. In addition, the acceptance cut was tightened by 5 degrees, to $|\cos\theta| < 0.6$, and the asymmetry was measured to be $A_h = 8.6 \pm 1.9\%$. This indicates that any uncertainty from the thrust direction introduces a systematic uncertainty of about 0.4% into the asymmetry measurement. Notice that this also includes any systematics which might come from the choice for the acceptance cut of $|\cos\theta| < 0.65$.

The thrust cut is another source of systematics. Since low thrust events are more likely to have incorrectly determined thrust direction and jet charge, events with $T < 0.8$ are discarded. This choice is arbitrary, and the thrust value cannot be determined with complete precision, so the thrust cut is allowed to vary slightly to determine what uncertainty will result in the asymmetry. As mentioned in the previous section, the thrust value changes by 0.03 (FWHM) when the thrust is recalculated using only charged particles. So, 0.02 is a reasonable estimate of the

1σ uncertainty in the thrust value. Changing the thrust cut by that amount results in an asymmetry change of 0.45%.

The other major technique which must be examined is jet charge determination. A convenient consistency check for this is to vary the charge difference cut, ΔQ_{min}. Since the different flavors have different P's, they will respond differently to each value of ΔQ_{min}. That is why the flavor dependent selection efficiencies, f_q, were introduced. Recall that f was significantly lower for c quarks than the for other flavors. This difference will become more pronounced as the charge cut is increased, and it will affect the asymmetry in a predictable way. It is, therefore, important to make sure that the measured asymmetry in real data behaves as predicted when the charge cut is increased. That is shown in figure 7.5 which plots the measured asymmetry as a function of the charge cut for both real data and simulated data.

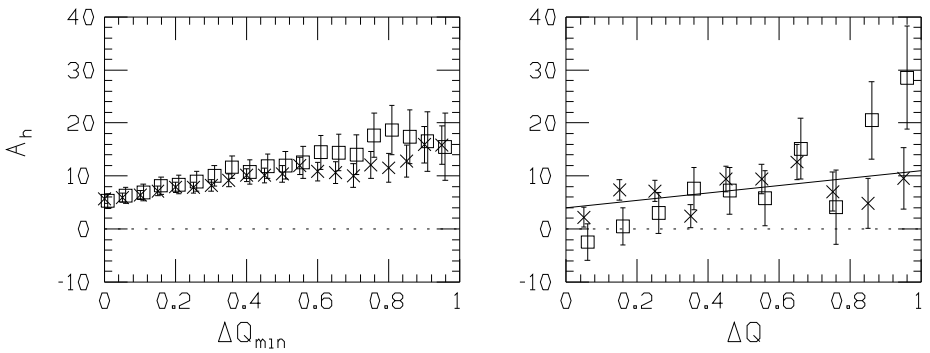

Fig. 7.5: The crosses show simulated data. The squares show real data. In both plots, the real data points are artificially moved slightly to the right to make them easier to distinguish from the simulated data points. (a) plots the measured asymmetry as a function of the charge cut, ΔQ_{min}. (b) plots the measured asymmetry as a function of the charge difference, ΔQ between the two jets, in bins of 0.1. The solid line shows a straight line fit to the simulated data. The χ^2 of the real data relative to the same line is $13.8/10 d.o.f.$

In figure 7.5(a), the asymmetry increases with ΔQ_{min} as expected. It appears that the real data is consistently larger than the simulated data for large values of

ΔQ_{min}, but that is not very significant since there is a strong correlation between the data at different values of ΔQ_{min} since they contain many of the same events. To avoid this, figure 7.5(b) plots the asymmetry for different values of the charge difference, ΔQ, between the two jets. In this representation, there is no correlation between the different points, and the same increase in asymmetry is apparent. To check for inconsistency, the simulated data was fit to a straight line, and the real data points were compared to that line. The χ^2 of that comparison is $13.8/10 d.o.f.$ which indicates that the real data is experiencing the same increase as the simulated data.

These simple consistency checks indicate that the jet charge method is performing as expected. Now, the systematics from the jet charge method will be determined. This can be done by determining the uncertainties on the values of the P_q's and the f_q's and then using Eq. 6.7 to find what effect that has upon the asymmetry. Tables 6.2 and 6.3 list the P and f values along with their statistical uncertainties which are limited by the size of the simulated data sample. There are, of course, systematic uncertainties in these values as well, but they come from the effects which have been accounted for separately in the previous sections. So, all that remains is to estimate a systematic uncertainty which might be introduced by arbitrarily cutting events with the ΔQ_{min} cut. If the ΔQ_{min} cut is varied slightly (by 0.01), the f's all change by about 1%, and the P's change by about 0.5%. Combining these uncertainty estimates in quadrature with the statistical uncertainties and calculating the asymmetry difference which results from a simultaneous 1σ fluctuation in the u type quarks, or a separate fluctuation in the d type quarks gives about 0.6%. If both u type quarks are set 1σ high and all the d type quarks are set 1σ low, the asymmetry changes by 1%. However, that is unrealistically conservative. In the same way, randomly bumping some flavors up and some down has no significant effect on the asymmetry since the changes tend to cancel. But, that is unrealistically optimistic, so an uncertainty estimate of 0.6% will be used.

The systematics are summarized in table 7.1. Combining the various uncer-

Source	Uncertainty in A_h
Radiative corrections	0.6%
Fragmentation	0.13%
s quark suppression	0.5%
$B^0\bar{B}^0$ mixing	0.2%
Thrust direction and $\cos\theta$ cut	0.4%
Thrust cut	0.45%
P and f values	0.6%
Total	1.2%

Table 7.1: Summary of the systematic uncertainties.

tainties in quadrature results in 1.2%.

8. Conclusions

Now that the results have been determined and the systematic uncertainty has been estimated, some conclusions can be drawn from the measurement. The primary conclusion is that the measurement is consistent with the value predicted by electroweak interference in the Standard Model. The measured value, combining all data, is $A_h(<\sqrt{s}>=57.8GeV) = 8.2 \pm 1.7 \pm 1.2\%$ where the first uncertainty is statistical and the second systematic. This agrees well with the expected value of $7.4 \pm 0.2\%$ (without including $B^0\bar{B}^0$ mixing). If there were no electroweak interference, the expected asymmetry would be 0.5% which is more than 3.5σ below the measured value. So, the measurement strongly supports the expectation of electroweak interference in quark production.

As discussed in the previous chapter, the asymmetry prediction is altered when $B^0\bar{B}^0$ mixing is included. That increases the prediction to $8.2 \pm 0.3\%$. This is in good agreement with the measured value, however, the experimental uncertainty is too large to provide clear evidence for $B^0\bar{B}^0$ mixing. Since $B^0\bar{B}^0$ mixing has been observed by other experiments, it will henceforth be incorporated in the prediction.

Since it involves the sum of several nearly cancelling quantities, the asymmetry measurement is sensitive to new physics related to these quantities. For example, if the top quark mass had been light enough to be produced at TRISTAN, it would have increased the asymmetry by a factor of ≈ 1.5. On the other hand, if a fourth generation d type quark were being produced, it would have decreased the asymmetry by a similar factor.

It is now known that the top quark mass is too large for production at TRISTAN, but the asymmetry measurement still gives some information about the top

quark. Within the Standard Model, the axial vector coupling of each quark is equal to its isospin, which is $\frac{1}{2}$ if the quark is a member of a doublet and zero if it is a singlet. If the b quark where to have zero isospin, then its asymmetry would be zero. That would increase the expected asymmetry to 11.3% which is 1.5σ above the measured value. While not highly significant, this does indicate that the b quark has non-zero isospin, so it has an isospin partner. This necessitates the existence of the top quark. The significance of this argument can be increased by changing the ΔQ_{min} cut to enhance the effect of d type quarks (and therefore the b quark) as in figure 7.5. Even more significance can be obtained by directly selecting b events based on their leptonic decays. This has been done by the AMY collaboration as well as others.[3]

8.1 Comparison to other experiments

Since the measured asymmetry agrees with the Standard Model prediction, it can be used to extract information about a Standard Model parameter. The asymmetry depends on all of the parameters, but the dependence is strongest for the axial vector couplings. Recalling Eqs. (2.2) and (2.3),

$$R_q = Q_q^2 - 8Q_q g_V^e g_V^q \Re(\chi) + 16(g_V^{e\,2} + g_A^{e\,2})(g_V^{q\,2} + g_A^{q\,2})|\chi|^2 \tag{2.2}$$

and

$$B_q = -16Q_q g_A^e g_A^q \Re(\chi) + 128 g_V^e g_V^q g_A^e g_A^q |\chi|^2. \tag{2.3}$$

So, the asymmetry of each flavor can be written as

$$A_q = \frac{3}{8} g_A^e g_A^q \frac{-16Q_q \Re(\chi) + 128 g_V^e g_V^q |\chi|^2}{Q_q^2 - 8Q_q g_V^e g_V^q \Re(\chi) + 16(g_V^{e\,2} + g_A^{e\,2})(g_V^{q\,2} + g_A^{q\,2})|\chi|^2}.$$

Assuming universality, the axial vector couplings of all the quarks and leptons are

the same. Calling this g_A, the individual asymmetries become

$$A_q = \frac{3}{8} g_A^2 \frac{-16 Q_q \Re(\chi) + 128 g_V^e g_V^q |\chi|^2}{Q_q^2 - 8 Q_q g_V^e g_V^q \Re(\chi) + 16 (g_V^{e\,2} + g_A{}^2)(g_V^{q\,2} + g_A{}^2)|\chi|^2}.$$

The individual asymmetries depend upon g_A^2, and when the asymmetries are combined, this dependence remains. So, a value for g_A^2 can be extracted from the measured asymmetry. This is done by plotting the predicted asymmetry as a function of g_A^2 in figure 8.1 and comparing that to the measured value. The result is $g_A^2 = 0.252\ ^{+0.059}_{-0.050}\ ^{+0.043}_{-0.039}$. The Standard Model value for the axial vector coupling is $g_A = \frac{1}{2}$, and the world average measured value is $g_A^2 = 0.2492 \pm 0.0012$.[39]

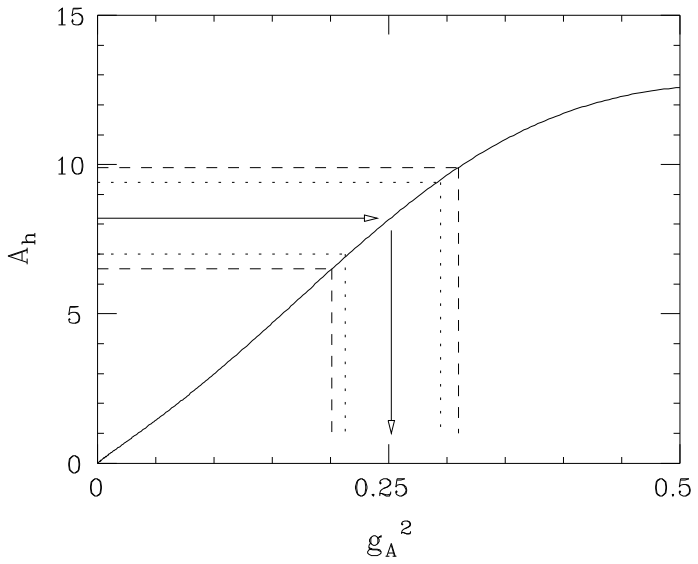

Fig. 8.1: Plot of the expected asymmetry as a function of the square of the axial vector coupling (assuming universality and accounting for $B^0\bar{B}^0$ mixing). The arrow indicates the measured asymmetry value. The dashed lines indicate the statistical errors and the dotted lines indicate the systematic errors in the measured value.

It is desirable to compare the asymmetry measurement to what is obtained by experiments at different energies. This is not straight forward since each group uses different techniques in their measurement, and the results are method dependent.

However, a method independent asymmetry can be unfolded from the value of g_A^2 that was extracted above. The curve in figure 8.1 takes into account all the method dependent parameters of the measurement, specifically the P and f values. So, the extracted g_A^2 value is method independent. From it, a method independent asymmetry can be unfolded by reversing the g_A^2 extraction process with the P's and f's set to unity. In this way, a method independent asymmetry of $A_h^{'} = 9.2\ ^{+3.2}_{-2.7}\ ^{+2.4}_{-2.1}\%$ is unfolded. (The prime is used to distinguish the method independent asymmetry from the measured asymmetry, A_h.) The quoted uncertainties are likely to have been overestimated by the unfolding process. A more reasonable approach is to scale the fractional uncertainty of the measured asymmetry, A_h, to the method independent asymmetry value. That results in $A_h^{'} = 9.2 \pm 1.9 \pm 1.4\%$.

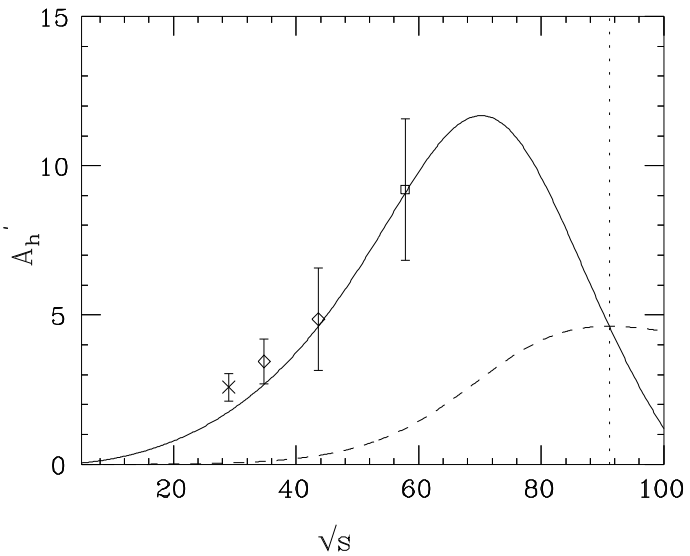

Fig. 8.2: Plot of the method independent asymmetry as a function of the center of mass energy. Results are shown from several experiments at various energies. An x is used to indicate the Mac collaboration's measurement, and a diamond is used to indicate the JADE collaboration's measurements. The uncertainties shown here are scaled from the uncertainties of the measured asymmetries. The solid line shows the Standard Model prediction with electroweak interference. The dashed line shows the Standard Model prediction without interference.

This method independent asymmetry is compared to the results from other experiments[38] in figure 8.2. The method independent asymmetries shown for

the other experiments are unfolded from the quoted g_A^2 values which they extract just as was done above. Other TRISTAN data points are not shown because the measurements are not far from the systematic limits, and they have similar sources of systematic uncertainties, so combining them is not helpful.

The results at different energies all agree with the Standard Model prediction, including electroweak interference. The TRISTAN point is particularly significant since the electroweak interference is near maximum there.

Summary

The interference between γ and Z_0 exchange in electron-positron annihilation into a $q\bar{q}$ pair is expected to produce an angular asymmetry in the production direction of the quark. The magnitude of the effect is expected to be near maximum in the TRISTAN energy range. This asymmetry is measured with the AMY detector on TRISTAN. The quark-antiquark production direction is determined with the thrust axis. The ambiguity between the quark and antiquark is handled by using the charge of the resulting jets, and the charge asymmetry is measured with all the quark flavors combined. The results are consistent with the standard model prediction and strongly disagree with the prediction obtained if electroweak interference is neglected.

Appendix

The measurement described in this thesis was published previously.[40] This appendix describes the differences between the publication and this thesis.

The primary difference is that a momentum weighting is used for the jet charge sum here while a rapidity weighting was used in the publication. Also, a larger data sample is used. The published results used a $27.4pb^{-1}$ data sample while the thesis uses the entire $96pb^{-1}$ accumulated so far. In the publication, the thrust axis was calculated using only charged particles. In the thesis neutral particles are included as well, but as shown in chapter 7, this does not make a significant difference. Finally, there are some changes in notation.

In the publication, rapidity weighting was used in the jet charge sum. Actually, since AMY does not provide particle identification, pseudorapidity was used. It was chosen over momentum weighting for two reasons. A plot of P as a function of κ has a broader peak in rapidity weighting than in momentum weighting. It was expected that this would make rapidity weighting slightly less sensitive to the choice of κ. More importantly, rapidity weighting is not as sensitive to effects from prompt decay which as shown in section 3.4 has a large effect upon c-quark events in momentum weighting. As a result, the c-quark contribution to the asymmetry sum is larger if rapidity weighting is used. That makes the asymmetry value larger.

Since the publication, that choice was changed for the following reasons. In events with 3 jets, rapidity with respect to the thrust axis is not meaningful since the recoiling quark jet is perturbed away from the thrust direction. Instead, the rapidity would have to be measured with respect to the jet axis (from jet clustering). However, it is not always possible to tell the gluon jet and the quark jet apart if

they have nearly equal momentum, and if the gluon jet can be clearly distinguished (because is has lower momentum), then it is unwise to completely neglect the particles in the gluon jet since they are not completely unrelated to the quark's fragmentation. Furthermore, rapidity is sensitive to errors in the determination of the jet direction. The 5° error which was considered to be 1σ in chapter 7 corresponds to a significant change in rapidity. Since these problems do not occur with momentum weighting, it became the preferred technique.

There is also a difference in notation. The publication refers to A_h^M as the measured asymmetry and uses A_h as the method independent asymmetry. The thesis uses A_h as the measured asymmetry and refers to the method independent asymmetry as $A_h^{'}$.

REFERENCES

1. This cross section is easily calculable, but can also be found in the Particle Data Book.

2. A. Bacala et al. (AMY collaboration), Phys. Lett. **B218**, 112 (1989); I. Adachi et al. (TOPAZ collaboration), Phys. Lett. **B208**, 319 (1988).

3. H. Sagawa et al. (AMY collaboration), Phys. Rev. Lett. **63**, 2341 (1989).

4. T. Mori et al. (AMY collaboration), Phys. Lett. **B218**, 499 (1989); T. Kumita et al. (AMY collaboration), Phys. Rev. **D42**, 1339 (1990). T. Kumita Doctoral dissertation, University of Rochester.

5. The Standard Model has described experimental results so well that it deserves to be called a theory, not just a model.

6. The Standard Model was developed by Weinberg, Glashow, and Salam in the sixties.

7. These plots are made using the couplings shown in table 1.1. The Standard Model parameters used are $\sin^2\theta_W = 0.229$, $M_Z = 91.1GeV$, and $\Gamma_Z = 2.6GeV$.

8. Actually, the *center of mass energy* cannot change since it is defined by the momenta of the electron and positron before the collision. So, it is more correct to say that the energy of the γ or Z_0 (often labelled q^2) is diminished. This reduction of q^2 then has the stated effect upon the asymmetry.

9. M. Ye and Ping Gu, AMY Note 542 and 554; W. Braunschweig et al. (TASSO Collaboration), Z. Phys. **C41**, 385 (1988); F. Berends and R. Kleiss. Nucl. Phys. **B178**, 141 (1981); S. Brodsky et al. Phys. Rev. **D14**, 2264 (1976); E. Fernandez et al. (MAC Collaboration), Phys Rev. Lett. **54**,95 (1985); W. Bartel et al. (JADE Collaboration), Z. Phys. **C28**, 343 (1985)

10. W. Bartel et al. (JADE Collaboration) Z. Phys. **C25**, 231 (1984); **C33**, 23 (1986); Y. K. Li et al. (AMY Collaboration) Phys. Rev. **D41**, 2675 (1990).

11. T. Sjöstrand, Int. J. Mod. Phys. **A3**, 751 (1988); E. Reya, Phys. Rep. **58**, 269 (1980); G. Altarelli and G. Parisi, Nucl. Phys. **B126**, 298 (1977); G. Altarelli, Phys. Rep. **81**, 1 (1982);

12. T. Sjöstrand, Computer Phys. Comm. **27**, 243 (1982); T. Sjöstrand and M. Bengtsson, Comp. Phys. Comm. **43**, 367 (1987).

13. A good review of the string fragmentation algorithm can be found in B. Anderssen et al. Phys. Rep. **97**, 33 (1983) and also in T. Sjöstrand. Int. J. Mod. Phys. **A3**, 751 (1988).

14. C. Peterson et al. Phys. Rev. **D27**, 105 (1983).

15. Y. K. Li et al. (AMY Collaboration) Phys. Rev. **D41**, 2675 (1990).

16. The thrust variable was first introduced by E. Farhi, Phys. Rev. Lett. **39**, 1587 (1977).

17. There are many jet clustering schemes. The method used in this thesis was introduced by the JADE group. See W. Bartel et al. Z. Phys. **C33**, 23 (1986).

18. The y_{cut} value used in this thesis is $(\frac{13GeV}{E_{vis}})^2$. In a previous AMY analysis, a y_{cut} value of $(\frac{9GeV}{E_{vis}})^2$ was used, but it was decided that a larger value should be used here. This is important since the jet clustering method is used to detect photon and gluon radiation. To detect an isolated photon, it is desirable to have the photon well separated from any other jet. This requires a large y_{cut}. Detecting gluon radiation is necessary so that the asymmetry can be checked for any dependence upon gluon radiation. For that purpose, it is important to have a clearly distinguished gluon jet. Again, this requires a large y_{cut}.

19. The actual value of the thrust cut is not important here. A final value will be decided upon after detector effects are included.

20. R. Field and R. Feynman. Nucl. Phys. **B136**, 1 (1978)

21. H. Sagawa et al. (AMY collaboration), Phys. Rev. Lett. **63**, 2341 (1989). S.S. Myung, et al. (AMY collaboration), KEK-PREPRINT-90-66-mc (microfiche), (1990).

22. The technical details describing TRISTAN are taken from KEK report 86-14.

23. The source for much of the technical information is the AMY proposal, TRISTAN-EXP-003, Nov. 1984.

24. The straws were manufactured by Euclid Spiral Paper Tube company, Applecreek, Ohio (216) 698-4711. They were constructed by wrapping two layers of mylar strips around a rod of the desired diameter and then gluing the layers together.

25. This gas choice is called HRS gas because it was developed by the HRS collaboration. It was chosen because it is non-flammable. That was a requirement due to the VTX's high leak rate.

26. To achieve the physics goals, the resolution of each straw needs to be $\approx 50\mu m$. Since the drift velocity is $\approx 50\mu m/ns$, a timing resolution of $\approx 1ns$ is needed.

27. Due to leaks, the choice of gas mixture was dominated by safety concerns and the pressure was kept only slightly above 1 atm.

28. Nickel-chromium wires were used. Their resistance is $4k\Omega/m$.

29. The ADC used is the LeCroy 1885F. It is a 15-bit charge ADC with 96 input channels. It is readout out by Fastbus.

30. The tracking algorithm was written by T. Mori and is described in his thesis, **UR-1104** (1988). It is also described in the AMY proposal, TRISTAN-EXP-003, Nov. 1984.

31. There are no publications giving the performance of AMY's simulator, but there would certainly be no AMY publications if the simulator was not understood. But, reference [15] compares many event shape variables in real and simulated data.

32. Recall that the SHW is only efficient at detecting electrons and photons. A quark jet produces photons primarily through π^0's decaying to a pair of photons.

33. Actually, a κ slightly less than 0.5 gives the highest P values, but it is only slightly better. It was considered unwise to choose such parameters too precisely since measurement error makes them not so well defined. For example, the difference between $|p|^{0.4}$ and $|p|^{0.5}$ is less than the experimental uncertainty in either quantity. Because of that, $\kappa = 0.5$ was chosen because it corresponds to a more physically meaningful quantity i.e., $\sqrt{p}$.

34. J. Fujimoto et al. Progr. Theor. Phys. Suppl 100, 1 (1990). J. Fujimoto et al. Progr. Theor. Phys. **79**, No. 3 , 701 (1988).

35. This seemingly odd angle definition was chosen for a reason. The angle of the positively charged jet direction used for the asymmetry measurement was defined with respect to the positron beam direction (i.e., $-\hat{z}$). This was chosen so that it would be the angle between the positively charged incoming particle and the positively charged outgoing particle. For consistency, the same angle definition is used when plotting the distribution of the individual charged particles.

36. W. Bartel et al. (JADE Collaboration) Z. Phys. **C20**, 187 (1983). H. Aihara et al. (TPC Collaboration) Phys. Rev. Lett. **53**, 2378 (1984). M. Derrick et al. (HRS Collaboration) Phys. Lett. **B158**, 519 (1985).

37. H. Albrecht et al. (ARGUS Collaboration) Phys. Lett. **B192**, 245 (1987). M. Artuso et al. (CLEO Collaboration) Phys. Rev. Lett. **62**, 2233 (1989).

38. W. Ash et al. (MAC Collaboration) Phys. Rev. Lett. **58**, 1080 (1987). T. Greenshaw et al. (JADE Collaboration) Z. Phys. **C42**, 1 (1989). K. Abe et al. (VENUS Collaboration) Phys. Lett. **B232**, 425, (1989). I. Idachi et al. (TOPAZ Collaboration) Phys. Lett. **B255**, 613, (1991). D. Decamp et al. (ALEPH Collaboration) CERN-PPE **91-27**, (1991). P. Abreu et al. (DELPHI Collaboration) Phys. Lett. **B277**, 371, (1992). P. D. Acton et

al. (OPAL Collaboration) CERN-PPE **92-119**, (1992). Submitted to Phys. Lett. B.

39. Particle Properties Data booklet, June 1992.

40. D. Stuart et al. (AMY collaboration), Phys. Rev. Lett. **64**, 983 (1990).